1-1-2022

# Ultrahigh-temperature granulite-facies metamorphism and exhumation of deep crust in a migmatite dome during late- to post-orogenic collapse and extension in the central Adirondack Highlands (New York, USA)

Ellen P. Metzger
*San Jose State University*, ellen.metzger@sjsu.edu

Mary L. Leech
*San Francisco State University*

Michael W. Davis
*San Francisco State University*

Jackson V. Reeder
*San Francisco State University*

Brandon A. Swanson
*San Francisco State University*

*See next page for additional authors*


## Recommended Citation
Ellen P. Metzger, Mary L. Leech, Michael W. Davis, Jackson V. Reeder, Brandon A. Swanson, and Heather V. Waring. "Ultrahigh-temperature granulite-facies metamorphism and exhumation of deep crust in a migmatite dome during late- to post-orogenic collapse and extension in the central Adirondack Highlands (New York, USA)" *Geosphere* (2022): 261-297. https://doi.org/10.1130/GES02318.1

Research Paper

GEOSPHERE

GEOSPHERE, v. 18, no. 1

https://doi.org/10.1130/GES02318.1

16 figures; 7 tables; 1 set of supplemental files

CORRESPONDENCE: leech@sfsu.edu

CITATION: Metzger, E.P., Leech, M.L., Davis, M.W., Reeder, J.V., Swanson, B.A., and Waring, H.V, 2021, Ultrahigh-temperature granulite-facies metamorphism and exhumation of deep crust in a migmatite dome during late- to post-orogenic collapse and extension in the central Adirondack Highlands (New York, USA): Geosphere, v. 18, no. 1, p. 261–297, https://doi.org/10.1130/GES02318.1.

Science Editor: Shanaka de Silva
Associate Editor: Michael L. Williams

Received 15 July 2020
Revision received 19 March 2021
Accepted 14 July 2021

Published online 2 December 2021



# Ultrahigh-temperature granulite-facies metamorphism and exhumation of deep crust in a migmatite dome during late- to post-orogenic collapse and extension in the central Adirondack Highlands (New York, USA)

**Ellen P. Metzger[1], Mary L. Leech[2], Michael W. Davis[2], Jackson V. Reeder[2], Brandon A. Swanson[2], and Heather V. Waring[1]**

[1]Geology Department, San Jose State University, One Washington Square, San Jose, California 95192, USA
[2]Department of Earth and Climate Sciences, San Francisco State University, 1600 Holloway Avenue, San Francisco, California 94132, USA

## ABSTRACT

**This study combines field observations, mineral and whole-rock geochemistry, phase equilibrium modeling, and U-Pb sensitive high-resolution ion microprobe (SHRIMP) zircon geochronology to investigate sillimanite-bearing felsic migmatites exposed on Ledge Mountain in the central Adirondack Highlands (New York, USA), part of an extensive belt of mid-crustal rocks comprising the hinterland of the Mesoproterozoic Grenville orogen. Phase equilibrium modeling suggests minimum peak metamorphic conditions of 960–1025 °C and 11–12.5 kbar during the Ottawan orogeny—significantly higher pressure-temperature conditions than previously determined—followed by a period of near-isothermal decompression, then isobaric cooling. Petrography reveals abundant melt-related microstructures, and pseudosection models show the presence of at least ~15%–30% melt during buoyancy-driven exhumation and decompression. New zircon data document late Ottawan (re)crystallization at ca. 1047 ± 5 to 1035 ± 2 Ma following ultrahigh-temperature (UHT) metamorphism and anatexis on the retrograde cooling path. Inherited zircon cores give a mean date of 1136 ± 5 Ma, which suggests derivation of these felsic granulites by partial melting of older igneous rocks. The ferroan, anhydrous character of the granulites is similar to that of the ca. 1050 Ma Lyon Mountain Granite and consistent with origin in a late- to post-Ottawan extensional environment. We present a model for development of a late Ottawan migmatitic gneiss dome in the central Adirondacks that exhumed deep crustal rocks including the Snowy Mountain and Oregon anorthosite massifs with UHT Ledge Mountain migmatites. Recognition of deep crustal meta-plutonic rocks recording UHT metamorphism in a migmatite gneiss dome has significant implications for crustal behavior in this formerly thickened orogen.**

Mary Leech https://orcid.org/0000-0003-2871-5297

## INTRODUCTION

Decades of multifaceted studies of the Grenville province (eastern North America; Fig. 1) have expanded our understanding of one of the world's best-documented Mesoproterozoic orogenic belts (McLelland et al., 2013; Rivers, 2015). The metamorphic signatures of rocks in different parts of the Grenville province helped to reveal its crustal architecture and, combined with structural data and thermomechanical modeling, were crucial to the development of the conceptual model of the Grenville orogen as a large hot orogen in which protracted contraction and development of an orogenic plateau was followed by collapse, extension, and exhumation of deep crustal rocks to mid-crustal levels (Rivers, 2008, 2012, 2015). However, refinement of that tectonic model will require more precise documentation of the temporal and spatial relationships between deformation, metamorphism, and melting (e.g., Heumann et al., 2006, Bickford et al., 2008; Rivers, 2015; Regan et al., 2019; Williams et al., 2019). The majority of pressure-temperature (*P-T*) estimates used for constraining the tectonic evolution of the Grenville orogen are based on classical inverse thermobarometry (e.g., Lasalle and Indares, 2014), which has been shown to be problematic in high-grade metamorphic terranes due to post-peak diffusion and re-equilibration (e.g., Frost and Chacko, 1989; Spear and Florence, 1992). Forward thermodynamic modeling using internally consistent thermodynamic databases, when carefully applied, can help address these challenges. However, in spite of its wide application in unraveling the geodynamic evolution of other orogenic belts, "pseudosection" (or isochemical phase diagram) modeling has been underutilized in the Grenville province and its outlier, the Adirondack Mountains of New York (northeastern United States; Lasalle and Indares, 2014; Regan et al., 2015; Rivers, 2015).

In this contribution, we integrate thermodynamic modeling with microtextural analysis, mineral chemistry, and U-Pb sensitive high-resolution ion microprobe (SHRIMP) zircon geochronology to describe sillimanite-bearing felsic migmatites exposed on Ledge Mountain in the central Adirondack Highlands, part of an extensive belt of mid-crustal rocks extending from Labrador (Canada) to New York State comprising the hinterland of the Grenville orogen (Fig. 1A; Rivers, 2012). We document late- to post-Ottawan ultrahigh-temperature (UHT) metamorphism and anatexis and evaluate its implications in the context of recent studies of late- to post-orogenic collapse, extension, and melting

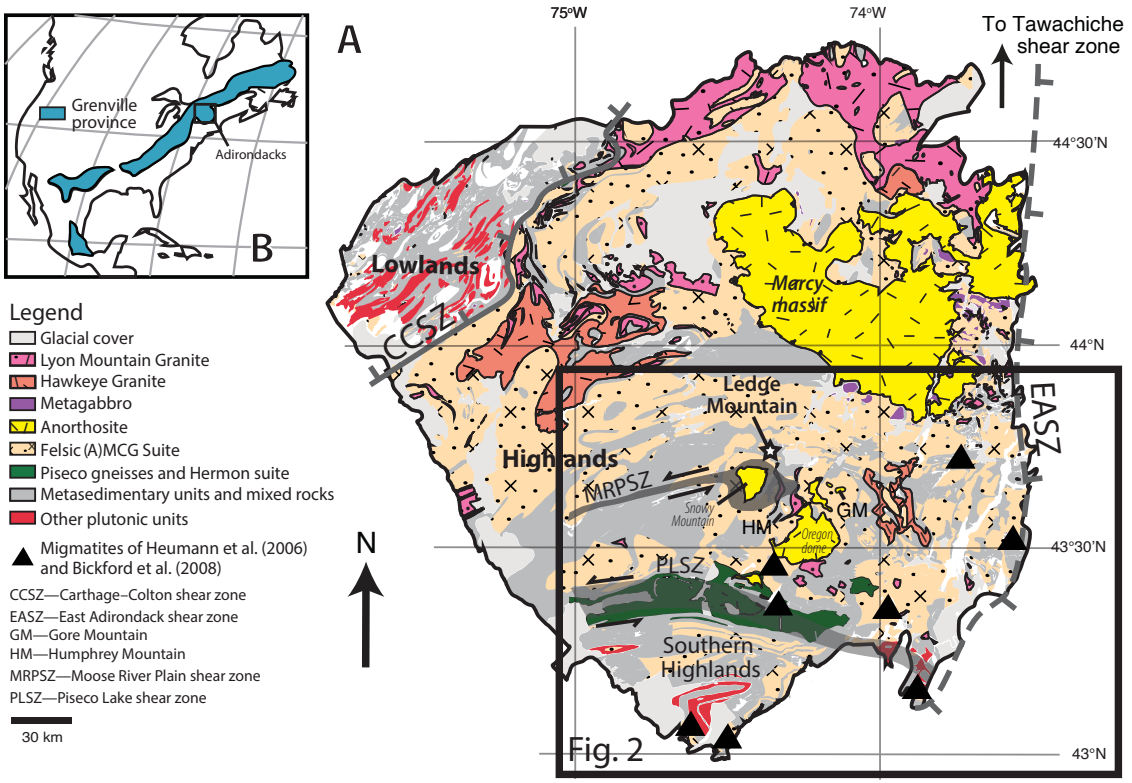


**Figure 1. Maps of the Grenville orogen and Adirondack Highlands. (A) General geologic map of major intrusive suites in the Adirondack Highlands and related Grenville rocks including the anorthosite-mangerite-charnockite-granite (AMCG) suite and undifferentiated medium- to high-pressure metamorphic rocks (modified from Wong et al., 2012; Peck et al., 2013). Triangles mark migmatite samples from Heumann et al. (2006) and Bickford et al. (2008). The location of Fig. 2 is shown for reference. (B) Location of the Adirondacks within the North American Grenville orogen (after Rivers, 1997, 2015).**

in the Adirondack Highlands (Bickford et al., 2008; Wong et al., 2012; McLelland et al., 2013; Regan et al., 2019; Williams et al., 2019). Whole-rock major and trace element geochemistry is used to constrain the petrogenesis of the Ledge Mountain migmatites, and we present a model for the exhumation of deep crustal rocks in a migmatitic gneiss dome (Fig. 2).

## GEOLOGIC SETTING AND PREVIOUS WORK

The Grenville orogen, a portion of which is exposed in the Grenville province of Canada and its extensions (Fig. 1B), is interpreted as resulting from the collision of Laurentia and Amazonia to form the supercontinent Rodinia (e.g., McLelland et al., 2010, 2013; Rivers, 2015). Rocks of the Grenville province range in age from Archean to Mesoproterozoic and generally become younger toward the southeast, reflecting pre-collision accretionary growth of the Laurentian margin (e.g., McLelland et al., 2013; Rivers, 2015). The Mesoproterozoic rocks of the Grenville province and its outlier in the Adirondack Mountains were affected by two major orogenic events, the Shawinigan (1190–1140 Ma) and the Grenville (1090–980 Ma) orogenies (McLelland et al., 2013; Rivers, 2008, 2015). The first pulse of the Grenville orogeny—the Ottawan (1090–1020 Ma)—generally involved granulite-facies metamorphism, while amphibole-facies conditions were attained during the younger Rigolet phase (1010–980 Ma) (McLelland et al., 2010, 2013). The Rigolet stage was significant in the western Grenville province but is thought to have had minimal impact in the Adirondacks (Williams et al., 2019). Some researchers subdivide the Ottawan orogeny in the Adirondack Highlands into a prograde and peak phase at ca. 1090–1060 Ma followed by an extensional phase from 1060 to 1020 Ma (Wong et al., 2012; Chiarenzelli et al., 2017; Williams et al., 2019).

McLelland et al. (2013) attributed igneous activity following both the Shawinigan and Ottawan orogenies to post-orogenic collapse, lithospheric delamination, and asthenospheric upwelling. The voluminous post-Shawinigan anorthosite-mangerite-charnockite-granite (AMCG) suite was emplaced between ca. 1165 and 1145 Ma. Aleinikoff and Walsh (2017) reported dates of 1144–1138 ± 10 Ma for oscillatory-zoned zircon cores in the less-voluminous Hawkeye Granite. The ca. 1050 Ma Lyon

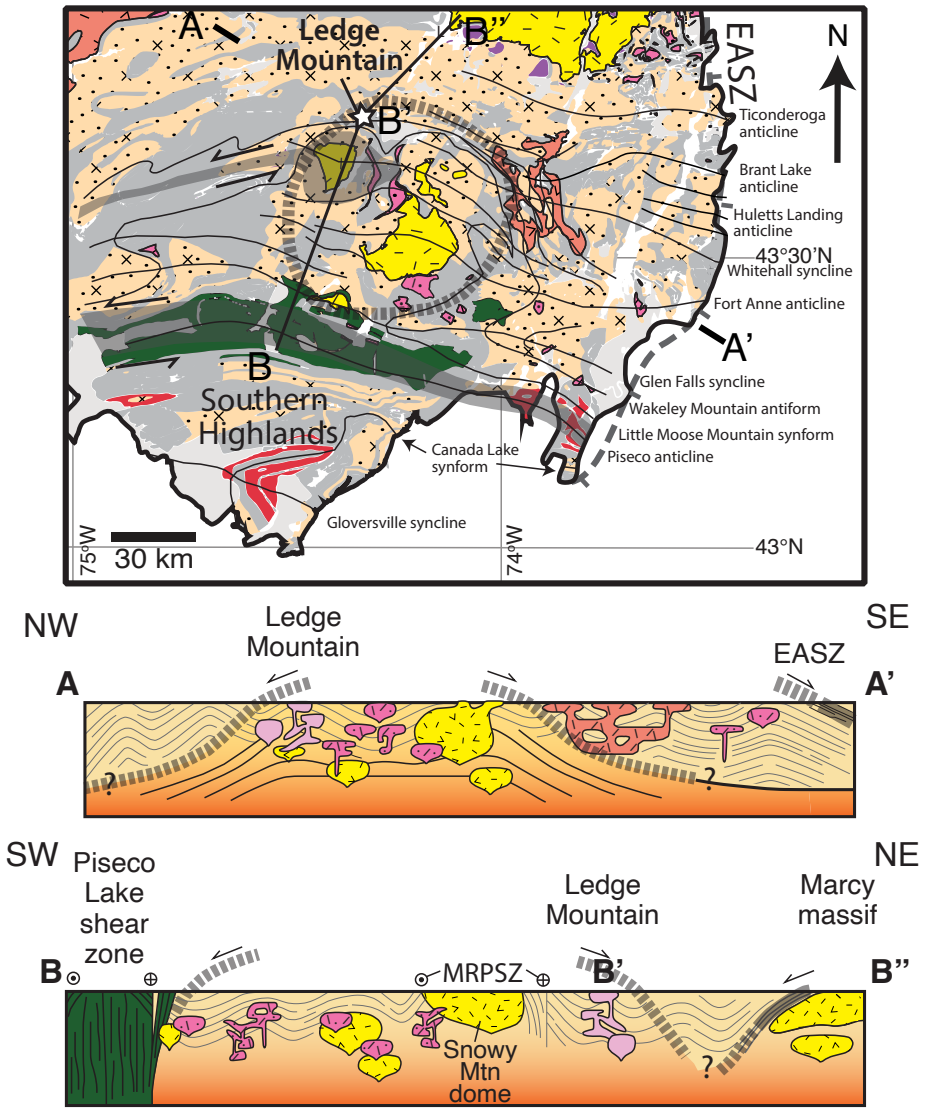


**Figure 2. Generalized structural map of the central and southern Adirondack Highlands, with the northwest-southeast–trending cross-section A-A′ across Ledge Mountain to the East Adirondack shear zone (EASZ), and the B-B′-B″ cross-section from the northeast at the Marcy massif to the southwest in the Piseco Lake shear zone. Both cross-sections show the tentative location of a lower-crustal gneiss dome in the central Adirondack Highlands (dashed area on map; based on Jamieson et al., 2007; Rey et al., 2009; Rivers, 2009, 2012, 2015). Star marks the location of Ledge Mountain. See Figure 1 for symbol explanation. Light pink bodies in cross-sections are Ledge Mountain felsic migmatites. MRPSZ—Moose River Plain shear zone. Compiled from Geraghty (1978), McLelland et al. (1978), McLelland and Isachsen (1980), McLelland (1991), Valentino et al. (2008), McLelland and Selleck (2011), Wong et al. (2012), and Regan et al. (2019).**

Mountain Granite (formerly Lyon Mountain Gneiss; Chiarenzelli et al., 2017), the youngest plutonic rock in the Adirondacks, surrounds much of the Adirondack Highlands (Fig. 1A; e.g., McLelland et al., 2002, 2013; Valley et al., 2011; Chiarenzelli et al., 2017) and is thought to have formed by anatexis during late Ottawan orogenic collapse and extension (Valley et al., 2011; McLelland et al., 2013; Chiarenzelli et al., 2017). Unlike the older plutonic rocks, the Lyon Mountain Granite mostly lacks penetrative deformation, and its ferroan, A-type geochemical character is consistent with formation in a post-orogenic extensional environment (Chiarenzelli et al., 2017). In places, the Lyon Mountain Granite is accompanied by Na and K fluid alteration, development of Kiruna-type magnetite-apatite deposits, and the presence of sillimanite-quartz veins and nodules (Whitney and Olmsted, 1988; McLelland et al., 2002; Selleck et al., 2005; Valley et al., 2011; Chiarenzelli et al., 2017).

## Adirondack Highlands

The Adirondack Mountains are divided into two contrasting areas separated by the northeast-trending, northwest-dipping Carthage-Colton shear zone (Fig. 1A; McLelland et al., 2010, 2013). The Adirondack Highlands are dominated by plutonic rocks and record granulite-facies metamorphic conditions; the Adirondack Lowlands consist predominantly of amphibolite-facies metasedimentary rocks (Fig. 1A). Mapping during the 1970s and 1980s established that multiple sets of folds are variably developed in the Lowlands and Highlands and range in age from Shawinigan to Ottawan (McLelland and Isachsen, 1980; McLelland et al., 2013).

Estimated metamorphic *P-T* conditions of 600–850 °C and 6–8 kbar for the Adirondack Highlands (McLelland et al., 2013) are based on extensive application of classic mineral thermobarometry including two-feldspar, Fe-Ti oxide solvus, and Fe-Mg exchange thermometry for orthopyroxene-clinopyroxene, garnet-biotite, and garnet-pyroxene pairs; and garnet-aluminosilicate-silica-plagioclase (GASP) and other barometers (e.g., Bohlen and Essene, 1977; Bohlen et al., 1980, 1985; Florence and Spear, 1995; Spear and

Markussen, 1997; Storm and Spear, 2005). The highest previously reported temperatures (~800–850 °C at 7–8 kbar) center on the Marcy anorthosite massif in the central Adirondack Highlands (Fig. 1A; Spear and Markussen, 1997), with later metamorphic garnet growth in the anorthosite taking place at lower temperatures (~750–650 °C; Spear and Markussen, 1997; Peck et al., 2018). Shinevar et al. (2021) recently reported UHT conditions (950 ± 40 °C, 8.5–10 kbar) for garnet amphibolite at Gore Mountain (Fig. 1A) based on thermobarometry, thermodynamic modeling, and diffusion models.

Although *P-T* conditions have been extensively documented across the Adirondack Highlands, the timing of metamorphism is not well constrained, and similar metamorphic assemblages and conditions in different locations may represent separate metamorphic events (Regan et al., 2019). For example, Peck et al. (2018) used in situ zircon geochronology to establish an Ottawan age (1050–1035 Ma) for metamorphic mineral growth in the Marcy massif (Fig. 1A), while Shawinigan ages (1170–1130 Ma) were obtained from zircon rims in quartzite that record similar metamorphic conditions in the southern Highlands (Peck et al., 2018). The central and southern Adirondacks are inferred to have had different geologic histories and are separated by a major lithotectonic discontinuity, the Piseco Lake shear zone (Valentino et al., 2018; Fig. 1A).

Sillimanite is the dominant aluminosilicate in the Adirondacks. Multiple reports of kyanite in Ledge Mountain granulites in the central Highlands (Boone, 1978; Geraghty, 1978; McLelland et al., 1978) are not well documented and require identification by Raman spectroscopy for confirmation. Both counterclockwise (Bohlen et al., 1985; Bohlen, 1987; Spear and Markussen, 1997) and clockwise (McLelland and Selleck, 2011) metamorphic *P-T-t* (where *t* is time) paths have been proposed for the Highlands (Darling and Peck, 2016). Storm and Spear (2005) concluded that their data for metapelites exposed in the southern Highlands were insufficient for distinguishing between these two paths.

Late Grenville extension following orogenic collapse is thought to have taken place along the Carthage-Colton shear zone and the East Adirondack shear zone (Fig. 1A), which may correlate to the Tawachiche shear zone to the north of the Adirondacks in Quebec, Canada (Fig. 1A; Bickford et al., 2008; Wong et al., 2012). This resulted in extensive fluid infiltration, partial melting, and development of the Adirondack Highlands as a gneiss dome (e.g., Fig. 2; Bickford et al., 2008; McLelland and Selleck, 2011; Wong et al., 2012; Regan et al., 2019).

Migmatitic metapelites are widespread across the Adirondacks, but the timing and tectonic setting for anatexis vary (Fig. 1A; Heumann et al., 2006; Bickford et al., 2008; Regan et al., 2019; Williams et al., 2019). Based on U-Pb SHRIMP analyses of zircon from migmatites in the Adirondack Lowlands and southern Highlands, Heumann et al. (2006) concluded that anatexis took place during the Shawinigan orogeny (ca. 1190–1160 Ma) and subsequent AMCG magmatism (ca. 1160–1140 Ma). The lack of evidence for Ottawan anatexis during granulite-facies metamorphism in the southern Highlands was attributed to dehydration of the rocks during earlier episodes of melting. Bickford et al. (2008) documented Ottawan anatexis ca. 1050 Ma in the eastern Highlands that they attributed to localized influx of a small amount of fluids (because there is no evidence for widespread retrograde metamorphism) and/or decompression melting during exhumation (Fig. 1A).

### Ledge Mountain and Field Relationships

Ledge Mountain is located to the northeast of the Snowy Mountain anorthosite massif near Indian Lake, New York (Fig. 1A). Migmatitic sillimanite-bearing quartzofeldspathic rocks exposed at Ledge Mountain are surrounded by marble in the core of a recumbent antiform (Geraghty, 1978). Previous studies of Ledge Mountain and the surrounding area include early investigations of field relationships and application of conventional thermobarometry (Boone, 1978; Geraghty, 1978; McLelland et al., 1978; Metzger, 1980). Boone (1978) used garnet-biotite exchange thermometry and GASP barometry to calculate metamorphic conditions of 695–700 °C and 7.4–8.2 kbar.

Ledge Mountain "migmatite" refers to neosome in which tan to pink, fine- to medium-grained, granoblastic melanosome hosts millimeter- to centimeter-scale leucosome and wider pegmatitic leucosome. Leucosome has both diffuse contacts and direct genetic relationship with its adjacent host rock, and sharp contacts where leucosome has migrated short distances (i.e., in-source). In the melanosome, quartz, alkali feldspar, and plagioclase are the dominant minerals and vary in their relative proportions. Sillimanite, garnet, biotite, and Fe-Ti oxide minerals typically each make up <5% of the melanosome. In places, quartzofeldspathic melanosome alternates with lenses and layers of sillimanite- and quartz-rich leucosome that weathers in positive relief and define a foliation (Fig. 3A). Sillimanite and quartz concentrations vary within leucosome and in some locations make up 15%–30% of the outcrop; overall, these sillimanite and quartz layers decrease in abundance from west to east across Ledge Mountain (Boone, 1978; McLelland et al., 1978; Metzger, 1980; Swanson, 2019).

Pegmatitic leucosomes are composed mainly of coarse quartz and perthitic K-feldspar (Fig. 3B), and are mostly concordant to the foliation of the host migmatitic gneiss; they are invariably surrounded by a shell of weakly foliated biotite-rich quartzofeldspathic neosome that is enriched in biotite (Fig. 3C). Pegmatitic leucosome bodies extend for up to 6 m and range from 20 cm to 2 m in thickness, with thinner ~5 mm fingers within the melanosome near their contact. Pegmatitic leucosome bodies are largely undeformed, although a few have been slightly folded. "Pegmatitic" describes the coarse texture of the leucosome and should not be confused with "pegmatite," which is a genetic term describing a recrystallized melt that has migrated away from its source area (Sawyer, 2008).

A ~12 × 6 m lens of white, coarse-grained plagioclase-quartz rock with <5% biotite and garnet (sample 11) was observed at one location. Its contact with the surrounding K-feldspar-rich rock is obscured.

## PETROGRAPHY

Sample locations for this study are shown in Figure 4. This study focuses on migmatite samples

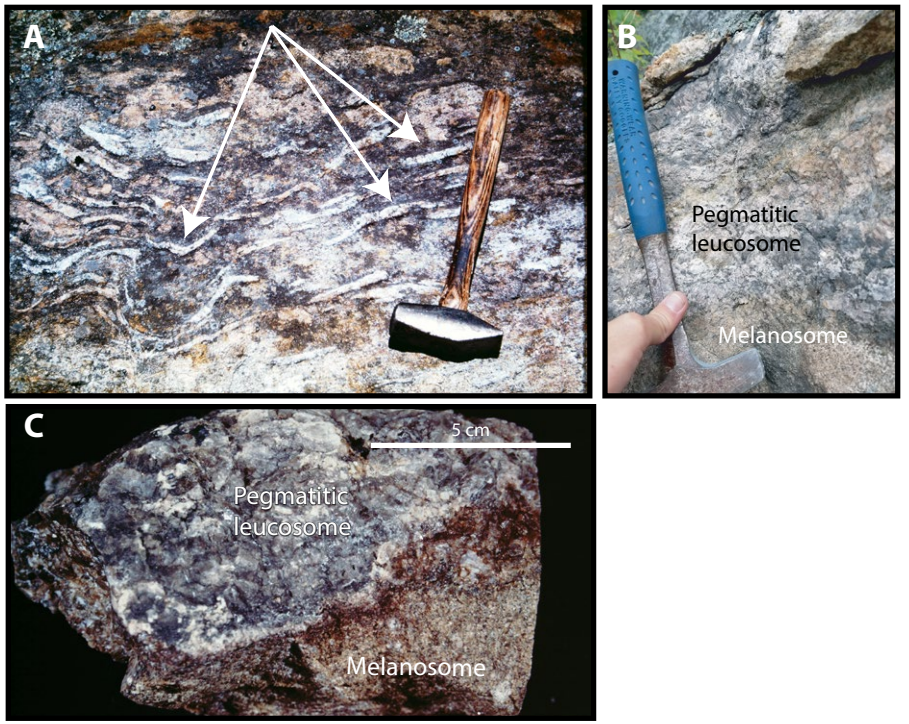


**Figure 3. Field photos showing macroscopic features. (A) Outcrop with prominent sillimanite and quartz layers in migmatite near sample AD-11 (43°48′35″ N, 74°18′16″ W). (B) Coarse-grained quartz and K-feldspar pegmatite near sample 17LM12 (43°48′37.3″ N, 74°18′17″ W; from Swanson, 2019). (C) Hand specimen displaying pegmatitic leucosome surrounded by melanosome.**

containing sillimanite and poikiloblastic garnet because these rocks are most likely to yield information about the metamorphic conditions that formed them.

Ledge Mountain migmatites are characterized by mineralogical and textural heterogeneity on the millimeter to decimeter scale, which is typical of migmatites (Sawyer, 2008). However, the migmatites are relatively homogeneous in terms of texture and mineralogy except for pegmatitic leucosomes that form separate lenses and bodies of varied dimensions and that may in part represent externally derived melts particularly where they cut across the local fabric. Representative microstructures showing key mineralogic relationships and evidence for the presence of abundant melt are shown in Figures 5, 6, and 7. Quartz and feldspar define the dominant mineral assemblage in all samples, but the relative proportions of quartz, alkali feldspar, and plagioclase are variable. Most samples contain both K-feldspar and plagioclase, but sample 11, a meta-leucotonalite, lacks K-feldspar and consists of plagioclase and quartz in approximately equal proportions (Table 1). In addition to quartz and feldspar, fine- to medium-grained, granoblastic to weakly foliated migmatites contain small and variable amounts of sillimanite, biotite, garnet, ilmenite, magnetite, and hercynite (Table 1; Fig. 5). Sillimanite-quartz layers and biotite define a weak foliation in places. Accessory minerals

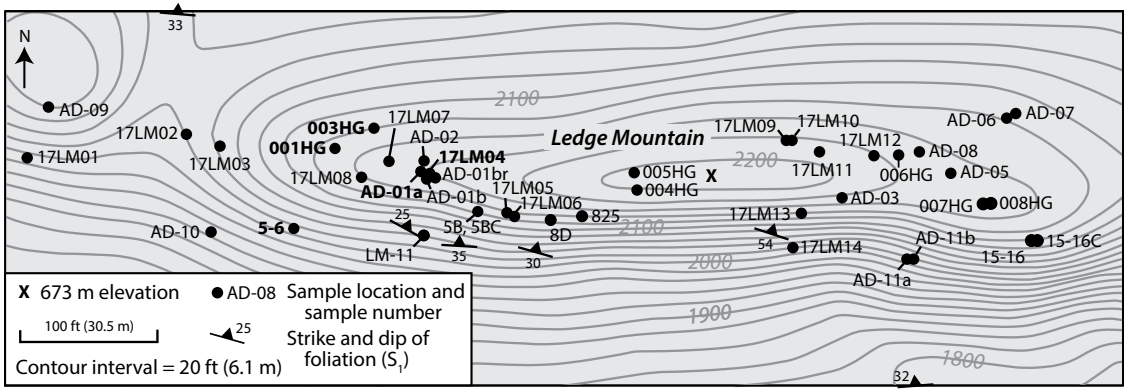


**Figure 4. Map of Ledge Mountain showing 38 sample locations within felsic gneiss and migmatites. Strike and dips of foliation are shown where measured (foliation is weak or not visible at the macroscale). Modeled samples AD-01, 17LM04, 5-6, 001HG, and 003HG are highlighted in bold text. Sample AD-01br is a replicate. Contour interval is 6.1 m (20 feet). "X" marks elevation 673 m (2208 feet) at 43°48′37.88″N, 74°18′22.55″W. Adapted from Metzger (1980) and Swanson (2019).**

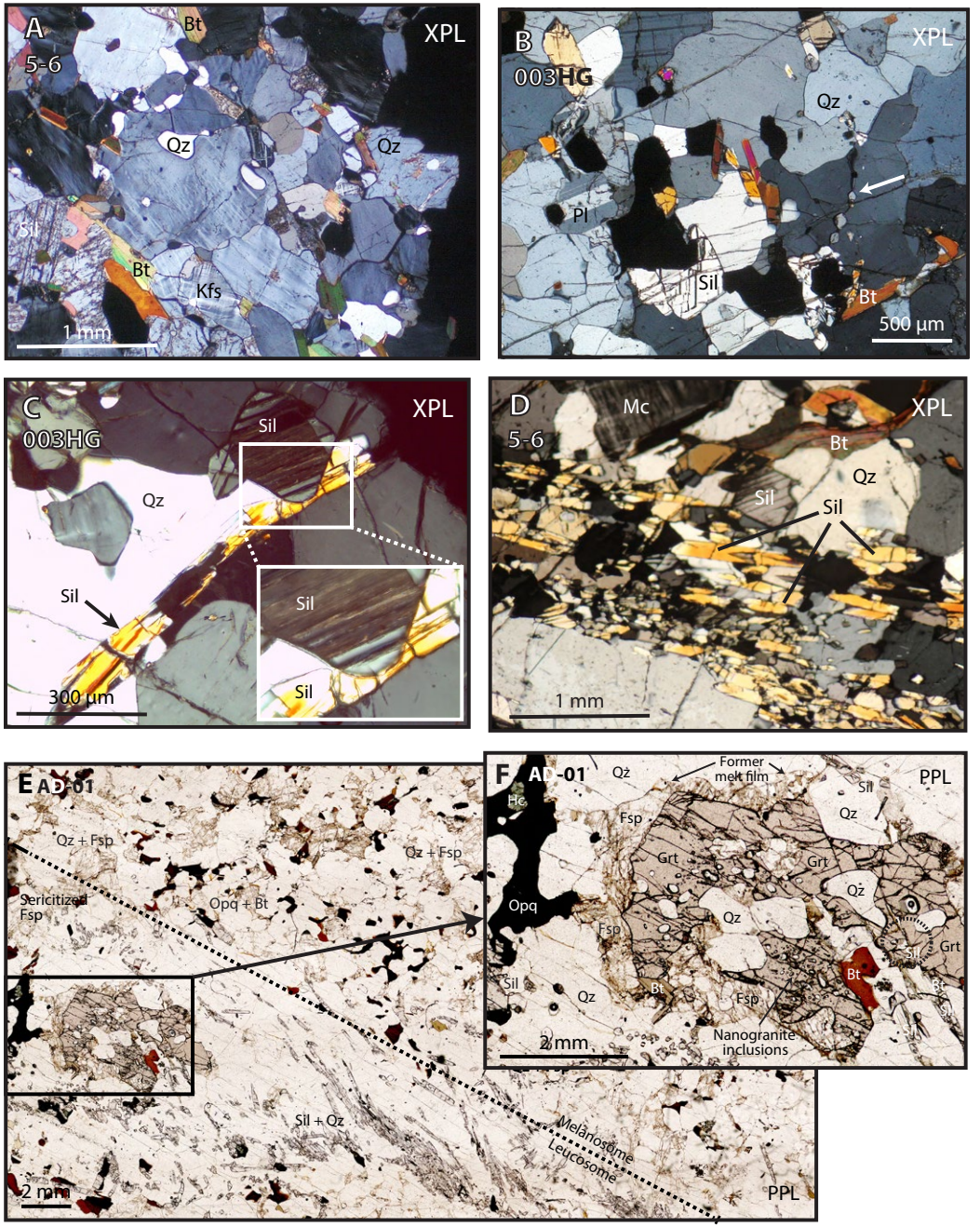


**Figure 5. Photomicrographs showing the mineralogy and textures in Ledge Mountain migmatites. (A) Granoblastic texture showing quartz (Qz) + biotite (Bt) + K-feldspar (Kfs) + sillimanite (Sil) in sample 5-6. (B) Separate crystals of prismatic sillimanite in the migmatite matrix of Qz + Sil + Bt + plagioclase (Pl) in sample 003HG. Arrow points to a quartz "string of beads". (C) Late blocky sillimanite overgrows elongate sillimanite in the granoblastic matrix of sample 003HG. Inset shows an enlargement of the overgrowth. (D) Aligned Sil + Qz layer in a coarse matrix of Qz + microline (Mc) + Bt + Sil in sample 5-6. (E) Part of a thin-section scan of sample AD-01 displaying peritectic garnet (Grt) and aligned Sil + Qz + opaque minerals (Opq) in leucosome. (F) Inset shows garnet with adjacent Opq + hercynite (Hc) cluster; garnet contains nanogranite inclusions and texturally late biotite and sillimanite (in dashed circle). Note feldspar (Fsp) around garnet interpreted to be a former melt film. Mineral abbreviations are after Whitney and Evans (2010). PPL—plane polarized light; XPL—cross-polarized light.**

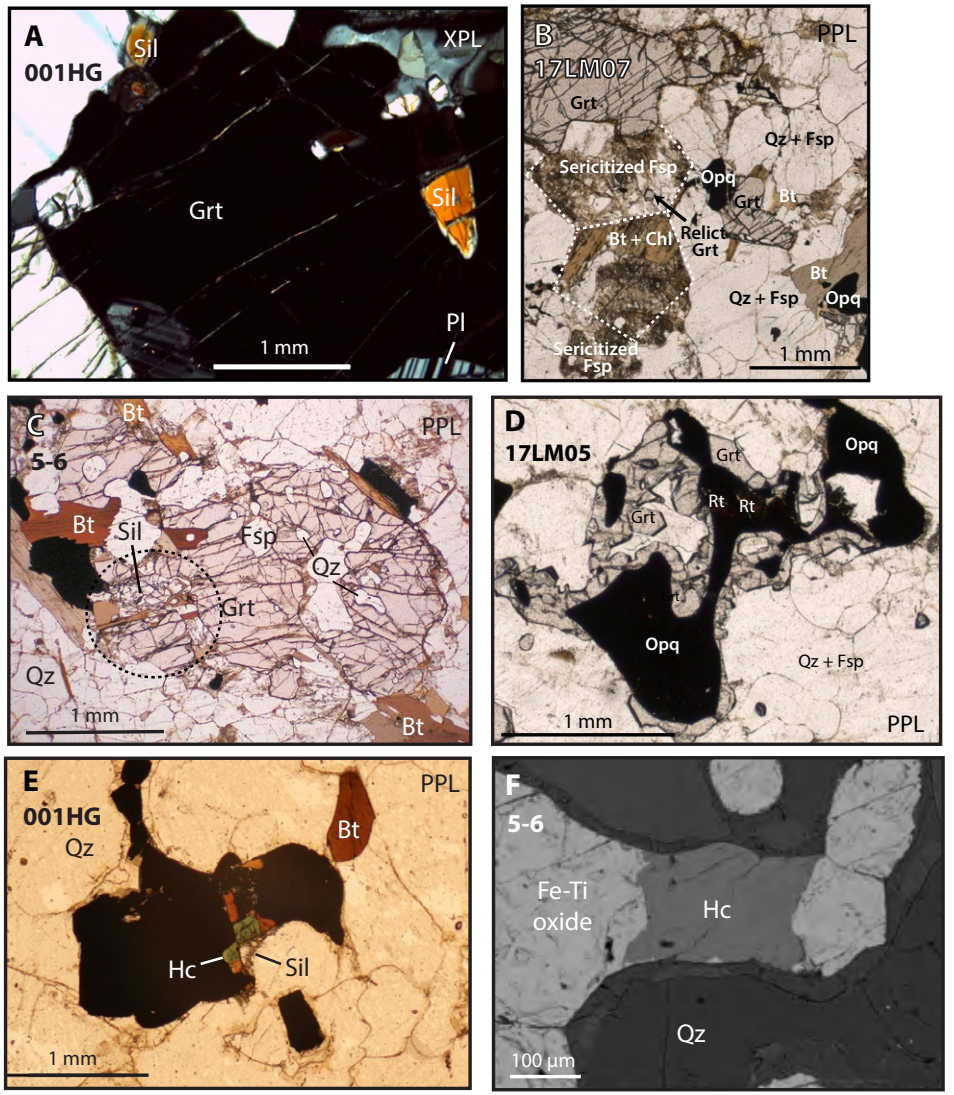


**Figure 6. Photomicrographs of microtextures in Ledge Mountain rocks. (A) Sillimanite (Sil) inclusion in garnet (Grt) in sample 001HG. Pl—plagioclase. (B) Peritectic garnet and garnet pseudomorphs in sample 17LM07 showing replacement feldspar (Fsp) + biotite (Bt) + chlorite (Chl) and small relict garnet. Opq—opaque minerals; Qz—quartz. (C) Peritectic garnet in sample 5-6 with lobate quartz and feldspar inclusions with texturally late biotite. Garnet is being replaced at its edge by biotite and an intergrowth of Bt + Sil + Qz (circled). (D) Sample 17LM05 showing relict rutile (Rt) in ilmenite (shown as Opq) in garnet in a coarse matrix of Qz + Fsp. Fe-Ti oxides are rimmed by garnet. (E) Intergrown hercynite (Hc) and Fe-Ti oxides in sample 001HG showing sillimanite between hercynite and quartz. (F) Backscattered electron (BSE) image showing composite grain of hercynite and Fe-Ti oxides separated from quartz by a rim of plagioclase in sample 5-6. PPL—plane polarized light; XPL—cross-polarized light.**

include rutile, apatite, zircon, monazite, and xenotime. Lenses and layers of sillimanite and quartz ± magnetite ± hercynite are found in some samples (Figs. 5D, 5E). Leucosome and melanosome are commonly interlayered on a microscopic scale (Fig. 5E).

Microcline perthite occurs as medium-grained, typically poikiloblastic, xenoblastic grains with inclusions of quartz, biotite, and opaque minerals (Fig. 5A). Xenoblastic to sub-idioblastic plagioclase feldspar is usually finer-grained than microcline (Figs. 5A, 5B). Plagioclase is also commonly poikiloblastic with inclusions of quartz, biotite, and Fe-Ti oxides. Quartz is medium-grained and rounded in quartzofeldspathic portions of the gneiss (Figs. 5A, 5B) and fine-grained and rounded to elongate in sillimanite-quartz layers (Fig. 5D). Myrmekite is common.

Garnet is scarce (<5%), poikiloblastic, and heterogeneously distributed. Garnet varies in size from <0.1 mm to ~3 cm and occurs both as small scattered crystals and as larger porphyroblasts, some of which appear to be aggregates of smaller grains (Fig. 8B). Larger garnet crystals are typically poikiloblastic and enclose both monomineralic (quartz, biotite, Fe-Ti oxides) and polymineralic inclusions (Figs. 5F, 6B, 6C, 7B). Sillimanite inclusions are scarce (Fig. 6A). Quartz inclusions have rounded or lobate shapes, and some have feldspar rims (former melt films; Figs. 5F, 7B, 7C). Garnet crystals are commonly embayed by intergrowths of biotite + sillimanite + quartz + plagioclase at their edges (Fig. 6C). Garnet also occurs as rims on Fe-Ti oxides (Fig. 6D).

Biotite is found as a matrix mineral with quartz and feldspar (Figs. 5A, 5B, 5E), replacing garnet (Figs. 5E, 5F, 6B, 6C, 7B), and as inclusions in garnet and other phases (Fig. 7B). The timing of matrix biotite crystallization is unclear but appears to be retrograde where biotite is in contact with other Fe-Mg-bearing minerals. Biotite fills fractures in peritectic garnet (e.g., Fig. 6C) and replaces garnet rims, including within garnet embayments, and complete garnet grains in places (Figs. 5F, 6B, 6C, 7C). Biotite also replaces oxide minerals that grew within leucosome (Fig. 6E).

Sillimanite is found in several microstructural settings: (1) as isolated prisms in quartzofeldspathic

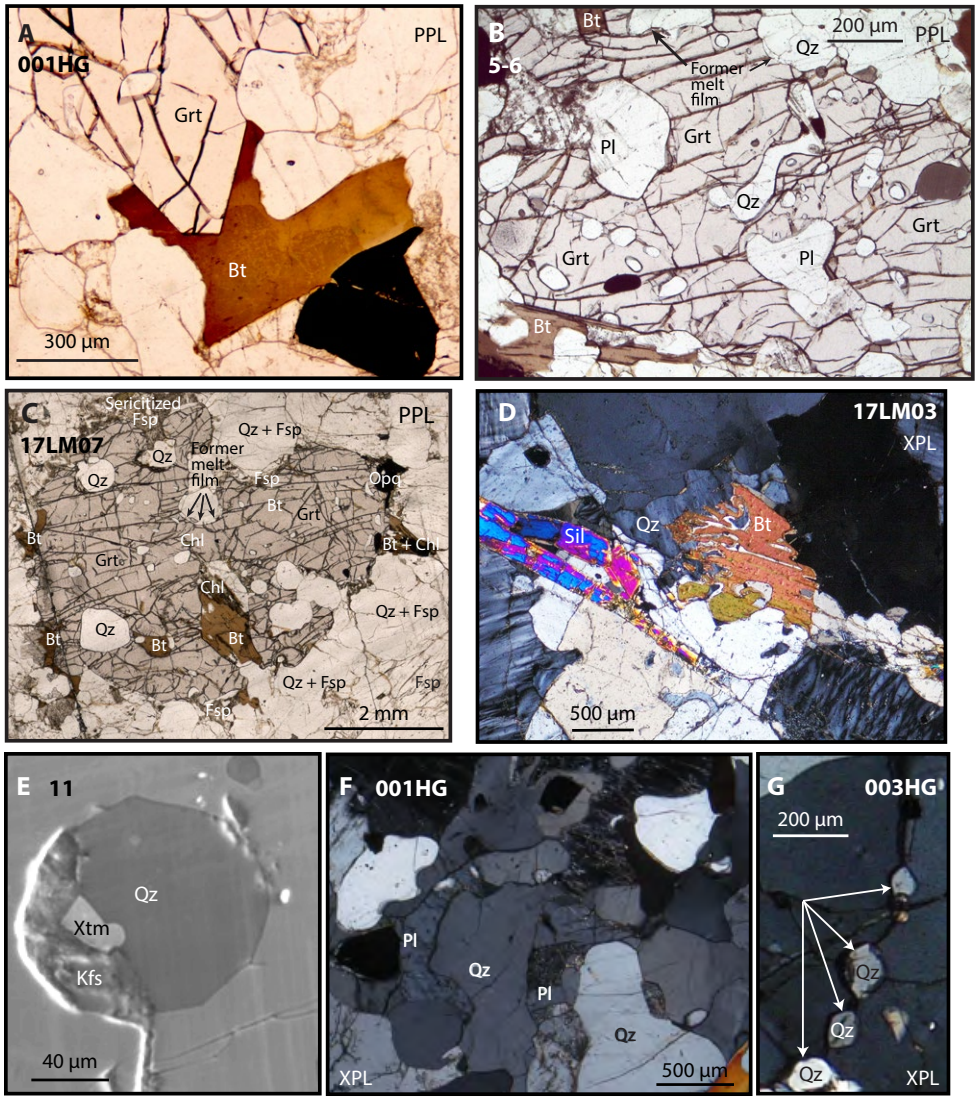


**Figure 7. Photomicrographs showing melt textures in Ledge Mountain migmatites. (A) Euhedral garnet (Grt) face against biotite (Bt) in sample 001HG. (B) Peritectic garnet with lobate quartz (Qz) and feldspar (Pl—plagioclase) inclusions with texturally late biotite in sample 5-6. (C) Peritectic garnet with late biotite in sample 17LM07. Note former melt film inside embayments in garnet. Chl—chlorite; Fsp—feldspar; Opq—opaque minerals. (D) Biotite-quartz symplectite next to an altered sillimanite (Sil) crystal in sample 17LM03. (E) Backscattered electron (BSE) image of a small polyphase "nanogranite" inclusion (Qz + K-feldspar [Kfs] + xenotime [Xtm]) in garnet in sample LM-11. (F) Plagioclase with cuspate boundaries, interpreted as former melt, around quartz in sample 001HG. (G) Quartz "string-of-beads" along grain boundary in sample 003HG. PPL—plane polarized light; XPL—cross-polarized light.**

domains (Figs. 5B, 5C); (2) as inclusions in other minerals; (3) in layers intergrown with quartz ± biotite ± Fe-Ti oxides (Fig. 5E); and (4) as rims on Fe-Ti oxides (Fig. 6E). Two generations of sillimanite growth were observed in some samples (Fig. 5C). Geraghty (1978) reported the presence of kyanite at two locations on Ledge Mountain; however, we have not yet found kyanite in thin section, and, if present, its textural relationship to sillimanite remains uncertain.

Iron-titanium (Fe-Ti) oxides (ilmenite and magnetite) occur in several textural settings: (1) as inclusions in garnet and other phases; (2) intergrown with sillimanite and quartz in sillimanite-quartz segregations (Fig. 5E); and (3) as single oxide minerals or composite aggregates intergrown with biotite and green hercynite in quartzofeldspathic domains (Figs. 6E, 6F). Fe-Ti oxide inclusions are scarce in garnet. Hercynite is found only in association with Fe-Ti oxides and is always separated from quartz by sillimanite, plagioclase, or garnet.

The migmatites enclose pegmatitic leucosomes that reach as much as ~2 m in width and contain quartz and perthitic K-feldspar. Plagioclase concentrations in pegmatitic leucosomes are significantly less than that of K-feldspar. Sillimanite and scarce borosilicates (tourmaline and dumortierite) are also present. Pegmatitic leucosome is surrounded by melanosome, which has the same mineralogy as non-pegmatitic leucosome-adjacent melanosome but is more altered in appearance (i.e., feldspar is sericitized) and contains more biotite (as much as ~12%). Sericitized feldspars, chlorite replacing biotite, altered sillimanite prisms, and minor muscovite are present in both melanosome and pegmatitic leucosome, especially near their mutual contact.

The observed mineral assemblages and textures are consistent with dehydration melting of biotite (Storm and Spear, 2005) to produce melt, with garnet and K-feldspar as peritectic phases:

$$\text{biotite} + \text{aluminosilicate} + \text{quartz} + \text{plagioclase} \rightarrow \text{garnet} + \text{K-feldspar} + \text{melt}. \quad (1)$$

However, this reaction represents only a small fraction of the total melting because biotite percentages

TABLE 1. DESCRIPTIONS OF FIVE REPRESENTATIVE LEDGE MOUNTAIN SAMPLES USED IN MODELING

| Sample number | Coordinates (latitude/longitude) | Mineral assemblage | Approximate melt volume (%) | Mineral compositions |
|---|---|---|---|---|
| Group 1 models | | | | |
| AD-01 | 43°48′38″N, 74°18′32″W | 45% Qz + 20% Pl + 20% Ksp + <4% Bt + <3% Grt + <3% Sil + <1% Ms + <4% (Rt + Ilm + Zrn + Mag ± Hc ± Ap ± Mnz) | 14–42 | Grt: $Alm_{71–75}Sps_{11–13}Prp_{8–9}Grs_{7–8}$; Bt: $X_{Fe57–61}$; Ti (a.p.f.u.): 0.19–0.22; Pl: $An_{43–44}$ |
| 17LM04 | 43°48′37.9″N, 74°18′31.9″W | 45% Qz + 25% Pl + 20% Ksp + <4% Sil + 2% Bt + <2% Grt + <2% (Rt + Ilm + Zrn + Mag ± Hc ± Ap ± Mnz) | 12–49 | Grt: $Alm_{69–73}Sps_{12–15}Prp_{7–8}Grs_{7–8}$; Bt: $X_{Fe43–55}$; Ti (a.p.f.u.): 0.11–0.17; Pl: $An_{42–43}$ |
| 11 | 43°48′36.36″N, 74°18′33.31″W | 50% Pl + 45% Qz + <2% Grt + <1% Sil + <1% Bt + <<1% Ms + 1% (Rt + Ilm + Zrn + Mag ± Hc ± Ap ± Mnz) | 9–20 | Grt: $Alm_{65–71}Sps_{13–15}Prp_{5–17}Grs_{6–7}$; Bt: $X_{Fe42–67}$; Ti (a.p.f.u.): 0.09–0.21; Pl: $An_{28–47}$ |
| Group 2 models | | | | |
| 5-6 | 43°48′36.44″N, 74°18′36.67″W | 40% Ksp + 30% Qz + 20% Pl + <4% Bt + <2% Sil + <1% Grt + <3% (Rt + Ilm + Zrn + Mag ± Hc ± Ap ± Mnz) | 15–50 | Grt: $Alm_{69–70}Sps_{15–16}Prp_{10}Grs_{5}$; Bt: $X_{Fe43–55}$; Ti (a.p.f.u.): 0.11–0.17; Pl: $An_{29–33}$ |
| 001HG | 43°48′39.06″N, 74°18′36.66″W | 60% Ksp + 30% Qz + <3% Grt + <1% Pl + <2% Bt + <3% (Rt + Ilm + Zrn + Mag ± Hc ± Ap ± Mnz) | 30 | Grt: $Alm_{67–74}Sps_{14–15}Prp_{6–12}Grs_{5–7}$; Bt: $X_{Fe53–63}$;Ti (a.p.f.u.): 0.14–0.23; Pl: $An_{35–36}$ |

*Note:* Melt percentages taken from the intersection of melt isomodes with the peak assemblage fields for each sample as in Figure 13. Mineral abbreviations after Whitney and Evans (2010): Alm—almandine; Ap—apatite; Bt—biotite; Grs—grossular; Grt—garnet; Hc—hercynite; Ilm—ilmenite; Ksp—K-feldspar; Mag—magnetite, Mnz—monazite; Ms—muscovite; Pl—plagioclase; Prp—pyrope; Qz—quartz; Rt—rutile; Sil—sillimanite; Sps—spessartine; Zrn—zircon. a.p.f.u.—atoms per formula unit.

are so low; decompression melting must have also played a significant role during exhumation (see Discussion).

Textural evidence for the presence of former melt (e.g., Waters, 2001; Holness and Sawyer, 2008; Holness et al., 2011) is abundant in the Ledge Mountain samples and includes: (1) euhedral crystal faces against former melt (Fig. 7A); (2) numerous rounded to lobate quartz inclusions of quartz in garnet (Figs. 5F, 6B, 6C, 7B) that are inferred to be a result of peritectic garnet growth during dehydration melting (Waters, 2001; Guilmette et al., 2011; Groppo et al., 2012); (3) biotite-quartz symplectites (Fig. 7D), which Waters (2001) interpreted to form during crystallization of a melt; (4) very small polyphase inclusions in garnet (Fig. 7E), which may represent melt inclusions or "nanogranites" similar to those reported in migmatites from the western Adirondack Highlands (Darling, 2013) and from other migmatite terranes (e.g., Sawyer et al., 2011; Bartoli et al., 2015, 2016; Cesare et al., 2015); and (5) textures consistent with pseudomorphs of melt-filled pores (e.g., Holness and Sawyer, 2008, and references therein; Guilmette et al., 2011; Groppo et al., 2012). These include films of feldspar and/or quartz on other phases, interstitial grains with cuspate boundaries, and quartz "string of beads" textures (Figs. 5B, 7G), which represent polycrystalline replacement of grain-boundary melt (Holness and Sawyer, 2008).

Resorption of garnet rims by biotite ± sillimanite ± plagioclase ± quartz suggests reversal of Reaction 1 and back-reaction during cooling and melt crystallization (Waters, 2001). Other evidence for retrogression includes sericitized feldspars (Fig. 6B), retrograde biotite and corroded sillimanite (Fig. 7D), garnet rims replaced by biotite-plagioclase-sillimanite intergrowths (Fig. 6C), replacement of biotite by chlorite (Fig. 6B), and small amounts of muscovite.

Complex intergrowths of Fe-Ti-Al oxides are similar to those reported for UHT aluminous granulites from the Eastern Ghats belt of India (Sengupta et al., 1999; Bose et al., 2009; Das et al., 2017). The diverse and complicated textural relationships among oxide minerals in Ledge Mountain rocks have not yet been thoroughly investigated, but reconnaissance microprobe analysis shows that both ilmenite and magnetite are present as opaque minerals. Ilmenite commonly exhibits exsolution lamellae of hematite. Green hercynitic spinel is found in aggregates with magnetite and ilmenite (Figs. 6E, 6F). Similar spinel-bearing oxide aggregates found in rocks of the Eastern Ghats belt have been interpreted as secondary breakdown products of a primary Ti-Mg-Fe-Al spinel formed during cooling (Sengupta et al., 1999; Bose et al., 2009; Das et al., 2017). Hercynite is separated from quartz by coronae of garnet or sillimanite (Fig. 6E), suggesting retrograde reversal of the reaction (Dasgupta et al., 1995):

$$\text{spinel} + \text{quartz} \rightarrow \text{garnet} + \text{sillimanite}. \quad (2)$$

Locally, plagioclase also separates hercynite from quartz.

## SAMPLE SELECTION, ANALYTICAL METHODS, AND RESULTS

Samples of migmatites including leucosome-melanosome pairs were collected over the course of several field seasons (Fig. 4). Thirty-eight (38) samples were analyzed for whole-rock geochemistry and were modeled using Perple_X software (Connolly, 2005, 2009). Based on detailed petrographic study and initial modeling results, a

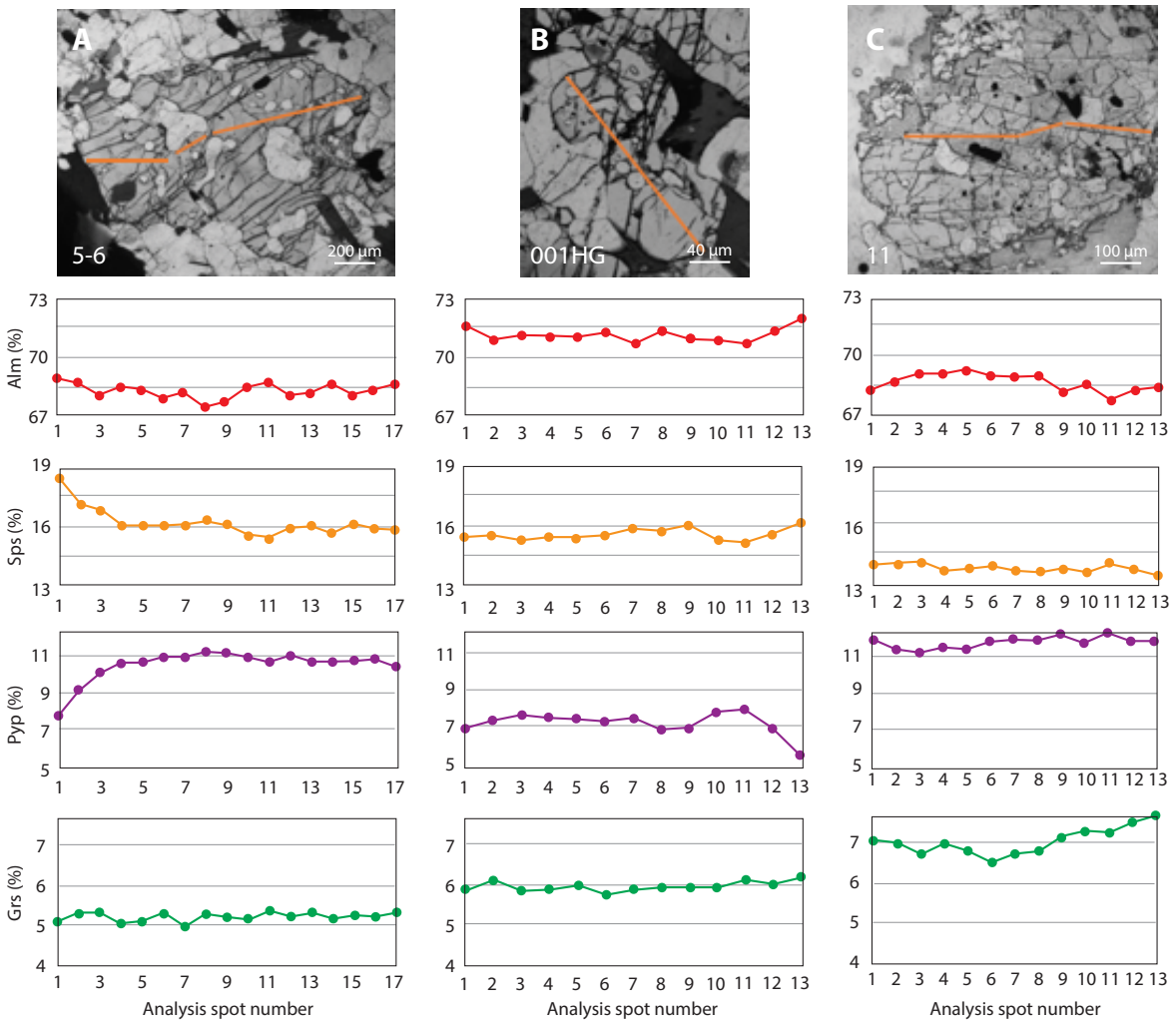


**Figure 8. Garnet zoning profiles for samples 5-6 (A), 001HG (B), and LM-11 (C). Percentage of garnet end-member compositions are shown in red (Alm—almandine), orange (Sps—spessartine), purple (Pyp—pyrope), and green (Grs—grossular). Analysis spot numbers correspond to points along the orange profile line shown on the photomicrographs at the top. Samples 5-6 and 001HG show an inverse relationship between the pyrope and spessartine-almandine end members.**

representative subset of five of these samples was selected for further study (samples 5-6, 001HG, 11, AD-01, and 17LM04). Six samples (001HG, 004HG, 005HG, 006HG, 007HG, and 008HG) were chosen for U-Pb SHRIMP and trace element analysis of zircon. Mineral compositions were collected for samples 5-6, 001HG, 11, AD-01, and 17LM04.

## Mineral Compositions

Representative electron microprobe analyses for samples used in pseudosection models are presented in Tables 2–5, and summaries are included in Table 1. Mineral abbreviations are from Whitney and Evans (2010). Mineral composition analyses were performed on the JEOL JXA-8239 "SuperProbe" or the JEOL 733 electron microprobe at the Stanford University Mineral and Microchemical Analysis Facility (Stanford, California, USA) for incorporation into our pseudosection models (Tables 2–5). Operating conditions were 15 keV accelerating voltage and 15 nA beam current with 20 s counting time. Mineral composition data for select phases were collected in order to investigate possible chemical zoning in garnet and other phases. Compositional isopleths in our models were correlated to these mineral composition analyses to better constrain *P-T* conditions for Ledge Mountain rocks.

### *Garnet*

Peritectic garnet is almandine-rich ($Alm_{66–75}Sps_{11–16}Pyp_{7–13}Grs_{5–8}$ [Alm—almandine; Grs—grossular; Pyp—pyrope; Sps—spessartine; values are garnet end-member percentages]). Major element zoning in garnets appears weak based on electron

TABLE 2. REPRESENTATIVE GARNET ANALYSES

| Sample number | 5-6 | | AD01 | | 17LM04 | | 001HG | | 11 | |
|---|---|---|---|---|---|---|---|---|---|---|
| Location | Core | Rim | Core | Rim | Core | Rim | Core | Rim | Core | Rim |
| Oxides (wt%) | | | | | | | | | | |
| $SiO_2$ | 37.60 | 37.70 | 37.13 | 37.10 | 37.22 | 36.98 | 36.63 | 36.46 | 36.09 | 36.61 |
| $TiO_2$ | 0.00 | 0.03 | 0.01 | 0.02 | 0.02 | 0.03 | 0.03 | 0.02 | 0.02 | 0.02 |
| $Al_2O_3$ | 21.39 | 21.22 | 20.76 | 20.68 | 20.71 | 20.68 | 21.26 | 20.96 | 20.49 | 20.60 |
| $Cr_2O_3$ | 0.00 | 0.05 | 0.06 | 0.01 | –0.01 | 0.02 | 0.00 | –0.01 | 0.00 | 0.01 |
| FeO | 30.73 | 31.36 | 31.50 | 31.41 | 30.55 | 30.12 | 31.71 | 32.41 | 29.96 | 29.76 |
| MnO | 6.76 | 7.03 | 5.22 | 4.96 | 6.01 | 5.98 | 6.36 | 6.41 | 6.37 | 6.24 |
| MgO | 2.51 | 2.42 | 2.11 | 2.02 | 2.17 | 2.13 | 2.42 | 1.83 | 3.15 | 3.08 |
| CaO | 1.83 | 1.82 | 2.45 | 2.51 | 2.50 | 2.63 | 2.05 | 2.00 | 2.32 | 2.59 |
| $Na_2O$ | 0.07 | 0.06 | 0.02 | 0.02 | 0.02 | 0.02 | 0.02 | 0.03 | 0.00 | –0.02 |
| $K_2O$ | 0.00 | 0.01 | 0.00 | 0.02 | 0.01 | 0.05 | –0.15 | –0.20 | –0.17 | –0.16 |
| Sum | 100.90 | 101.7 | 99.27 | 98.78 | 99.17 | 98.65 | 100.33 | 99.90 | 98.23 | 98.72 |
| Cations based on 12 atoms of oxygen | | | | | | | | | | |
| Si | 3.00 | 3.00 | 3.018 | 3.028 | 3.025 | 3.021 | 2.96 | 2.97 | 2.97 | 2.99 |
| Ti | 0.00 | 0.00 | 0.001 | 0.001 | 0.001 | 0.002 | 0.00 | 0.00 | 0.2 | 0.23 |
| Al | 2.01 | 1.99 | 1.990 | 1.990 | 1.984 | 1.992 | 2.03 | 2.01 | 1.99 | 1.98 |
| Cr | 0.00 | 0.00 | 0.004 | 0.001 | -0.001 | 0.001 | 0.00 | 0.00 | 0.00 | 0.00 |
| Fe | 2.05 | 2.09 | 2.141 | 2.144 | 2.076 | 2.058 | 2.14 | 2.21 | 2.06 | 2.03 |
| Mn | 0.46 | 0.47 | 0.359 | 0.343 | 0.414 | 0.414 | 0.44 | 0.44 | 0.44 | 0.43 |
| Mg | 0.30 | 0.29 | 0.256 | 0.246 | 0.263 | 0.259 | 0.29 | 0.22 | 0.386 | 0.374 |
| Ca | 0.16 | 0.15 | 0.213 | 0.220 | 0.218 | 0.231 | 0.18 | 0.17 | 0.20 | 0.23 |
| Na | 0.01 | 0.01 | 0.003 | 0.003 | 0.003 | 0.003 | 0.00 | 0.00 | 0.00 | 0.00 |
| K | 0.00 | 0.00 | 0.000 | 0.002 | 0.001 | 0.005 | –0.02 | –0.02 | –0.02 | –0.02 |
| Sum | 19.99 | 20.01 | 18.986 | 18.978 | 18.984 | 18.985 | 20.02 | 20.02 | 20.03 | 20.01 |
| End-member calculations | | | | | | | | | | |
| Almandine (%) | 69.20 | 69.49 | 72.10 | 72.61 | 69.90 | 69.48 | 70.30 | 72.46 | 66.6 | 66.32 |
| Spessartine (%) | 15.43 | 15.79 | 12.10 | 11.61 | 13.93 | 13.98 | 14.28 | 14.51 | 14.32 | 14.08 |
| Pyrope (%) | 10.08 | 9.55 | 8.63 | 8.34 | 8.85 | 8.75 | 9.58 | 7.32 | 12.48 | 12.22 |
| Grossular (%) | 5.29 | 5.16 | 7.19 | 7.44 | 7.33 | 7.79 | 5.84 | 5.71 | 6.60 | 7.38 |

*Note*: Negative values indicate determinations less than the detection limit of the analytical method.

microprobe point traverses (Fig. 8; Table 2), and compositional X-ray maps reveal no zoning (not shown). Garnet cores are compositionally homogeneous or weakly and irregularly zoned. Minor variations in major element concentrations are observed at garnet rims (<2%–3%). The grain transect of sample 5-6 (Fig. 8A) gives evidence of Mn increase and corresponding Mg decrease of as much as ~3% in garnet rims compared to cores. Sample 001HG (Fig. 8B) is similar to sample 5-6, showing an increase in both Fe and Mn of ~2% in garnet rims correlating to a 3% decrease in Mg. No consistent patterns are evident, but some garnets look like composite rather than single grains, so patterns might reflect that complexity (see Fig. 8B).

TABLE 3. REPRESENTATIVE PLAGIOCLASE ANALYSES

| Sample number | 5-6 | | AD-01 | | 17LM04 | | HW-LM-001HG | | |
|---|---|---|---|---|---|---|---|---|---|
| Location | Core | Rim | Core | Rim | Core | Rim | Inclusion | Core | Rim |
| Oxides (wt%) | | | | | | | | | |
| $SiO_2$ | 60.06 | 61.75 | 57.13 | 57.06 | 57.46 | 57.40 | 58.35 | 58.45 | 58.22 |
| $TiO_2$ | 0.02 | 0.04 | 0.00 | 0.00 | 0.00 | 0.00 | 0.01 | 0.02 | 0.01 |
| $Al_2O_3$ | 26.57 | 26.24 | 26.95 | 27.02 | 26.53 | 26.70 | 25.58 | 25.74 | 25.40 |
| FeO | 0.00 | 0.05 | 0.02 | 0.02 | 0.03 | 0.04 | 0.14 | 0.15 | 0.05 |
| MgO | 0.00 | 0.02 | 0.00 | –0.01 | 0.00 | 0.00 | 0.00 | 0.02 | 0.00 |
| CaO | 7.09 | 6.22 | 8.97 | 9.14 | 8.84 | 8.82 | 7.75 | 7.53 | 7.82 |
| $Na_2O$ | 7.64 | 8.36 | 6.25 | 6.26 | 6.61 | 6.51 | 7.45 | 7.12 | 7.34 |
| $K_2O$ | 0.27 | 0.14 | 0.26 | 0.16 | 0.19 | 0.16 | 0.14 | 0.74 | 0.25 |
| Sum | 101.7 | 102.9 | 99.59 | 99.64 | 99.66 | 99.64 | 99.44 | 99.74 | 99.07 |
| Cations based on 8 atoms of oxygen | | | | | | | | | |
| Si | 2.64 | 2.67 | 2.57 | 2.57 | 2.58 | 2.58 | 2.63 | 2.63 | 2.63 |
| Ti | 0.00 | 0.00 | 0.00 | 0.00 | 0.00 | 0.00 | 0.00 | 0.00 | 0.00 |
| Al | 1.37 | 1.34 | 1.43 | 1.43 | 1.41 | 1.42 | 1.36 | 1.36 | 1.35 |
| Fe | 0.00 | 0.00 | 0.00 | 0.00 | 0.00 | 0.00 | 0.01 | 0.01 | 0.00 |
| Mg | 0.00 | 0.00 | 0.00 | 0.00 | 0.00 | 0.00 | 0.00 | 0.00 | 0.00 |
| Ca | 0.33 | 0.29 | 0.43 | 0.44 | 0.43 | 0.43 | 0.37 | 0.36 | 0.38 |
| Na | 0.65 | 0.70 | 0.55 | 0.55 | 0.58 | 0.57 | 0.65 | 0.62 | 0.64 |
| K | 0.01 | 0.01 | 0.02 | 0.01 | 0.01 | 0.01 | 0.01 | 0.04 | 0.01 |
| Sum | 13.01 | 13.01 | 12.99 | 12.99 | 13.01 | 13.00 | 13.02 | 13.02 | 13.02 |
| End-member calculations | | | | | | | | | |
| Albite % | 65.1 | 70.4 | 54.91 | 54.86 | 56.86 | 56.66 | 63.0 | 60.4 | 62.1 |
| Anorthite % | 33.4 | 28.9 | 43.56 | 44.24 | 42.04 | 42.43 | 36.2 | 35.4 | 36.6 |
| Orthoclase % | 1.5 | 0.8 | 1.53 | 0.90 | 1.11 | 0.91 | 0.78 | 4.19 | 1.35 |

*Note*: Negative value indicates determination less than the detection limit of the analytical method.

### *Feldspars*

Matrix plagioclase ranges in composition from $An_{29}$ to $An_{44}$ (An—anorthite; Table 3). Plagioclase rims on Fe-Ti oxides are more sodic (~$An_{2–8}$). Most plagioclase grains are homogeneous, but a few show slight zoning (~2%–3% An), with rims both enriched and depleted in calcium relative to the cores (Table 3). Plagioclase rims on a quartz inclusion within garnet in sample 5-6 are similar in composition ($An_{32}$) to matrix plagioclase. Integrated perthitic K-feldspar compositions vary from $Or_{84}$ to $Or_{90}$ (Or—orthoclase).

### *Biotite*

Biotite has variable compositions, with mole fraction of Fe ($X_{Fe}$) values for matrix biotite ranging from 0.43 to 0.63 and Ti from 0.09 to 0.23 atoms per formula unit (a.p.f.u.) (Table 4 gives a selection of representative data). Biotite inclusions in garnet are more magnesian than matrix biotite but have less Ti (Table 4).

### *Fe-Ti-Al Oxides*

The oxide minerals in Ledge Mountain migmatites show complex intergrowths and exsolution textures. Reconnaissance microprobe analysis has verified the presence of both ilmenite and magnetite; representative analyses are included in Table 5. Rutile occurs as inclusions in garnet and Fe-Ti oxides. Green spinel is hercynitic and contains variable amounts of ZnO (9.23–12.45 wt% in sample 5-6; 2.51–2.73 wt% in sample 001HG). Spinel has low $Fe^{3+}$ (0.00–0.05 a.p.f.u.) and contains negligible $Cr_2O_3$.

## Whole-Rock Geochemistry

Whole-rock geochemical analyses were performed on all samples by X-ray fluorescence (XRF) and inductively coupled plasma mass spectrometry (ICP-MS) at the GeoAnalytical Lab at Washington State University (Pullman, Washington, USA). Johnson et al. (1999) presented a discussion of the precision and accuracy of these methods.

Whole-rock major and selected trace element analyses for the five Ledge Mountain migmatite samples used for thermodynamic modeling are summarized in Table 6 and plotted in Figures 9 and 10; analyses for the Hawkeye Granite (Valley et al., 2011) and the least-altered phase of the Lyon Mountain Granite (perthite granite of Valley et al. [2011]) are included for comparison.

### *Major Element Characteristics*

The majority of the analyzed Ledge Mountain migmatite samples have granitic compositions, but three are tonalitic and one plots in the granodiorite field. Four of the five samples selected

for pseudosection modeling plot as granite on an Ab-An-Or diagram (Ab—albite; Fig. 9A) and have a limited range of $SiO_2$ (66.11 to 71.71 wt%). They are K rich ($K_2O$ = 3.59–6.24 wt%), are strongly peraluminous (A/CKN >1.1 [molecular ratio of $Al_2O_3$/($CaO + Na_2O + K_2O$)]; Fig. 9B), range from alkali calcic to calcic (Fig. 9C), and are ferroan [FeO/(FeO + MgO) = 0.89–0.96] according to terminology of Frost and Frost (2008; Fig. 9D). The fifth sample used for phase equilibrium modeling, sample 11, is a meta-leucotonalite.

TABLE 4. REPRESENTATIVE BIOTITE ANALYSES

| Sample | 5-6 | | | AD-01 | | 17LM04 | | HW-LM-001HG | |
|---|---|---|---|---|---|---|---|---|---|
| Location | matrix | incl.* | adj.† | matrix | matrix | matrix | matrix | matrix | adj.† |
| Oxides (wt%) | | | | | | | | | |
| $SiO_2$ | 36.59 | 37.35 | 37.00 | 36.24 | 36.99 | 36.29 | 36.72 | 35.73 | 35.51 |
| $TiO_2$ | 3.10 | 2.23 | 1.90 | 3.79 | 3.50 | 3.26 | 3.30 | 2.82 | 3.18 |
| $Al_2O_3$ | 18.59 | 17.87 | 18.42 | 16.18 | 16.27 | 16.52 | 16.56 | 16.30 | 16.20 |
| $Cr_2O_3$ | 0.00 | 0.00 | 0.01 | 0.00 | 0.01 | 0.02 | 0.03 | 0.01 | 0.01 |
| FeO | 19.48 | 16.78 | 16.23 | 20.93 | 20.55 | — | — | 19.10 | 19.25 |
| MnO | 0.20 | 0.09 | 0.08 | 0.13 | 0.14 | 20.20 | 20.12 | 0.07 | 0.09 |
| MgO | 8.87 | 11.91 | 11.53 | 7.58 | 8.27 | 0.31 | 0.24 | 9.33 | 9.35 |
| CaO | 0.01 | 0.03 | 0.08 | 0.01 | –0.01 | 7.95 | 8.23 | -0.01 | -0.03 |
| $Na_2O$ | 0.12 | 0.15 | 0.15 | 0.09 | 0.07 | 0.01 | –0.01 | 0.08 | 0.09 |
| $K_2O$ | 9.65 | 9.82 | 9.81 | 9.24 | 9.04 | 0.09 | 0.10 | 10.21 | 10.12 |
| Sum | 96.59 | 96.24 | 95.21 | 94.33 | 95.00 | 9.00 | 9.36 | 93.63 | 93.77 |
| Cations based 11 atoms of oxygen | | | | | | | | | |
| Si | 2.74 | 2.78 | 2.77 | 2.81 | 2.84 | 2.82 | 2.82 | 2.79 | 2.77 |
| Ti | 0.17 | 0.12 | 0.11 | 0.22 | 0.20 | 0.19 | 0.19 | 0.17 | 0.19 |
| Al | 1.64 | 1.57 | 1.63 | 1.48 | 1.47 | 1.51 | 1.50 | 1.50 | 1.49 |
| Cr | 0.00 | 0.00 | 0.00 | 0.00 | 0.00 | 0.00 | 0.00 | 0.00 | 0.00 |
| Fe | 1.22 | 1.04 | 1.02 | 1.36 | 1.32 | 1.31 | 1.29 | 1.25 | 1.26 |
| Mn | 0.01 | 0.01 | 0.01 | 0.01 | 0.01 | 0.02 | 0.02 | 0.01 | 0.01 |
| Mg | 0.99 | 1.32 | 1.29 | 0.88 | 0.94 | 0.92 | 0.94 | 1.08 | 1.09 |
| Ca | 0.00 | 0.00 | 0.01 | 0.00 | 0.00 | 0.00 | 0.00 | 0.00 | 0.00 |
| Na | 0.02 | 0.02 | 0.02 | 0.01 | 0.01 | 0.01 | 0.01 | 0.01 | 0.01 |
| K | 0.92 | 0.93 | 0.94 | 0.92 | 0.88 | 0.89 | 0.92 | 1.02 | 1.01 |
| Sum | 18.73 | 18.79 | 18.79 | 18.69 | 18.67 | 18.69 | 18.70 | 18.81 | 18.81 |
| End-member calculations | | | | | | | | | |
| Phlogopite ($X_{Mg}$) | 44.8 | 55.86 | 55.87 | 39.29 | 41.80 | 41.26 | 42.15 | 46.52 | 46.39 |
| Annite ($X_{Fe}$) | 55.2 | 44.14 | 44.13 | 60.71 | 58.31 | 58.74 | 57.85 | 53.48 | 53.61 |

*Note*: Negative values indicate determinations less than the detection limit of the analytical method; dashes indicate values not determined.
*Inclusion in garnet.
†Adjacent to garnet.

### *Trace Element Characteristics*

Chondrite-normalized whole-rock rare-earth element (REE) patterns for Ledge Mountain migmatites, the Hawkeye Granite, and the Lyon Mountain Granite are plotted in Figure 10A. The patterns for the granitic Ledge Mountain migmatites and Lyon Mountain Granite are broadly similar and show light REE enrichment ($La_N/Yb_N$ = 5.03–6.61; N—normalized) and a negative Eu anomaly [Eu/Eu* = $Eu_N/(Sm_N \times Gd_N)^{0.5}$]. Patterns for the granitic Ledge Mountain migmatites also resemble those for the Lyon Mountain Granite on a primitive mantle–normalized multi-element diagram and show enrichment in large-ion lithophile elements (Rb, Th, K) and depletion in high-field-strength elements (Nb, Sr, P, Ti) (Fig. 10B). Meta-leucotonalite sample 11 shows elevated heavy REEs (HREEs; Fig. 10A) compared to the granitic samples.

Rare earth element patterns for Ledge Mountain pegmatitic leucosome and surrounding melanosome are shown in Figure 10C. The pegmatitic leucosome and melanosome patterns are broadly similar, with the exception of two pegmatitic leucosome samples that have lower total REEs and positive Eu anomalies suggesting feldspar accumulation. Ledge Mountain migmatite samples, Lyon Mountain Granite, and Hawkeye Granite plot in the A-type granite field on the Zr versus $10^4 \times Ga/Al$ diagram of Whalen et al. (1987; Fig. 10D) and in the within-plate granite field on the Rb versus Y + Nb diagram of Pearce et al. (1984; Fig. 10E). Sample 11 meta-leucotonalite is similar to the granites in Figure 10D also plotting in the A-type granite field, but sample 11 plots in the ocean ridge granite field in Figure 10E.

### *Nature of the Protolith*

The chemical similarity of Ledge Mountain migmatites and the least-altered Lyon Mountain Granite samples suggests that, like the Lyon Mountain Granite, Ledge Mountain migmatites had an igneous protolith. However, the difficulty of identifying a protolith in high-grade metamorphic rocks is widely acknowledged, particularly for aluminous felsic granulites, which may be derived from either Al-rich sedimentary materials or by melting of igneous rocks (e.g., Turpin et al., 1990; Ownby et al., 2004). Although unequivocal identification of a protolith is not possible, chemical discriminant plots have been used to distinguish igneous from sedimentary protoliths (Ownby et al., 2004; Hasterok et al., 2019). The majority of the granitic Ledge Mountain migmatites plot in the igneous field on the $P_2O_5/TiO_2$ versus MgO/CaO diagram of Werner (1987; Fig. 9E).

TABLE 5. REPRESENTATIVE SPINEL ANALYSES

| Sample number | 5-6 | 5-6 | 5-6 | 001HG | 001HG |
|---|---|---|---|---|---|
| Oxides (wt%) | | | | | |
| $SiO_2$ | 3.18 | 0.00 | 0.01 | 0.00 | 0.00 |
| $TiO_2$ | 0.00 | 0.00 | 0.00 | 3.95 | 4.47 |
| $Al_2O_3$ | 52.96 | 57.90 | 57.92 | 61.46 | 62.97 |
| $Cr_2O_3$ | 0.00 | 0.00 | 0.01 | 0.02 | 0.01 |
| FeO | 23.61 | 25.43 | 27.02 | 25.85 | 24.46 |
| MnO | 1.18 | 1.45 | 1.79 | 0.66 | 0.61 |
| MgO | 2.23 | 2.57 | 2.69 | 1.86 | 1.76 |
| CaO | 0.12 | 0.00 | 0.02 | 0.00 | 0.00 |
| ZnO | 12.21 | 12.45 | 9.76 | 2.73 | 2.68 |
| Sum | 96.05 | 100.13 | 99.50 | 96.94 | 97.38 |
| Cations based on 4 atoms of oxygen | | | | | |
| Si | 0.10 | 0.00 | 0.00 | 0.00 | 0.00 |
| Ti | 0.00 | 0.00 | 0.00 | 0.09 | 0.10 |
| Al | 1.90 | 1.97 | 1.98 | 2.12 | 2.16 |
| Cr | 0.00 | 0.00 | 0.00 | 0.00 | 0.00 |
| $Fe^{3+}$ | 0.00 | 0.03 | 0.02 | 0.00 | 0.00 |
| $Fe^{2+}$ | 0.60 | 0.59 | 0.63 | 0.63 | 0.59 |
| Mn | 0.03 | 0.04 | 0.04 | 0.02 | 0.02 |
| Mg | 0.10 | 0.11 | 0.12 | 0.08 | 0.08 |
| Ca | 0.00 | 0.00 | 0.00 | 0.00 | 0.00 |
| Zn | 0.27 | 0.27 | 0.21 | 0.06 | 0.06 |
| Sum | 3.00 | 3.00 | 3.00 | 3.00 | 3.00 |

TABLE 6. WHOLE-ROCK X-RAY FLUORESCENCE AND INDUCTIVELY COUPLED PLASMA MASS SPECTROMETRY MAJOR AND TRACE ELEMENT ANALYSES FOR REPRESENTATIVE LEDGE MOUNTAIN MIGMATITES USED IN MODELING

| Sample number | Group 1 | | | Group 2 | |
|---|---|---|---|---|---|
| | AD-01a | 17LM04 | 11 | 5-6 | 001HG |
| Unnormalized major elements (wt%) | | | | | |
| $SiO_2$ | 71.710 | 69.340 | 71.880 | 66.110 | 70.040 |
| $TiO_2$ | 0.590 | 0.640 | 0.422 | 0.612 | 0.496 |
| $Al_2O_3$ | 14.080 | 15.420 | 14.690 | 15.890 | 13.720 |
| FeO* | 4.530 | 4.720 | 3.850 | 5.050 | 4.740 |
| MnO | 0.077 | 0.089 | 0.417 | 0.148 | 0.034 |
| MgO | 0.500 | 0.560 | 0.370 | 0.330 | 0.520 |
| CaO | 1.940 | 1.930 | 3.470 | 2.010 | 1.160 |
| $Na_2O$ | 1.780 | 1.760 | 2.680 | 2.830 | 1.950 |
| $K_2O$ | 3.590 | 3.990 | 0.810 | 5.300 | 6.240 |
| $P_2O_5$ | 0.109 | 0.122 | 0.200 | 0.122 | 0.101 |
| Sum M | 98.900 | 98.570 | 98.790 | 98.402 | 99.020 |
| LOI % | 0.630 | 0.760 | 0.530 | 0.440 | — |
| Unnormalized trace elements (ppm) | | | | | |
| Ni | 0 | 4 | 4 | 3 | 1 |
| Cr | 2 | 4 | 9 | 7 | 5 |
| Sc | 8 | 7 | 29 | 7 | 6 |
| V | 6 | 9 | 8 | 7 | 7 |
| Ba | 660 | 741 | 116 | 1708 | 1020 |
| Rb | 138 | 147 | 22 | 157 | 192 |
| Sr | 124 | 134 | 104 | 212 | 156 |
| Zr | 789 | 842 | 623 | 820 | 693 |
| Y | 83 | 87 | 280 | 117 | 73 |
| Nb | 28 | 30 | 26.7 | 30 | 25 |
| Ga | 25 | 27 | 19 | 31 | 26 |
| Cu | 0 | 1 | 1 | 2 | 1 |
| Zn | 180 | 177 | 28 | 120 | 25 |
| Pb | 21 | 22 | 6 | 20 | 10 |
| La | 84 | 69 | 42 | 94 | 83 |
| Ce | 177 | 152 | 93 | 205 | 173 |
| Th | 15 | 13 | 6 | 21 | 17 |
| Nd | 87 | 73 | 48 | 101 | 88 |
| U | 5 | 4 | 3 | 7 | 3 |
| Sum Tr | 2432 | 2543 | 1467 | 3669 | 2604 |
| Sum Tr (%) | 0.24 | 0.25 | 0.15 | 0.37 | 0.26 |
| Totals | | | | | |
| M + Tr oxides | 99.2 | 98.88 | 98.98 | 98.84 | 99.33 |
| With LOI | 99.83 | 99.64 | 99.50 | 99.28 | 99.33 |

*Note*: Dashes indicate values not determined. M—major elements; M + Tr—major and trace oxides; Tr—trace elements; LOI—loss on ignition. Sample AD-01a is referred to in some places in the text and figures as AD-01.
*Total Fe.

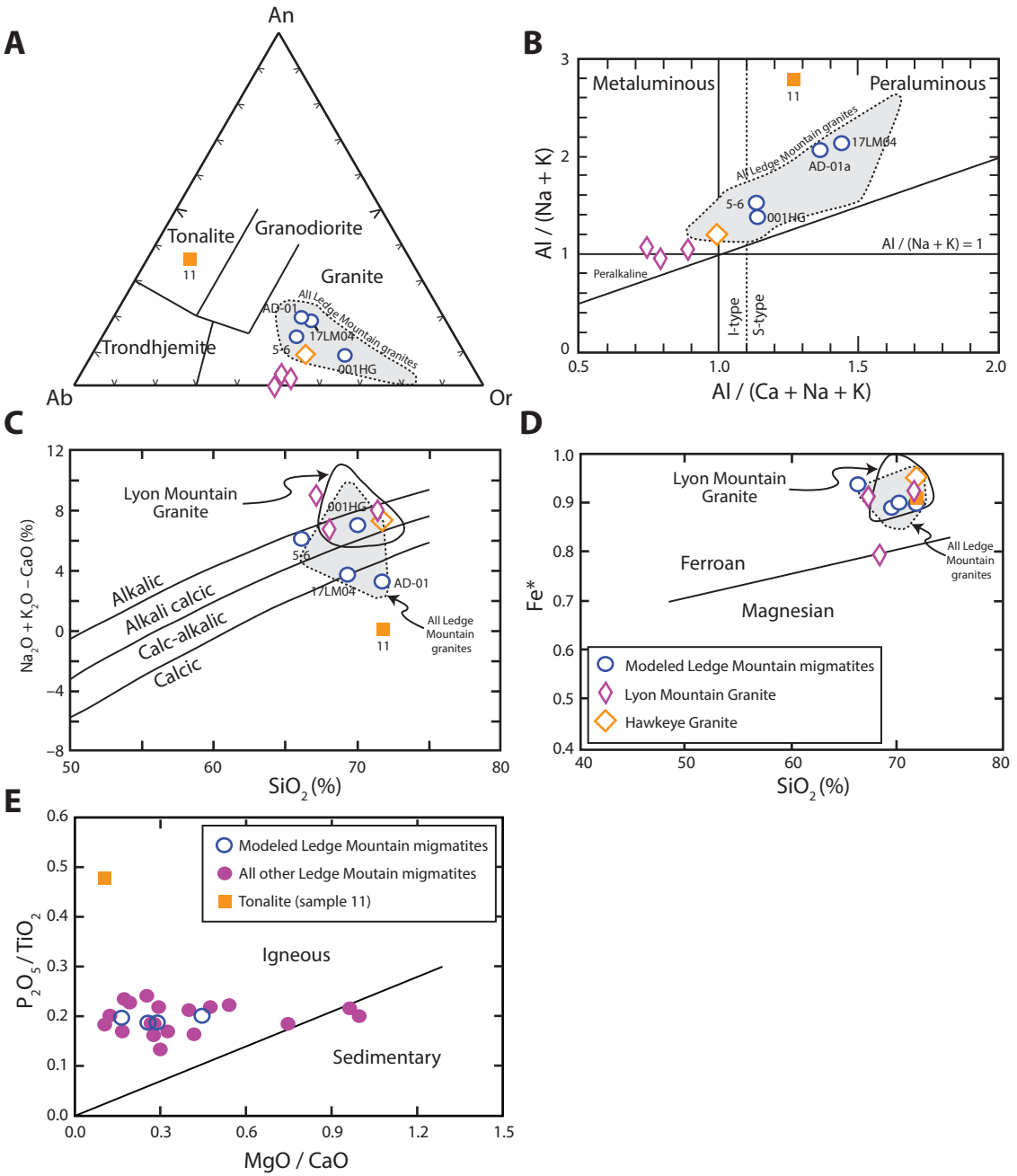


**Figure 9. Major element discrimination diagrams showing the modeled Ledge Mountain migmatites plotted with the Lyon Mountain and Hawkeye Granites. (A) Albite-anorthite-orthoclase (Ab-An-Or) discrimination plot (Barker, 1979) showing that the modeled Ledge Mountain samples, except for sample 11, and the Lyon Mountain and Hawkeye Granites plot in the granite field. (B) Alumina index diagram (Manier and Piccoli,1989) showing Ledge Mountain samples are peraluminous, Lyon Mountain Granite samples are metaluminous, and Hawkeye Granite falls in between. (C) Modified alkali lime index [($Na_2O$ + $K_2O$–CaO) vs. $SiO_2$]; Frost et al., 2001. Ledge Mountain samples plot in the alkali calcic to calcic fields, while Lyon Mountain Granite is alkalic or alkali calcic and Hawkeye Granite falls in the alkali calcic field. Broadly, Ledge Mountain samples are more calcic than the Lyon Mountain and Hawkeye Granites. (D) Fe* versus $SiO_2$ (Frost and Frost, 2008), showing Ledge Mountain, Lyon Mountain, and Hawkeye granites fall in the ferroan field. Fe* = Fe / (Fe + Mg). Lyon Mountain and Hawkeye data points are from Valley et al. (2011). Gray field shows span of Ledge Mountain samples with granitic compositions. Solid-line field in C and D represents the range of values for the Lyon Mountain Granite from Chiarenzelli et al. (2017). (E) $P_2O_5/TiO_2$ versus MgO/CaO diagram to distinguish felsic orthogneiss from paragneiss protoliths, showing all Ledge Mountain samples (after Werner, 1987, cited in Ownby et al., 2004).**

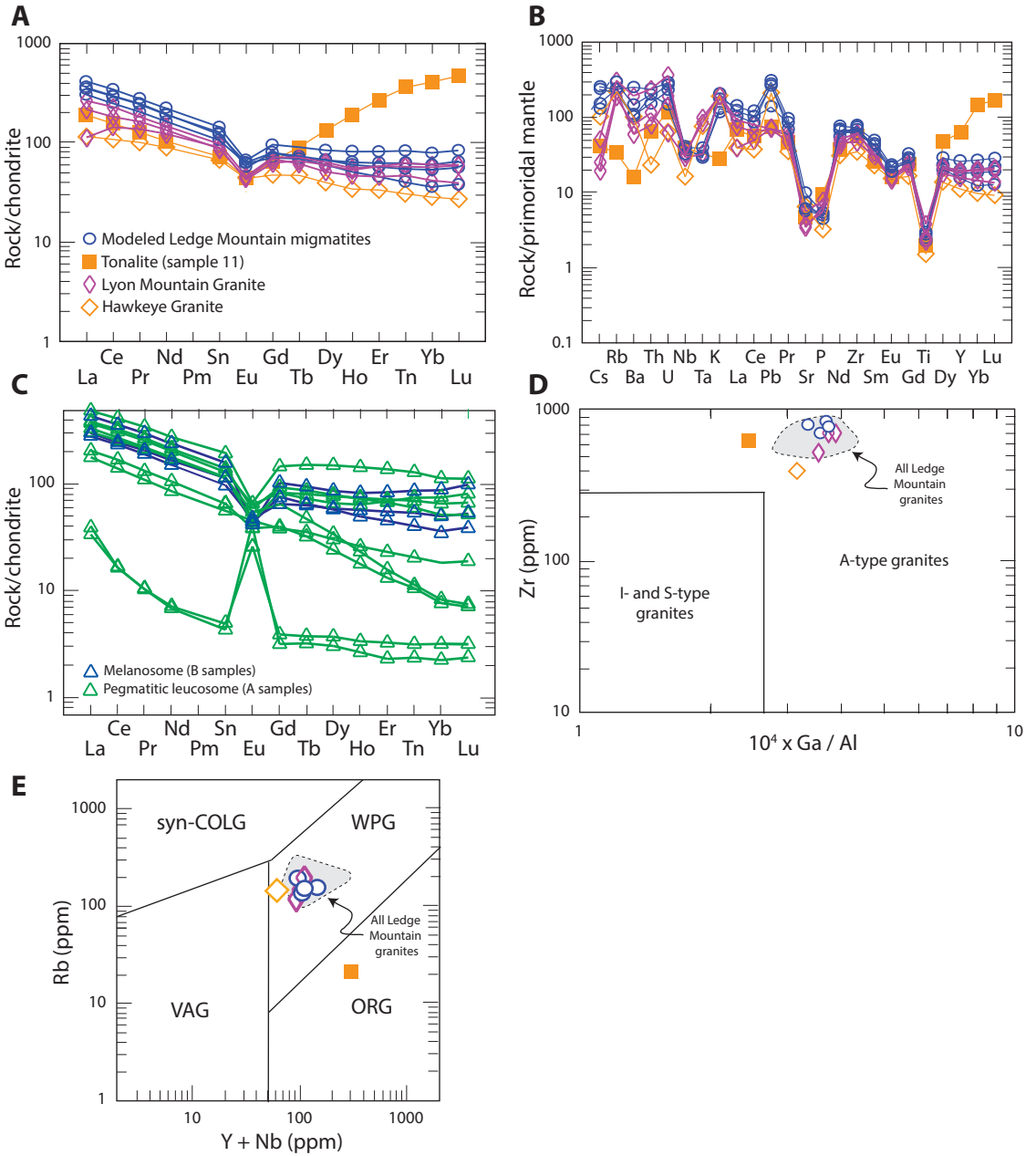


**Figure 10. Trace element discrimination diagrams showing the modeled Ledge Mountain migmatites plotted with the Lyon Mountain and Hawkeye Granites. (A) Chondrite-normalized spider diagram (Sun and McDonough, 1989). (B) Primordial mantle–normalized spider diagram (Sun and McDonough, 1989). (C) Chondrite-normalized spider diagram comparing Ledge Mountain pegmatitic leucosome to adjacent melanosome (Sun and McDonough, 1989). A—pegmatitic leucosome; B—melanosome. The magnitude of depletion in the heavy rare earth elements corresponds to the volume of garnet present in the source rock. Two pegmatitic leucosome samples show a large positive Eu anomaly. (D) Zr versus $10^4$ × Ga/Al plot (Whalen et al., 1987) showing the modeled Ledge Mountain samples and both the Lyon Mountain and Hawkeye Granites all plot in the A-type granite field. (E) Rb versus Y + Nb discrimination plot (Pearce et al., 1984) showing the modeled Ledge Mountain samples (except for sample 11) and both the Lyon Mountain and Hawkeye Granites all plot in the within-plate granite (WPG) field. Gray field shows span of Ledge Mountain metagranites. ORG—ocean ridge granites; syn-COLG—syn-collisional granites; VAG—volcanic arc granites.**

TABLE 7. ALL U-Th-Pb SHRIMP ANALYSES OF ZIRCON FROM LEDGE MOUNTAIN MIGMATITES

| Spot name | Zircon domain | I-M-C | U (ppm) | Th (ppm) | Th/U | $^{207}$Pb-corrected $^{206}$Pb (ppm) | $^{204}$Pb-corrected $^{238}$U/$^{206}$Pb | 1σ error (%) | $^{204}$Pb-corrected $^{207}$Pb/$^{206}$Pb | 1σ error (%) | $^{207}$Pb-corrected $^{206}$Pb/$^{238}$U age (Ma) | 1σ error (Ma) |
|---|---|---|---|---|---|---|---|---|---|---|---|---|
| 001HG-1.1 | Mantle + core | I | 171 | 57.6 | 0.35 | 27.0 | 5.38 | 2.7 | 0.0783 | 3.04 | 1097 | 29 |
| 001HG-4.1 | Rim | M | 1098 | 18.1 | 0.02 | 160.0 | 5.90 | 1.1 | 0.0737 | 0.71 | 1008 | 11 |
| 001HG-7.1 | Core | C | 2366 | 798.1 | 0.35 | 317.0 | 6.36 | 0.8 | 0.0761 | 0.48 | 935 | 7 |
| 001HG-20.1 | Rim | M | 967 | 18.7 | 0.02 | 317.0 | 5.91 | 2.5 | 0.0744 | 0.73 | 1006 | 24 |
| 001HG-29.1 | Rim | M | 652 | 19.9 | 0.03 | 98.0 | 5.71 | 0.7 | 0.0729 | 0.92 | 1042 | 7 |
| 001HG-30.1 | Rim | M | 639 | 16.2 | 0.03 | 94.0 | 5.86 | 0.7 | 0.0719 | 0.95 | 1017 | 7 |
| 001HG-33.1 | Rim | M | 928 | 18.8 | 0.02 | 142.0 | 5.61 | 1.1 | 0.0724 | 0.75 | 1060 | 11 |
| 004HG-10.1 | Rim | M | 731 | 8.1 | 0.01 | 109.3 | 5.75 | 1.1 | 0.0745 | 0.88 | 1034 | 11 |
| 004HG-13.1 | Rim | M | 721 | 7.5 | 0.01 | 105.6 | 5.86 | 1.1 | 0.0739 | 0.97 | 1015 | 11 |
| 004HG-16.1 | Core | I | 210 | 80.1 | 0.39 | 33.6 | 5.35 | 2.2 | 0.0790 | 1.98 | 1101 | 23 |
| 004HG-20.1 | Core | C | 1143 | 169.3 | 0.15 | 155.5 | 6.27 | 3.1 | 0.0763 | 0.69 | 948 | 28 |
| 004HG-24.1 | Rim | M | 846 | 8.7 | 0.01 | 130.9 | 5.55 | 0.8 | 0.0750 | 0.86 | 1067 | 8 |
| 004HG-27.1 | Rim | M | 728 | 11.8 | 0.02 | 109.2 | 5.73 | 1.7 | 0.0740 | 0.96 | 1038 | 17 |
| 005HG-A-5.1 | Rim | M | 1181 | 7.7 | 0.01 | 162.7 | 6.22 | 1.5 | 0.0726 | 0.73 | 959 | 14 |
| 005HG-A-6.1 | Rim | C | 868 | 16.0 | 0.02 | 120.9 | 6.15 | 0.6 | 0.0737 | 0.83 | 969 | 6 |
| 005HG-A-9.1 | Mantle | I | 89 | 30.6 | 0.35 | 15.0 | 5.07 | 1.2 | 0.0854 | 2.81 | 1152 | 13 |
| 005HG-A-10.1 | Rim | C | 731 | 14.6 | 0.02 | 101.7 | 6.15 | 1.4 | 0.0745 | 0.99 | 969 | 13 |
| 005HG-A-17.1 | Mantle | I | 58 | 17.2 | 0.31 | 9.8 | 5.08 | 3.5 | 0.0780 | 4.95 | 1159 | 39 |
| 005HG-A-24.1 | Rim | M | 959 | 15.8 | 0.02 | 151.0 | 5.46 | 1.2 | 0.0743 | 0.81 | 1085 | 13 |
| 005HG-B-2.1 | Rim | M | 650 | 17.2 | 0.03 | 87.3 | 6.37 | 2.4 | 0.0746 | 1.17 | 936 | 22 |
| 005HG-B-3.1 | Rim | M | 701 | 23.0 | 0.03 | 102.6 | 5.86 | 1.2 | 0.0748 | 1.04 | 1014 | 11 |
| 005HG-B-9.1 | Rim | M | 608 | 19.0 | 0.03 | 92.9 | 5.62 | 1.8 | 0.0749 | 1.03 | 1055 | 18 |
| 005HG-B-15.1 | Rim | C | 715 | 12.1 | 0.02 | 106.0 | 5.79 | 1.8 | 0.0747 | 1.02 | 1026 | 18 |
| 005HG-B-26.1 | Core | I | 1504 | 418.3 | 0.29 | 250.7 | 5.13 | 0.6 | 0.0815 | 4.50 | 1144 | 8 |
| 005HG-B-34.1 | Rim | M | 703 | 24.2 | 0.04 | 106.7 | 5.66 | 2.6 | 0.0751 | 0.93 | 1049 | 26 |
| 005HG-B-37.1 | Mantle | I | 106 | 42.8 | 0.42 | 17.1 | 5.31 | 1.2 | 0.0801 | 3.03 | 1107 | 12 |
| 006HG-A-34.1 | Rim | M | 774 | 14.6 | 0.02 | 112.6 | 5.89 | 0.9 | 0.0740 | 0.94 | 1009 | 9 |
| 006HG-A-34.2 | Mantle or core | I | 291 | 99.3 | 0.35 | 47.6 | 5.24 | 1.3 | 0.0796 | 2.52 | 1123 | 14 |
| 006HG-A-36.1 | Rim | M | 603 | 12.8 | 0.02 | 85.0 | 6.08 | 1.9 | 0.0738 | 1.07 | 979 | 18 |
| 006HG-A-36.2 | Mantle | I | 86 | 33.9 | 0.41 | 13.5 | 5.47 | 2.0 | 0.0776 | 4.38 | 1079 | 21 |
| 006HG-B-8.1 | Core | I | 1201 | 621.7 | 0.53 | 210.1 | 4.92 | 1.8 | 0.0784 | 0.64 | 1195 | 21 |
| 006HG-B-30.1 | Mantle | I | 71 | 21.1 | 0.31 | 12.1 | 4.99 | 1.3 | 0.0810 | 4.04 | 1176 | 15 |
| 006HG-B-31.1 | Rim | M | 570 | 17.1 | 0.03 | 85.2 | 5.75 | 2.3 | 0.0740 | 1.00 | 1033 | 23 |
| 006HG-B-33.1 | Rim | M | 763 | 13.1 | 0.02 | 114.5 | 5.72 | 1.5 | 0.0743 | 0.89 | 1038 | 15 |
| 007HG-A-1.1 | Rim | C | 823 | 22.8 | 0.03 | 125.5 | 5.64 | 0.6 | 0.0734 | 0.96 | 1054 | 6 |
| 007HG-A-3.1 | Rim | C | 675 | 9.2 | 0.01 | 100.1 | 5.81 | 0.7 | 0.0718 | 1.09 | 1026 | 7 |
| 007HG-A-8.1 | Rim | M | 614 | 17.1 | 0.03 | 88.1 | 5.98 | 0.7 | 0.0739 | 1.03 | 996 | 6 |
| 007HG-A-14.1 | Rim | C | 731 | 17.2 | 0.02 | 106.7 | 5.88 | 0.7 | 0.0735 | 1.73 | 1012 | 7 |
| 007HG-A-19.1 | Rim | C | 928 | 19.5 | 0.02 | 135.5 | 5.89 | 1.1 | 0.0719 | 0.82 | 1012 | 11 |
| 007HG-A-24.1 | Rim | M | 680 | 16.6 | 0.03 | 99.8 | 5.86 | 1.0 | 0.0722 | 1.04 | 1017 | 10 |
| 007HG-A-29.1 | Rim | C | 722 | 21.0 | 0.03 | 108.6 | 5.72 | 1.5 | 0.0735 | 0.96 | 1040 | 15 |
| 007HG-A-35.1 | Mantle | C | 131 | 39.5 | 0.31 | 16.9 | 6.61 | 1.1 | 0.0775 | 3.16 | 900 | 10 |
| 007HG-A-35.2 | Mantle | I | 125 | 35.3 | 0.29 | 19.4 | 5.53 | 1.9 | 0.0762 | 2.65 | 1070 | 20 |
| 007HG-B-1.1 | Rim | M | 680 | 11.2 | 0.02 | 95.1 | 6.13 | 1.0 | 0.0739 | 1.01 | 972 | 10 |
| 007HG-B-1.2 | Rim | C | 806 | 17.2 | 0.02 | 119.6 | 5.78 | 3.7 | 0.0747 | 0.87 | 1027 | 36 |
| 007HG-B-3.1 | Rim | C | 649 | 19.2 | 0.03 | 97.8 | 5.71 | 0.7 | 0.0719 | 1.07 | 1043 | 7 |
| 007HG-B-13.1 | Rim | M | 661 | 16.7 | 0.03 | 97.7 | 5.81 | 0.7 | 0.0738 | 0.99 | 1023 | 7 |
| 007HG-B-18.1 | Rim | M | 1044 | 21.8 | 0.02 | 157.8 | 5.69 | 0.6 | 0.0733 | 0.82 | 1045 | 6 |
| 007HG-B-19.1 | Rim | C | 909 | 23.4 | 0.03 | 136.9 | 5.72 | 3.2 | 0.0714 | 0.99 | 1041 | 32 |

(*continued*)

TABLE 7. ALL U-Th-Pb SHRIMP ANALYSES OF ZIRCON FROM LEDGE MOUNTAIN MIGMATITES (*continued*)

| Spot name | Zircon domain | I-M-C | U (ppm) | Th (ppm) | Th/U | $^{207}$Pb-corrected $^{206}$Pb (ppm) | $^{204}$Pb-corrected $^{238}$U/$^{206}$Pb | 1σ error (%) | $^{204}$Pb-corrected $^{207}$Pb/$^{206}$Pb | 1σ error (%) | $^{207}$Pb-corrected $^{206}$Pb/$^{238}$U age (Ma) | 1σ error (Ma) |
|---|---|---|---|---|---|---|---|---|---|---|---|---|
| 007HG-B-23.1 | Rim | M | 1695 | 18.5 | 0.01 | 261.3 | 5.58 | 0.9 | 0.0738 | 1.00 | 1064 | 9 |
| 007HG-B-24.1 | Mantle | C | 311 | 33.7 | 0.11 | 47.3 | 5.66 | 0.8 | 0.0720 | 2.38 | 1052 | 8 |
| 007HG-B-24.2 | Core | C | 1153 | 5.4 | 0.00 | 171.1 | 5.78 | 1.8 | 0.0746 | 0.67 | 1027 | 18 |
| 007HG-B-26.1 | Rim | M | 692 | 19.9 | 0.03 | 102.3 | 5.80 | 1.2 | 0.0749 | 0.98 | 1023 | 12 |
| 007HG-B-28.1 | Rim | M | 1117 | 26.1 | 0.02 | 150.6 | 6.33 | 1.8 | 0.0751 | 0.93 | 940 | 16 |
| 007HG-B-38.1 | Rim | M | 489 | 11.5 | 0.02 | 73.8 | 5.80 | 0.8 | 0.0577 | 5.81 | 1044 | 8 |
| 008HG-A-2.1 | Mantle | I | 131 | 58.2 | 0.46 | 20.9 | 5.37 | 2.3 | 0.0782 | 2.73 | 1099 | 25 |
| 008HG-A-3.1 | Mantle or rim | M | 966 | 30.3 | 0.03 | 141.1 | 5.88 | 1.2 | 0.0734 | 0.79 | 1012 | 11 |
| 008HG-A-5.1 | Rim | C | 1017 | 36.2 | 0.04 | 147.1 | 5.95 | 1.2 | 0.0712 | 0.86 | 1003 | 12 |
| 008HG-A-10.1 | Rim | M | 1206 | 12.0 | 0.01 | 173.0 | 5.99 | 2.0 | 0.0713 | 0.72 | 996 | 19 |
| 008HG-A-11.1 | Core | I | 1652 | 859.6 | 0.54 | 280.8 | 5.06 | 1.9 | 0.0784 | 0.53 | 1164 | 21 |
| 008HG-A-23.1 | Rim | I | 901 | 23.9 | 0.03 | 132.3 | 5.85 | 2.0 | 0.0727 | 0.80 | 1017 | 19 |
| 008HG-A-25.1 | Mantle or rim | C | 637 | 37.6 | 0.06 | 93.7 | 5.84 | 1.3 | 0.0724 | 1.15 | 1019 | 12 |
| 008HG-B-1.1 | Core | I | 5769 | 1554.7 | 0.28 | 657.2 | 7.49 | 1.8 | 0.0719 | 0.68 | 803 | 14 |
| 008HG-B-2.1 | Mantle or rim | C | 1532 | 22.9 | 0.02 | 223.2 | 5.90 | 0.9 | 0.0724 | 0.66 | 1010 | 9 |
| 008HG-B-9.1 | Rim | C | 953 | 27.0 | 0.03 | 145.0 | 5.66 | 2.5 | 0.0727 | 0.83 | 1052 | 26 |
| 008HG-B-24.1 | Core | I | 2629 | 1014.0 | 0.40 | 241.3 | 9.27 | 0.5 | 0.0696 | 1.22 | 654 | 3 |
| 008HG-B-25.1 | Rim | M | 752 | 27.0 | 0.04 | 110.2 | 5.86 | 1.0 | 0.0737 | 0.95 | 1016 | 10 |
| 008HG-B-32.1 | Rim | M | 1561 | 33.1 | 0.02 | 236.9 | 5.66 | 1.7 | 0.0741 | 0.63 | 1049 | 17 |
| 008HG-B-36.1 | Mantle + rim | M | 971 | 48.5 | 0.05 | 114.9 | 7.21 | 2.9 | 0.0722 | 1.08 | 832 | 23 |
| 008HG-B-39.1 | Rim | M | 825 | 21.4 | 0.03 | 117.9 | 6.02 | 2.5 | 0.0723 | 0.92 | 991 | 24 |

*Note*: SHRIMP—sensitive high-resolution ion microprobe. Zircon characterization (see text): I—igneous (i.e., magmatic domains); M—metamorphic; C—complex. All of these analyses are represented in the concordia diagrams (Fig. 12), cathodoluminescence imaging (Fig. S1 [see text footnote 1]), and rare earth element plots (Fig. S2). Samples 001HG and 004HG are melanosome + interlayered leucosome. Samples 005HG, 006HG, 007HG, and 008HG are paired pegmatitic leucosome and melanosome samples: A denotes leucosome; B denotes melanosome. Corresponding sample numbers in Fig. 11 drop "HG" for labeling simplicity.

## U-Pb SHRIMP-RG ZIRCON GEOCHRONOLOGY AND TRACE ELEMENT CHEMISTRY

### Zircon Results

Uranium-lead (U-Pb) geochronology and trace element analyses of zircon were conducted at the Stanford–U.S. Geological Survey (USGS) SHRIMP-RG Lab ("RG" is reverse geometry); a detailed description of methods is included in Supplemental Text S1[1], and data are presented in Table 7, Figures 11 and 12, and Figures S1–S3 (footnote 1).

Zircons from 10 migmatite samples were analyzed for trace element geochemistry and U-Pb geochronology at the Stanford-USGS SHRIMP-RG Lab (Reeder, 2017; Figs. 11, 12; Table 7). We analyzed zircon from six samples of Ledge Mountain melanosome (001HG, 004HG, 005HG-B, 006HG-B, 007HG-B, and 008HG-B) and four samples of pegmatitic leucosome (005HG-A, 006HG-A, 007HG-A, and 008HG-A); 001HG and 004HG are melanosome with microscopically interlayered leucosome, and the four melanosome samples denoted with "B" were collected adjacent to the four paired leucosome samples denoted with "A" (Reeder, 2017; Figs. 11, 12; Table 7). Zircon growth domains are divided into core, mantle, and rim domains and described based on the type (or lack) of zoning, cathodoluminescence (CL) character (i.e., brightness), and the grain or zircon domain morphology (Figs. 11, 12; Figs. S1–S3 [footnote 1]). We focused on the most recent (i.e., outer) zircon growth domains in order to capture the metamorphic and anatectic history of Ledge Mountain rocks.

### *Zircon Descriptions*

***Zircons from melanosome with interlayered leucosome (samples 001HG, 004HG).*** Dated zircons from melanosome with interlayered leucosome (samples 001HG and 004HG; $n = 13$) include dark inherited cores, and mantles with medium-bright CL; are unzoned or have a complex zoning

[1]Supplemental Material. Text S1: Supplemental text. Figure S1: Cathodoluminescence images for all analyzed zircon grains. Figure S2: REE spider plots for zircon. Figure S3: Tukey honestly significant difference (HSD) for the timing of anatexis. Table S1: Whole-rock data for 11 samples used in the average isochemical phase equilibria model in Figure 15. Table S2. Grossular content of garnet used to calculate the 95% confidence intervals for isopleth modeling in Figure 13. Please visit https://doi.org/10.1130/GEOS.S.16766470 to access the supplemental material, and contact editing@geosociety.org with any questions.

pattern; and occur in domains that are subhedral to rounded with margins that show evidence of dissolution (e.g., embayments; Fig. 11; Fig. S1 [footnote 1]). Core domain 004HG-16.1 yielded a near-concordant date of 1101 ± 23 Ma (Fig. 11). Grains with spots 001HG-29.1, 001HG-33.1, and 004HG-13.1 are three exceptions because they lack similar inherited cores (Table 7; Fig. 11; Fig. S1); the cores of these three zircon grains are medium bright to bright in CL and have faded or disrupted oscillatory zoning or a complex pattern, and the core domains are subhedral to anhedral. One zircon (spot 001HG-1.1) contains a mantle that is medium bright in CL, euhedral, displays faded or disrupted oscillatory zoning, has embayments suggesting dissolution, and gave one concordant analysis at 1097 ± 29 Ma. Rims are dark in CL; form thin, outer domains in rounded grains; and are mostly unzoned but locally display faded oscillatory zoning (e.g., spot 004-13.1). Dates for concordant or near-concordant zircon rims from samples of melanosome with interlayed leucosome range from 1067 ± 8 to 1006 ± 24 Ma (Table 7; Fig. 12). Zircons gave Th/U ratios of 0.15–0.39 for cores, 0.35 for one mantle, and 0.01–0.03 for rims.

***Zircons from pegmatitic leucosome bodies (samples 005HG-A, 006HG-A, 007HG-A, 008HG-A).*** Zircons from pegmatic leucosomes have mantles that display medium-bright CL (frequently with a dark inner core; e.g., spot 008HG-A-11.1 = 1164 ± 21 Ma); have oscillatory zoning that is sometimes faded or disrupted, complex zoning, or (uncommonly) sector zoning (e.g., spot 006HGA-34.2 = 1123 ± 14 Ma); and form euhedral to subhedral or rounded domains, with some exhibiting significant dissolution along the domain boundary. Dates for concordant or near-concordant zircon mantles from leucosomes range from 1152 ± 13 to 1070 ± 20 Ma ($n$ = 5). Zircon rims are thin and dark in CL; form rounded to subhedral domains; and are unzoned, show complex zoning, or faded or disrupted oscillatory zoning (Table 7; Fig. 11; Fig. S1 [footnote 1]). Dates for zircon rims from leucosome range from 1085 ± 13 to 959 ± 14 Ma (Fig. 12; Fig. S1). Th/U ratios ranged from 0.35 to 0.54 for cores, 0.29 to 0.46 for mantles, and 0.1 to 0.6 for rims.

***Zircons from melanosome adjacent to paired pegmatitic leucosome (samples 005HG-B, 006HG-B, 007HG-B, 008HG-B).*** Melanosome surrounding leucosome contains zircons with cores that are bright to dark in CL (commonly with a dark inner core; e.g., spot 006HG-B-8.1), form subhedral to rounded domains, show complex and oscillatory zoning or (uncommonly) sector zoning (e.g., spot 005HG-B-37.1), and contain embayments that are evidence of dissolution along margins of the zircon core (Table 7; Fig. 11; Fig. S1 [footnote 1]). Concordant zircon core ages range from 1195 ± 21 to 1107 ± 12 Ma ($n$ = 3) with one analysis at 1027 ± 18 Ma. One zircon mantle is medium bright in CL, has disrupted oscillatory zoning in a subhedral domain, and gave a date of 1052 ± 8 Ma (spot 007HG-B-24.1). Zircon rims are dark in CL, form subhedral to rounded domains, and are complexly zoned with faded or disturbed oscillatory zoning. Zircon rims from melanosome adjacent to leucosome yielded dates from 1064 ± 9 to 972 ± 10 Ma. Th/U ratios ranged from 0.29 to 0.53 for cores, 0.11 to 0.42 for mantles, and 0.02 to 0.04 for rims.

### *Rare Earth Elements*

Zircons from all analyzed samples show steep REE patterns characterized by HREE enrichment, negative Eu anomalies, and positive Ce anomalies (Fig. 12; Fig. S2 [footnote 1]).

## Zircon Interpretation

### *Textural Classification of Zircon*

We catalog zircon textures and classify zircon domains as having a "magmatic", "metamorphic", or "complex" character based on the type (or lack) of zoning that we see in the zircons, the cathodoluminescence (CL) character, and zircon domain morphology. Zircon domains classified as magmatic have well-developed growth zoning described as oscillatory and/or sector zoning interpreted to result from trace element variations as zircon crystallizes from a magma, and most form subhedral to euhedral crystals or domains with aspect ratios of ~1:2–1:4 (Corfu et al., 2003; Hoskin and Schaltegger, 2003).

Textures of metamorphic zircon can vary because of the different conditions of their formation, such as whether metamorphic zircon crystallized in the solid state by, for example, recrystallizing inherited zircon, or whether it grew from a fluid (e.g., anatectic melt) on cooling (Corfu et al., 2003; Hoskin and Schaltegger, 2003). In Ledge Mountain rocks, zircon domains classified as metamorphic typically have rounded or ovoid forms and have minimal CL (i.e., dark growth domains).

Inherited (i.e., xenocrystic) zircon cores can be distinguished by the presence of truncated growth zoning or an otherwise distinct boundary separating an unzoned or chaotically zoned core from a rim of a different character (Corfu et al., 2003; Hoskin and Schaltegger, 2003). Any of these zircon domains may have been subject to later resorption or recrystallization depending on the geologic history of the rocks. Zircons classified as complex are described below.

***Evidence of disruption of primary magmatic features in zircon.*** Zircon domains are commonly embayed, suggesting later dissolution (see 007HG-A and 008HG-A in Fig. 11). The transition zones between interior and rim domains exhibit textural features consistent with solid-state recrystallization and a transgressive recrystallization front, or evidence of magmatic resorption along irregular domain interfaces (samples 004HG-A and 006HG-A in Fig. 11; Corfu et al., 2003; Hoskin and Schaltegger, 2003). Disruption of concentric oscillatory zoning, a primary magmatic feature, appears as thickened, convoluted, blurred, or faded zoning, preserving "ghosts" of relict oscillatory zoning, and indicating solid-state recrystallization during metamorphism (sample 008HG-A in Fig. 11; Corfu et al., 2003; Hoskin and Schaltegger, 2003); these commonly correspond to the "complex" domains defined in this study.

The "fir tree" CL patterns in zircon and "soccer ball" grain shapes described by Bickford et al. (2008) for migmatitic metapelites in the eastern Adirondack Highlands are absent in Ledge Mountain zircons. Corfu et al. (2003) reviewed textural evidence for hydrothermal growth of zircon focusing on high-U alteration textures ("overgrowths") on low-U zircon

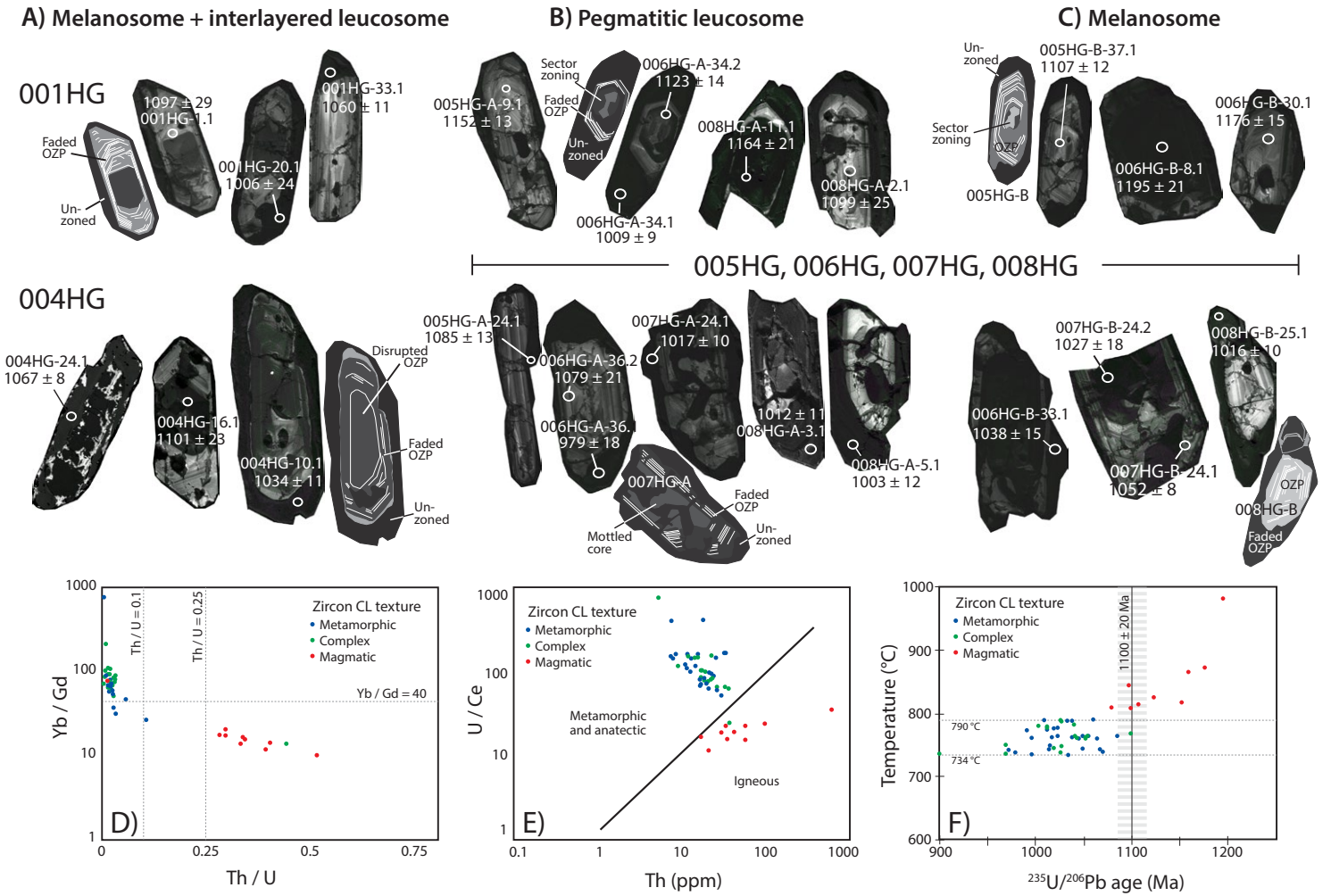


**Figure 11. Representative cathodoluminescence (CL) imaging of zircons dated by U-Th-Pb sensitive high-resolution ion microprobe (SHRIMP) geochronology for samples of melanosome with microscopically interlayered leucosome; pegmatitic leucosome; and melanosome adjacent to pegmatitic leucosome. Schematic diagrams of zircon are included to highlight textural differences between growth domains. Sample numbers and spot names corresponding to Table 7 are shown with ages ± 1σ errors (in Ma). Samples 005HG, 006HG, 007HG, and 008HG are paired pegmatitic leucosome and melanosome; spot name suffixes "-A" and "-B" indicate pegmatitic leucosome and melanosome, respectively. OZP—oscillatory zoning pattern. (A) Zircons from migmatite samples 001HG and 004HG (melanosome with interlayered leucosome). (B) Zircons from pegmatitic leucosome. (C) Zircons from melanosome. (D) Plot of Yb/Gd versus Th/U ratios from zircons. Th/U ratios <0.1 represent metamorphic settings; higher Th/U ratios indicate magmatic growth. Garnet preferentially incorporates heavy rare earth elements, so Yb/Gd ratios >40 result from growth without garnet; most Ottawan-aged zircons have Yb/Gd >40 and so likely grew post–peak metamorphism. (E) Plot of U/Ce ratios versus Th concentrations for metamorphic (blue), complex (green), and magmatic (red) zircon analyses. High U/Ce values indicate zircon growth in a metamorphic or anatectic setting, while low U/Ce values indicate magmatic zircon growth. (F) Ti-in-zircon temperatures versus age for different zircon domains. Metamorphic and anatectic zircons fall between 734 and 790 °C. Trace element data and zircon textures suggest "magmatic" zircon domains >1100 Ma are magmatic in origin, while the Ottawan-age domains have characteristics of metamorphic and/or anatectic zircon growth. See Figure S1 (see text footnote 1) for all CL imaging and Figure S2 for complete rare earth element plots.**

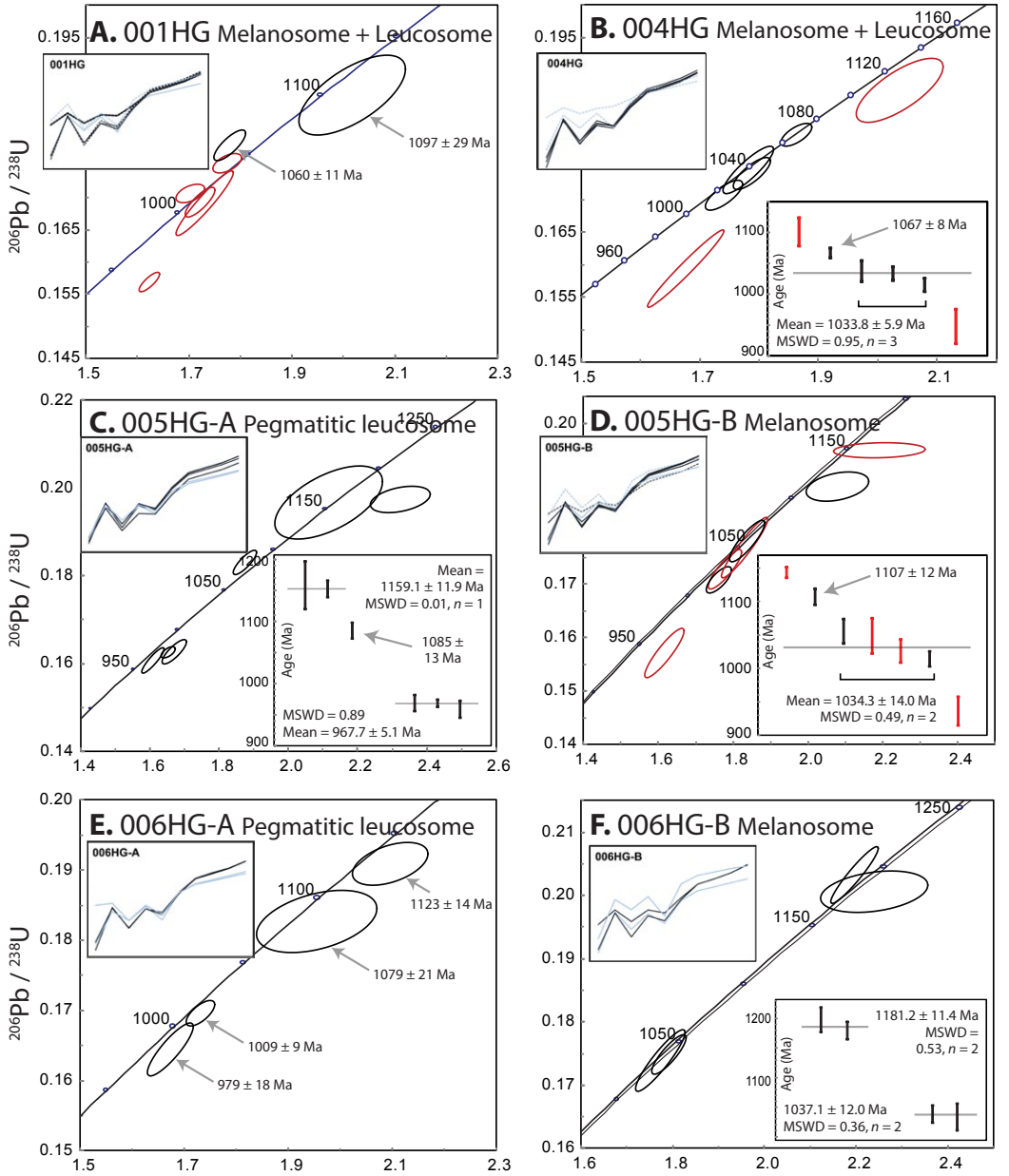


**Figure 12. Concordia diagrams for all U-Pb sensitive high-resolution ion microprobe (SHRIMP) analysis of zircons from Ledge Mountain corresponding to the data in Table 7. Inset plots of chondrite-normalized rare earth element (REE) data are included to aid in interpretation of age data. Normalization values are from McDonough and Sun (1995). (A) Sample 001HG gave one concordant (1097 ± 29 Ma) and one near-concordant analysis (1060 ± 11 Ma). (B) Sample 004HG yielded one concordant analysis at 1067 ± 8 Ma and three concordant points with a weighted mean of 1034 ± 6 Ma. (C) Sample 005HG-A zircons gave two concordant analyses with a weighted mean of 1159 ± 12 Ma, and one analysis at 1085 ± 13 Ma. The three youngest zircon rim ages for a pegmatitic leucosome come from 005HG-A with a mean of 968 ± 5 Ma (mean squared weighted deviation [MSWD] = 0.89). (D) Sample 005HG-B zircons from melanosome adjacent to pegmatitic leucosome yielded two concordant dates with a weighted mean of 1034 ± 14 Ma and one analysis at 1107 ± 12 Ma. (E) Sample 006HG-A gave four (near-)concordant dates at 1123 ± 14, 1079 ± 21, 1009 ± 9, and 979 ± 18 Ma. (F) Sample 006HG-B zircons gave four concordant dates, two with a weighted mean of 1181 ± 11 Ma and two with a weighted mean of 1037 ± 12 Ma. (*Continued on following page.*)**

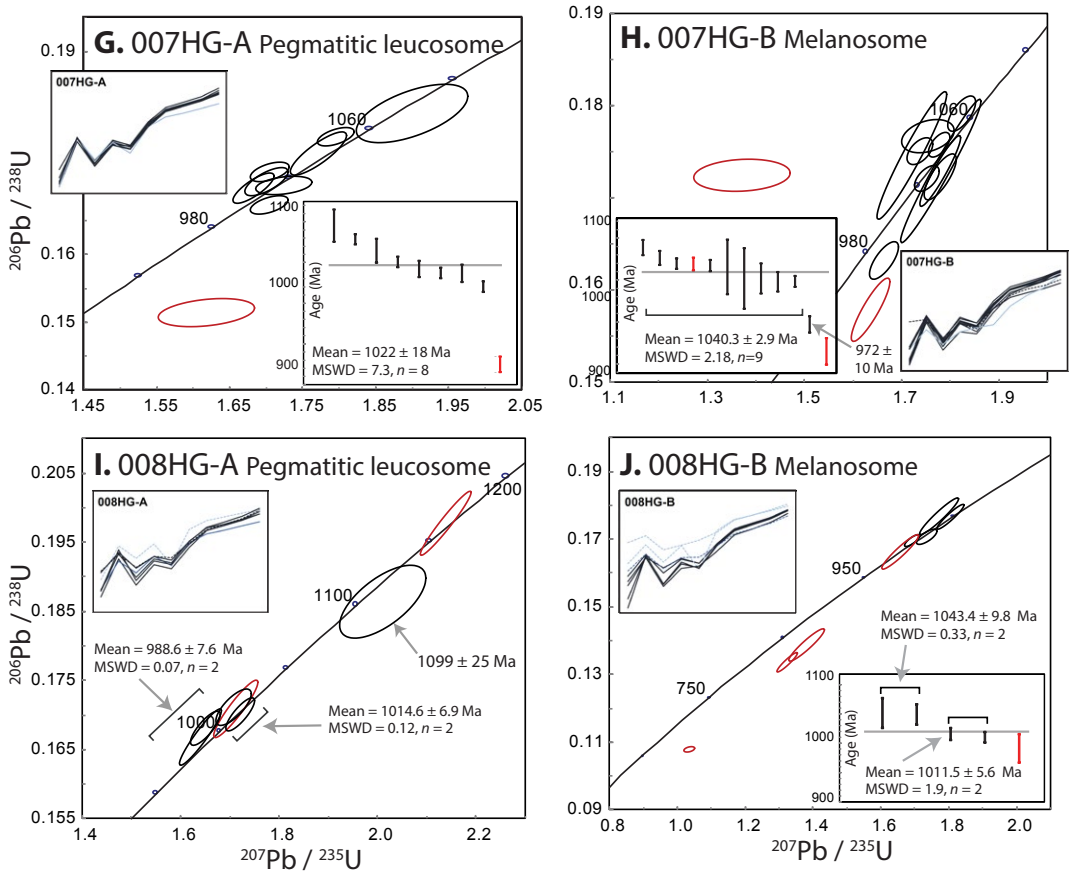


**Figure 12 (*continued*). (G) Sample 007HG-A yielded eight (near-)concordant dates with a weighted mean of 1022 ± 18 Ma. (H) Sample 007HG-B gave nine (near-)concordant dates with a weighted mean of 1040 ± 3 Ma and one analysis at 972 ± 10 Ma. (I) Sample 008HG-A gave one concordant date at 1099 ± 25 Ma, two dates with a weighted mean of 1015 ± 7 Ma, and another two with a weighted mean of 989 ± 8 Ma. (J) Sample 008HG-B yielded two concordant dates with a weighted mean of 1043 ± 10 Ma, and two with a weighted mean at 1012 ± 6 Ma. Note analyses in red were not included in the mean age calculation because they are not concordant (or not near-concordant) or because they have high Fe or Ti concentrations or high common Pb, for example; these are the same analyses comprising the dashed REE profiles (see Fig. S2 [see text footnote 1] for REE details).**

that are usually found as high-U embayments into zircon cores; they suggest these high-U overgrowths formed from aqueous fluids by recrystallization, metasomatism, or dissolution and reprecipitation and at low pressures and low temperatures (<500 °C, <2 kbar). Evidence for hydrothermally precipitated zircon is absent in Ledge Mountain zircons (see Text S1 [footnote 1] for further discussion).

We assigned zircon to our three groups—magmatic, metamorphic, or complex—to look for patterns that might help us to explain the zircon crystallization history. We analyzed the zircon chemistry including the Th/U ratio, assessment of the REE patterns, and Ti-in-zircon temperatures after looking at zircon dates for each of the zircon domains. The Ti-in-zircon temperature versus age plot in Figure 11F shows that the magmatic domains correspond to inherited cores from >1100 Ma to the earliest Ottawan; zircon age domains younger than ca. 1100 Ma are categorized as metamorphic or anatectic, suggesting the Ottawan was a time of high-grade metamorphism and anatectic melting.

### *Age Distributions*

The oldest concordant dates from zircon cores span the Shawinigan orogeny (Fig. 12; McLelland et al., 2004; Rivers, 2008, 2015) to nearly the Ottawan orogeny (Rivers, 2008, 2015; Chiarenzelli et al., 2010): concordant core dates range from 1195 ± 21 Ma (spot 006HG-B-8.1) to 1107 ± 12 Ma (spot 005HG-B-37.1) with a weighted mean of 1161.4 ± 7.5 Ma (mean squared weighted deviation [MSWD] = 2.5, $n$ = 9). There was one outlier date from a zircon core at 1027 ± 36 Ma (spot 007HG-B-1.2) that probably does not represent inheritance like the core domains of most grains.

Most of the concordant zircon dates we collected come from rim domains ($n$ = 33) and range from 1085 ± 13 to 959 ± 14 Ma (Table 7; Figs. 11, 12; Fig. S1 [footnote 1]). Dividing these rim dates

into those from melanosome with interlayered leucosome (samples 001HG and 004HG), melanosome adjacent to pegmatitic leucosome (samples 005HG-B to 008HG-B), and pegmatitic leucosome adjacent to melanosome (samples 005HG-A to 008HG-A), we see differences that help identify different stages in the metamorphic and anatectic history of Ledge Mountain rocks. Dates for zircon rims from melanosome with interlayered leucosome range from 1067 ± 8 to 1015 ± 11 Ma with a weighted mean of 1047.0 ± 4.6 Ma (MSWD = 4.53, $n$ = 5). Zircon rim dates for melanosome adjacent to pegmatitic leucosome range from 1064 ± 9 to 1010 ± 9 Ma with a weighted mean of 1035.2 ± 2.4 Ma (MSWD = 2.5, $n$ = 17); one outlier was excluded from this age (spot 007HG-B-1.1, 972 ± 10 Ma).

Most pegmatitic leucosomes are largely undeformed and not recrystallized, suggesting that the anatexis that formed the pegmatitic leucosomes represents the most recent metamorphic or melting event at Ledge Mountain. The timing of this anatexis is closely associated with granulite-facies metamorphism that preceded and/or accompanied it; this history is recorded by the trace element and age analyses in the outermost zircon domains (Figs. 11D–11F; Figs. S1–S3 [footnote 1]).

Zircon rims from pegmatitic leucosome give the youngest dates, ranging from 1019 ± 12 to 959 ± 14 Ma with a weighted mean of 992.8 ± 3.3 Ma (MSWD = 4.29, $n$ = 9); one outlier was excluded from this mean age (spot 005HG-A-24.1, 1085 ± 13 Ma). The five oldest zircon rims from pegmatitic leucosome form an age group at 1009 ± 14 Ma (MSWD = 0.44), and the three youngest ages from zircon rims from pegmatitic leucosome come from a single sample (005HG-A), giving a mean date of 967.7 ± 5.1 Ma (Fig. 12C; Fig. S1 [footnote 1]). Complexly zoned zircon domains record recrystallization of zircon rims formed following UHT conditions during near-isothermal decompression and cooling to high-temperature (HT) granulite-facies conditions; zircon rims from pegmatitic leucosome may have formed during cooling and crystallization from anatectic melt on the retrograde *P-T* path because models show that melt persisted in Ledge Mountain migmatites during exhumation to the mid-crust where retrograde metamorphism took place at HT granulite-facies conditions.

There is no statistical difference in U-Pb dates for the two characteristic zircon rim textures we document—i.e., for (1) thin, unzoned, low-CL-intensity rims forming rounded grains; and (2) rims with weak, fine oscillatory zoning with low CL contrast (Table 7; Fig. 11; Figs. S1–S3 [footnote 1]). Both zircon rim textures have similar Th/U ratios, U contents, and REE patterns, which suggests that the anatectic melts were in sufficient volume to form an interconnected melt network in the migmatites (Schaltegger et al., 1999). We interpret these zircon rim textures to represent metamorphism in the presence of an anatectic melt phase (Rubatto and Gebauer, 2000).

### *Trace Element Analysis of Zircons*

Thorium/uranium (Th/U) ratios for the metamorphic and complex domains are <0.1, while magmatic domains have Th/U values >0.25 (Fig. 11D; Table 7). The U/Ce versus Th plot in Figure 11E shows that the metamorphic and complex zircon domains fall in the metamorphic or anatectic field; magmatic domains fall within the igneous field (Hoskin and Schaltegger, 2003). Trace element data for the oldest zircon domains (inherited cores >1100 Ma) and Ti-in-zircon temperature estimates show that magmatic zircon domains plot together as a discrete group (Figs. 11D–11F). Dates younger than ca. 1100 Ma plot in the metamorphic or anatectic zircon fields, corresponding to Th/U <0.1 (with all but one analysis <0.07) and lower Ti-in-zircon temperatures compared to magmatic domains that are >1100 Ma and have Th/U >0.25, indicating the Ottawan was a time of high-grade metamorphism and anatectic melting (Figs. 11D, 11F). Zircon textures suggest that some new zircon grew by recrystallization of inherited zircon and/or the older igneous zircon, and zircon could have grown from anatectic melt.

Melting has a strong effect on the dissolution and crystallization behavior of zircon, especially in felsic rocks; instead of recording peak *P-T* conditions of metamorphism, zircons crystallize during post-peak exhumation and cooling (Roberts and Finger, 1997; Kelsey et al., 2008; Kohn et al., 2015). Zirconium is stored in the melt phase and in inherited zircons in migmatitic granulites (Rubatto, 2017). Models of Zr solubility in migmatites show that new zircon crystallizes when Zr solubility in the melt drops during cooling when Zr saturation, or the solidus, is reached in leucosome domains (Kelsey et al., 2008; Kelsey and Powell, 2011; Kohn et al., 2015; Rubatto, 2017). Kelsey et al. (2008) showed that zircon growth is initially rapid and slows with decreasing temperature; in their models, >40% of zircon crystallizes within ~50 °C of the 100% Zr solubility contour, thus skewing zircon ages toward higher temperatures.

Rubatto (2002) described zircon that crystallized during HT metamorphism in equilibrium with partial melt that has a composition similar to that of magmatic zircons with a positive Ce anomaly, negative Eu anomalies (Eu/Eu* = 0.08–0.41), and steep REE patterns with HREE enrichment—all characteristics of Ledge Mountain zircons (Fig. 11; Fig. S2 [footnote 1]). The only measured chemical characteristic distinguishing these zircons from magmatic zircons is their low Th/U ratios (<0.07). Monazite is rare in thin sections of Ledge Mountain migmatites, but monazite crystallization is unlikely to affect the Th/U ratio of zircon in an effectively open system (i.e., see Discussion regarding melt connectivity; Rubatto, 2002).

Besides zircon, the only other phases present in Ledge Mountain migmatites to incorporate enough Zr to produce new zircon upon breakdown are garnet and ilmenite (Bingen et al., 2001; Hoskin and Schaltegger, 2003). Rutile is rare, but present, in Ledge Mountain rocks; our models show a maximum of ~0.2 wt% rutile at peak temperature conditions, and it is replaced by ilmenite within <20 °C of cooling. Textural evidence and results of modeling suggest that garnet breakdown coincided with increasing melt fraction, and so the melt would have been increasingly HREE enriched. The typical (but simplistic) interpretation of the REE patterns for zircon rim domains is that the presence of an Eu anomaly and the lack of HREE depletion suggests that zircon rims grew with plagioclase present and not garnet, interpreted to mean that zircon grew at retrograde *P-T* conditions. It is subsolidus growth of zircon and

garnet that results in HREE depletion and production of a flat or negative HREE slope, which is not seen in Ledge Mountain zircons (Rubatto, 2002); however, the total Zr and REE budget may have been affected by any melt loss events that may have taken place in Ledge Mountain migmatites and that would have shifted Zr dissolution contours to lower temperatures (Kelsey et al., 2008). How we interpret these Ti-in-zircon temperatures is further complicated considering they may reflect a closure temperature for diffusion in zircon based on its diffusion radius (Cherniak and Watson, 2003) rather than record the temperature of peak or even retrograde metamorphism. It is not clear how best to interpret these zircon crystallization temperatures, but it is likely that zircon crystallized after Ledge Mountain rocks had begun to cool from peak *P-T* conditions, and the calculated Ti-in-zircon temperatures of 734 °C to 790 °C corresponding to retrograde metamorphism of Ledge Mountain migmatites are reasonable.

### *Titanium-in-Zircon Thermometry*

Titanium-in-zircon temperature estimates for metamorphic and anatectic zircon crystallization in the Ledge Mountain samples fall between 734 and 790 °C (Fig. 11F; Fig. S2 [footnote 1]; Ferry and Watson, 2007; Schiller and Finger, 2019). Temperature estimates for magmatic zircon domains range from 809 to 981 °C.

Titanium-in-zircon thermometry has been used widely to estimate peak conditions in granulites and UHT granulites, but temperature results commonly fall on the retrograde path (e.g., Baldwin et al., 2007; Ewing et al., 2013; Kelsey and Hand, 2015; Clark et al., 2019). Clark et al. (2019) reported that Ti-in-zircon thermometry applied to granulites from East Antarctica returned temperatures ~70–230 °C lower than estimated peak temperatures of 910 ± 50 °C based on Al-in-orthopyroxene thermobarometry, Zr-in-rutile thermometry, and phase equilibria modeling combined with calculated compositional isopleths. Several studies of UHT granulites show that zircon crystallization takes place on the retrograde cooling path, resulting in Ti-in-zircon temperatures below peak conditions as documented by phase equilibrium modeling, Zr-in-rutile thermometry, and reaction microtextures between sapphirine and quartz, for example (Baldwin et al., 2007; Ewing et al., 2013; Kelsey and Hand, 2015; Clark et al., 2019). If zircon coexists with the Ti-bearing phase ilmenite instead of rutile, a minimum temperature for the UHT event may be obtained using Ti-in-zircon thermometry (Harley, 2008). Kelsey and Hand (2015) noted several reasons why Ti-in-zircon thermometry may not record UHT temperatures, including zircon growth that post-dated peak metamorphic conditions; undersaturation in $TiO_2$ or $SiO_2$; recrystallization of zircon; and disequilibrium partitioning of Ti in zircon or between zircon and quartz, rutile, or ilmenite. Ti-in-zircon thermometry also commonly records conditions at or near solidus temperatures on the retrograde *P-T* path (Kelsey and Hand, 2015). Additional data are needed to interpret Ti-in-zircon thermometry when estimating peak *P-T* conditions for UHT migmatites because zircon can grow over such a large range of thermodynamic and chemical conditions. Zircon crystallizes from a melt at post-peak metamorphic conditions to near-solidus conditions on the retrograde *P-T* path to ~200 °C below the solidus (Kelsey and Hand, 2015, and references therein; Clark et al., 2019).

## PHASE EQUILIBRIA MODELING

All 38 analyzed samples were modeled using Perple_X, and five representative migmatite samples were chosen—based on their preserved high-grade minerals such as garnet, sillimanite, and rutile and a relative lack of retrogression observed in hand specimen and thin section—for more extensive thermodynamic modeling and incorporation of isopleth models of mineral compositions. Limitations of these modeling methods are included in Text S1 (footnote 1). Samples 5-6, 17LM04, AD-01, and 001HG are granitic migmatites, and sample 11 is a metaleucotonalite (Figs. 13A–13D; Tables 1, 6; Connolly, 2005, 2009). Prominent but localized sillimanite-quartz layers were avoided during sampling.

We recognize two groups of pseudosection topologies in these five samples: models for samples AD-01, 17LM04, and 11 are similar (group 1; Fig. 13A); and models for samples 5-6 and 001HG are similar (group 2; Fig. 13C). We distinguish the two different topologies based on the general shape of the stability fields and the location (in *P-T* space) of the major metamorphic reactions, but the two groups nevertheless yield similar *P-T* conditions for the peak and retrograde metamorphic events.

Peak metamorphic conditions in all samples are represented by the assemblage plagioclase + K-feldspar + quartz + garnet + sillimanite ± rutile + melt. In all samples, retrograde overprint conditions are represented by the biotite-bearing assemblages at low *P-T* conditions and by the assemblage biotite + plagioclase + K-feldspar + quartz + garnet + ilmenite ± sillimanite + melt. Biotite is interpreted as not being in equilibrium texturally with the peak mineral assemblages, and biotite appears only at lower *P-T* conditions in pseudosection models (<~800 °C). All models show that abundant melt is present at peak conditions through near-isothermal decompression.

Group 1 samples (AD-01, 17LM04, and 11; Figs. 13A, 13B) are Sil-bearing migmatites. Sample 11 is texturally different from samples AD-01 and 17LM04 because it contains more plagioclase, no K-feldspar, and less accessory Bt and Ilm, but pseudosection topologies between these three samples are nearly identical. Group 2 samples (5-6 and 001HG; Figs. 13C, 13D) are fine- to medium-grained, K-feldspar-rich migmatites. Sample 001HG differs from sample 5-6 in that it does not contain sillimanite, but the pseudosection topologies for these two samples are otherwise nearly identical.

Major element zoning in garnets in all samples is weak, showing no systematic pattern, or is non-existent (Fig. 8). Modal estimates (Table 1) are based on hand specimens and petrography. Samples selected for thermodynamic modeling all have low modal percentages (<5%) of the key minerals garnet and sillimanite. We do not attempt to assess precise percentages for these and other accessory minerals and do not rely on calculated modal percentages to constrain peak *P-T* conditions. Rather, calculated garnet and sillimanite isopleths are overlain on modeled phase equilibria and are used to check whether isopleth models are consistent with the low modal percentages of these minerals that we observed in the rocks. In all samples, retrograde

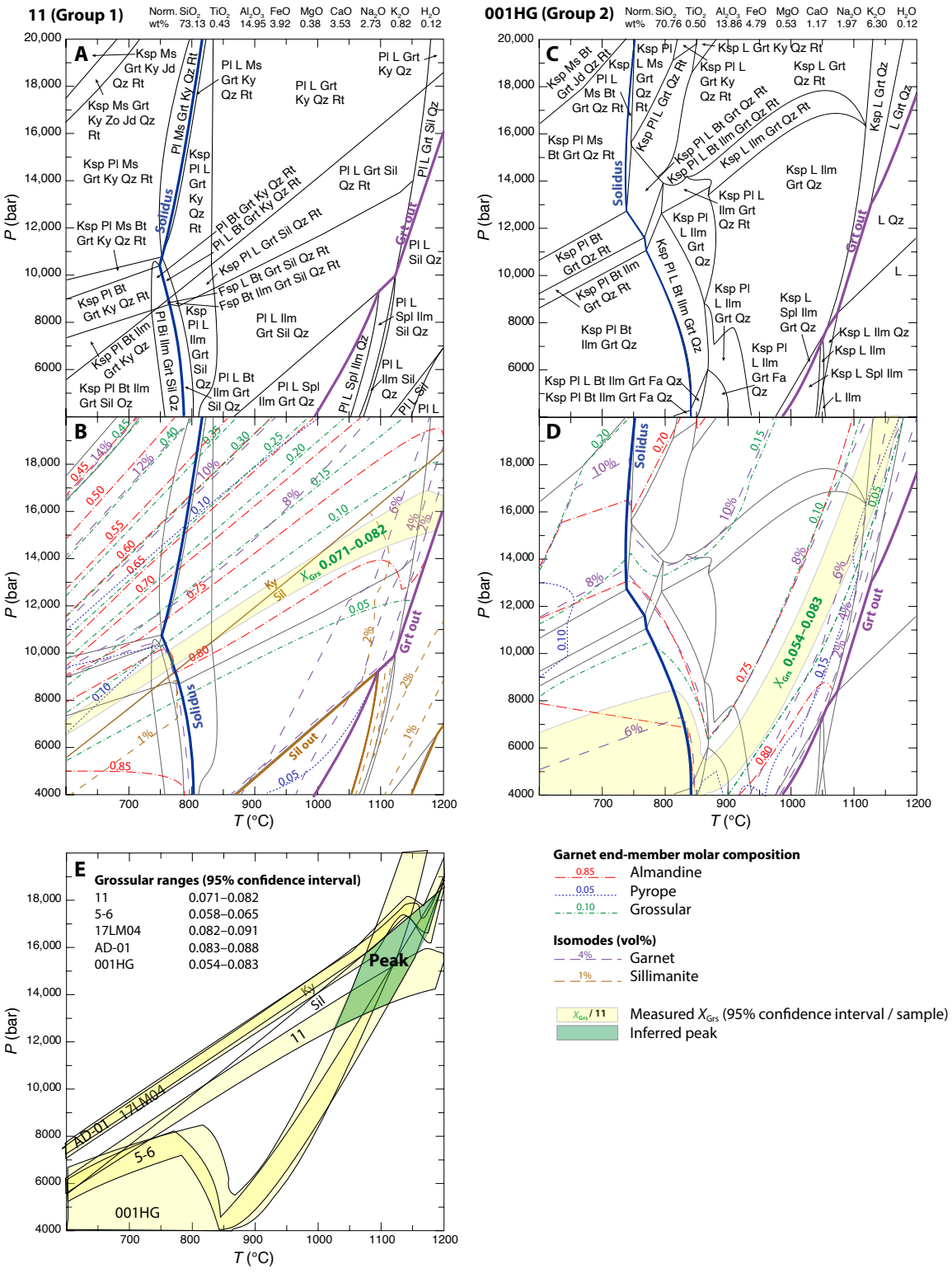


**Figure 13. (A, C) Pseudosections (isochemical phase diagrams) calculated using the igneous set of solution models (see text) for representative samples 11 (A) and 001HG (C) showing equilibrium mineral assemblages across the range 600–1200 °C and 4–20 kbar. Group 1 pseudosections include samples 11, AD-01, and 17LM04; group 2 pseudosections include samples 5-6 and 001HG (see Table 1). Values at top are whole-rock major element compositions for samples 11 (in A) and 001HG (in B). Norm—normalized. Garnet end-member isopleths and modal percentages of sillimanite and garnet superimposed on pseudosections A and C (mineral assemblages are removed for clarity). Yellow fields represent the 95% confidence intervals for the grossular component of garnet from mineral composition data (Table 2; Table S2 [see text footnote 1]). (E) Grossular components ($X_{Grs}$; 95% confidence interval) of garnets from samples 11, 001HG, AD-01, 17LM04, and 5-6 compiled to show the region of intersection that represents the pressure-temperature (*P-T*) conditions for peak metamorphism. Pseudosections and grossular data for samples AD-01, 17LM04, and 5-6 are calculated but not shown; only their grossular ranges are shown in E. Bt—biotite, Fa—fayalite, Fsp—feldspar, Grs—grossular, Grt—garnet, Ilm—ilmenite, Jd—jadeite, Ksp—K-feldspar, Ky—kyanite, L—liquid, Ms—muscovite, Pl—plagioclase, Qz—quartz, Rt—rutile, Sil—sillimanite, Spl—spinel, Zo—zoisite.**

conditions are represented by the chlorite- and biotite-bearing overprinting assemblages at low *P-T* conditions (Figs. 6B, 6C, 7B, 7C). The general consistency between the pseudosection topologies, textural data, and mineral compositions suggests that the pseudosection approach is suitable for inferring *P-T* conditions in these migmatitic felsic granulites (Indares et al., 2008). A first set of pseudosections was constructed using the measured bulk composition of each sample that represents the final rock composition, and not the prograde evolution, because early melt was undoubtedly lost on the prograde path and prograde minerals were overprinted during peak temperature conditions and/or retrograde metamorphism. However, forward modeling demonstrates that different scenarios of melt loss do not have a significant effect on the suprasolidus topologies or on the compositions of solid phases (e.g., Indares et al., 2008; Guilmette et al., 2011; Groppo et al., 2012). Therefore, this set of pseudosections allows the exploration of the phase equilibria at near-peak granulite-facies conditions.

## Phase Equilibria Modeling Methods

Pseudosections were created using the phase equilibria modeling program Perple_X version 6.8.9 (and corresponding data files; Connolly, 2005, 2009) and an internally consistent thermodynamic database for minerals and water (CORK model; Holland and Powell, 1991, 2001, 2011). Pseudosections were constructed using the whole-rock geochemical data in Table 6 for pressures of 4–20 kbar and temperatures of 600–1200 °C. We use sample 11 as an example of group 1 models and sample 001HG to represent group 2 models in Figure 13.

To account for possible variation in protolith type, we use two set of solution models and thermodynamic datafiles (Fig. 13). An "igneous set" of data files includes the thermodynamic data file *hp633ver.dat* (Holland and Powell, 2011; Holland et al., 2018) and solution models for the partial melting equilibria involving basaltic through granitic melts: melt [*melt(HGP)*], spinel [*Sp(HGP)*], biotite [*Bi(HGP)*], and garnet [*Gt(HGP)*; Holland et al., 2018]. Calculations using the igneous set were performed in the $Na_2O$-CaO-$K_2O$-FeO-MgO-$Al_2O_3$-$SiO_2$-$H_2O$-$TiO_2$ (NCKFMASHT) model system. A "metapelite set" of data files includes the thermodynamic data file *hp62ver.dat* (Holland and Powell, 2011; Green et al., 2016) and solution models for equilibria in metapelitic bulk compositions: melt [*melt(W)*], biotite [*Bi(W)*], garnet [*Gt(W)*; White et al., 2014a], and spinel [*Sp(WPC)*; White et al., 2002]. Biotite is "somewhat reparameterized" from White et al. (2014a). Calculations using the metapelite models were extended by White et al. (2014b) to include MnO and were performed in the MnNCKFMASHT system to include spessartine end-member calculations. Calculations using the igneous set were performed in the $Na_2O$-CaO-$K_2O$-FeO-MgO-$Al_2O_3$-$SiO_2$-$H_2O$-$TiO_2$ (NCKFMASHT) model system. Both model sets also use the following solution models: white mica [*Mica(W)*; White et al., 2014a]; ilmenite [*Ilm(WPH)*; White et al., 2000, 2007]; and ternary feldspar [*feldspar*; Fuhrman and Lindsley, 1988]. The margarite ("*ma*") end member was excluded from calculations to avoid conflicts with *Mica(W)*. The "*ilm*" and "*ilm_nol*" solution phases were excluded to use the *Ilm(WPH)* model, which enables the calculation of ilmenite, hematite, and geikeilite end members. Calculations used the whole-rock geochemical data from Ledge Mountain for samples 5-6, 17LM04, AD-01, 001HG, and 11 (Fig. 13; Table 6).

Estimation of bulk-rock $Fe_2O_3$ is problematic because it was not measured by XRF analysis. Calculation of $Fe^{3+}$ from microprobe analyses of spinel (0.00–0.03 $Fe^{3+}$ a.p.f.u.), garnet (0.00–0.05 $Fe^{3+}$ a.p.f.u.), and sillimanite (0.00–0.27 $Fe^{3+}$ a.p.f.u.) shows that these phases have very low $Fe^{3+}$ contents, suggesting that the bulk-rock composition is similarly low in ferric iron (Sarkar and Schenk, 2014; Walsh et al., 2015). Magnetite composed <1% of the modeled rocks (see below), and stoichiometry estimates that <0.07% $O_2$ should be used in modeling, which the model converts to $Fe_2O_3$; adding $O_2$ to correct for ferric iron resulted in only rare magnetite in our models (that is present in these rocks at <1%), irregular phase boundaries and islands, destabilization of rutile across the *P-T* range, and the appearance of several minerals (e.g., zoisite) across the pseudosection at low *P-T* conditions that have not been observed in thin section. Kendrick and Indares (2018) reported that increasing $O_2$ in phase equilibria models for anatectic aluminous granulites from the central Grenville province had little effect on the overall topologies for the relevant assemblages. For these reasons, no ferric iron ($O_2$) was used in our models.

To understand how individual minerals behaved at these conditions, isopleth models for mineral compositions were generated in Perple_X and overlaid onto the pseudosections. Several components were selected for isopleth contouring based on petrographic observations: garnet end members (Fe, Mg, Ca) and the percentage of garnet and sillimanite in the rock. We did not include feldspar isopleths because it is unclear texturally which feldspar grains grew during peak conditions and which grains resulted from retrograde reactions. Mineral compositions used to interpret isopleth models are from electron microprobe analysis (Tables 2–5).

## Estimating $H_2O$ Content

The $H_2O$ content of geochemical systems can potentially have a large effect on the temperature of the solidus in our models, so it is important to have a better constraint on the $H_2O$ content than loss-on-ignition (LOI) values offer (Hasalová et al., 2007; Bartoli, 2017). We estimate the percentage of $H_2O$ in our migmatite samples at 0.12 wt% based on the amount of biotite they contain (the molar percentage of $H_2O$ in biotite is ~4% g $H_2O$/g biotite; Lechler and Desilets, 1987; Indares et al., 2008). Retrograde biotite must be a minimum percentage of biotite if we assume no external fluids were introduced, as textures indicate. Retrograde biotite resulted from the breakdown of garnet, and peritectic garnet crystallized from the original amount of biotite that had been present in the rocks at prograde conditions. We would underestimate the biotite content only if biotite were removed with any leucocratic melt loss. We show that the melanosome is enriched in biotite and did not enter the leucocratic melts, thus making our estimate of the biotite percentage a valid proxy for the $H_2O$ content in these rocks.

Except in melanosome domains adjacent to pegmatitic leucosome, biotite composes ≤1%–3% of the volume in all migmatites. Indares et al. (2008)

performed forward modeling using 0.35–0.62 wt% $H_2O$ for kyanite-bearing paragneisses from the central Grenville province that contain slightly more biotite than our samples; given the lesser amount of biotite in our samples, using 0.12 wt% $H_2O$ in our models is reasonable.

To test this $H_2O$ estimate based on biotite content, we modeled temperature versus molar composition $H_2O$ at the pressure producing the current stable solid assemblage in preliminary thermodynamic models (6 kbar; Fig. 14) following a method similar to that of Hasalová et al. (2007), Bartoli, (2017), and White et al. (2005). The range of $H_2O$ values is determined where the observed assemblage K-feldspar + Plagioclase + Liquid + Biotite + Ilmenite + Garnet + Sillimanite + Quartz stabilizes at lower suprasolidus conditions—at the *P-T* conditions where the final melt fraction would have crystallized (White et al., 2005); textural evidence of the presence of former melt films can be seen in Figures 5F, 7B, and 7C. This model yielded $H_2O$ concentrations of 0–0.45 wt% $H_2O$ (Fig. 14), which is consistent with the low volume of hydrous minerals (i.e., biotite) observed in Ledge Mountain granulites and includes our best estimated value of 0.12 wt% $H_2O$ that was derived from the biotite content in our samples (≤3%). Because results of these two methods to estimate $H_2O$ content are similar, we chose to use the far simpler method of calculating $H_2O$ values from the biotite content.

Our forward modeling assumes a low $H_2O$ content based on the observation of a maximum of 3% hydrous minerals (biotite) observed across all samples (0.12 wt% $H_2O$; Figs. 15A, 15B). To better understand the effect of using higher $H_2O$ estimates, we also ran models with 1.23 wt% $H_2O$ (Figs. 15C, 15D) that derives from the 1.227 wt% $H_2O$ value used by Storm and Spear (2005) for metapelitic rocks in the southern Adirondack Highlands. Increasing $H_2O$ content to 1.23 wt% represents a tenfold increase in $H_2O$ content over our best estimate and overestimates the amount of biotite in Ledge Mountain granulites. We use this high estimate of 1.23 wt% $H_2O$ to test the reasonable range of *P-T* conditions for peak metamorphism of Ledge Mountain migmatites.

Using 1.23 wt% $H_2O$ shifts our peak fields to lower temperatures by ~50 °C and shifts the solidus by ~100 °C to lower temperatures and water-saturated conditions. Increasing the amount of water in our models decreases the temperature indicated by the peak fields by ~50–100 °C per weight percent $H_2O$ (Fig. 15E). Even adding as much as 2 wt% $H_2O$ to the igneous models—nearly 20 times our best estimate based on the amount of biotite—shows that Ledge Mountain rocks were still metamorphosed at temperatures >900 °C (UHT granulite-facies conditions). Our models required the addition of >3 wt% $H_2O$ to shift the peak field to sub-UHT conditions.

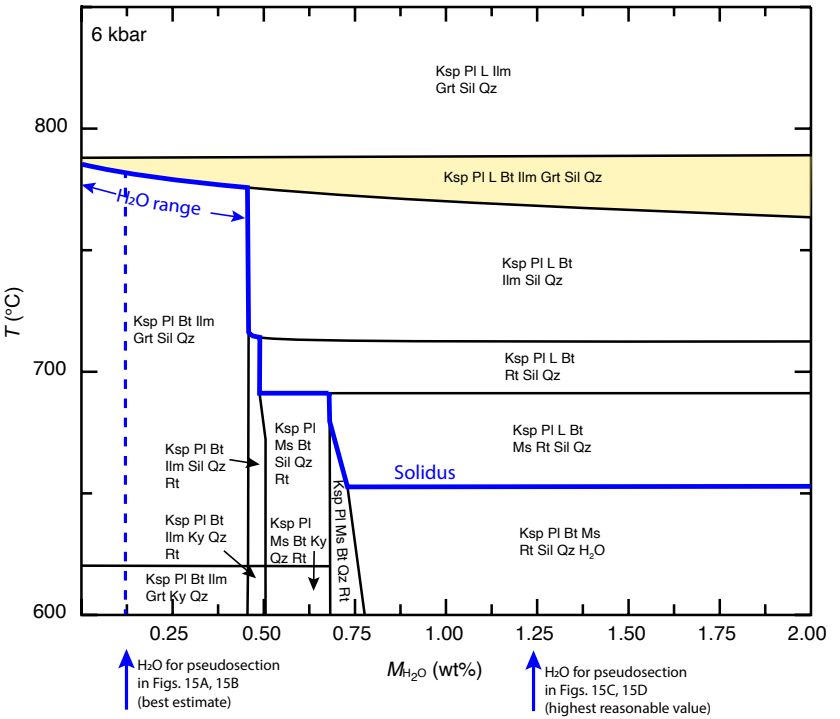


**Figure 14. Temperature versus molar composition $H_2O$ ($T$-$M_{H2O}$) diagram calculated at 6 kbar using the igneous set of solution models (NCKFMASHT; see text). The range of 0–0.45 wt% $H_2O$ corresponds to where the observed current solid assemblage (yellow field) stabilizes at the solidus where the last melt fraction crystallizes. Our best estimate of 0.12 wt% $H_2O$, calculated from the volume of hydrous minerals observed in thin section, falls within this range and agrees with these results (Figs. 15A, 15B). The high estimate of 1.23 wt% $H_2O$ falls outside of this model's range—representing a tenfold increase over our best estimate for water content—and was used to test phase equilibria models with a significantly higher water content and has the effect of reducing the estimated metamorphic temperatures for our peak assemblage (see Figs. 15C, 15D). Bt—biotite, Grt—garnet, Ilm—ilmenite, Ksp—K-feldspar, Ky—kyanite, L—liquid, Ms—muscovite, Pl—plagioclase, Qz—quartz, Rt—rutile, Sil—sillimanite.**

## Melt Reintegration and Assessment of Melt Loss

Observations of Ledge Mountain migmatites in thin section indicate evidence for at least 15%–30% melt in most rocks (Table 1). Diatexite migmatites begin to lose their pre-anatectic structures and develop flow foliations when they meet a critical melt fraction between 0.26 and 0.40 (also the melt escape threshold); in some cases, this is as low as 0.20 and

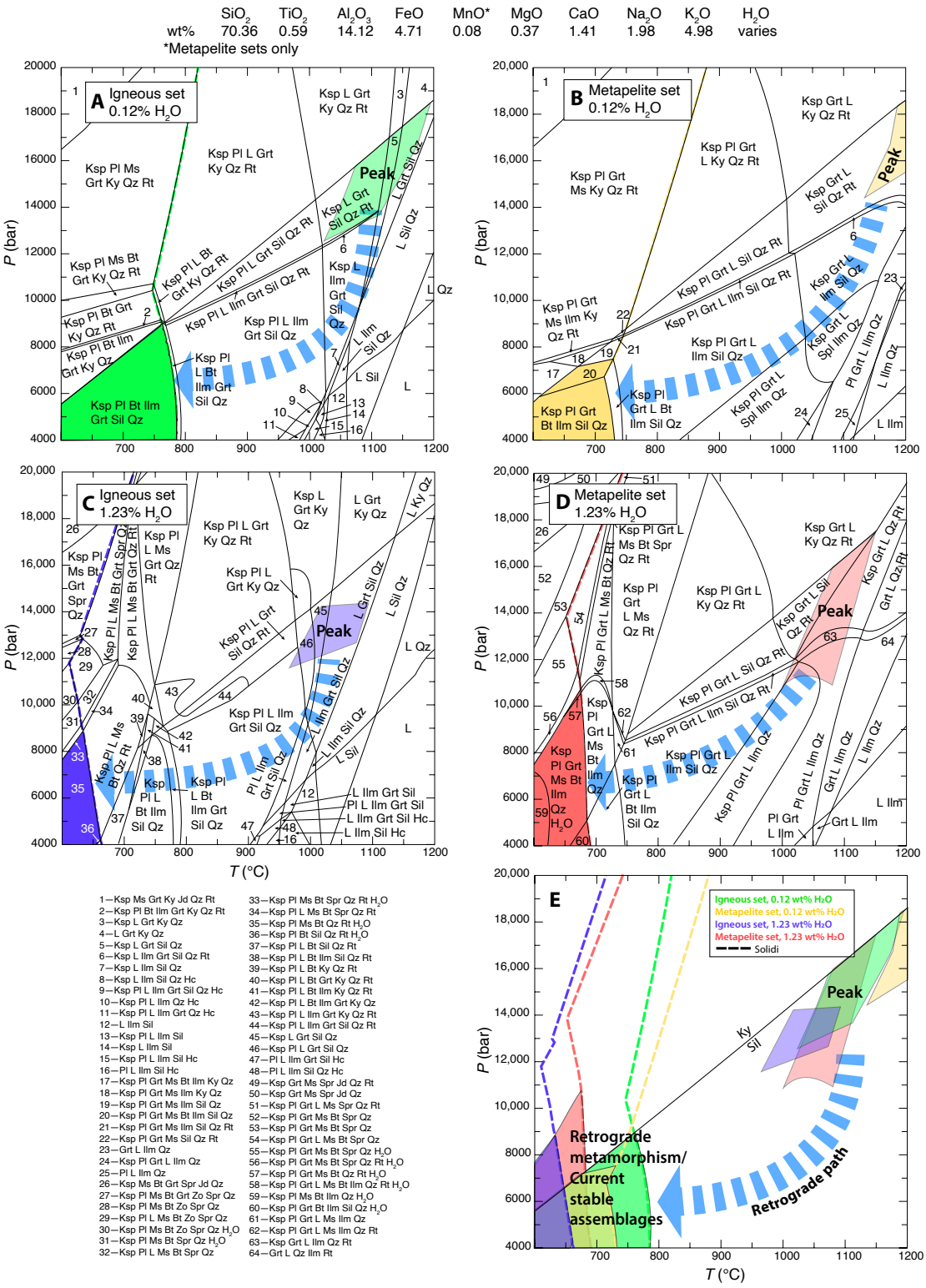


**Figure 15. Pseudosections comparing the effect of using igneous or metapelite model sets and varying $H_2O$ content for peak pressure-temperature (*P-T*) conditions. Pseudosections are calculated using the igneous set of solution models (A, C) or the metapelite set of solution models (B, D) (see text for details of solution models used) and varying water content from 0.12 wt% $H_2O$ (A, B) to 1.23 wt% $H_2O$ (C, D). Values at top are whole-rock major element compositions for the average of 11 migmatite samples (001HG, 003HG, 5-6, AD-01a, AD-01b, 17LM02, 17LM03, 17LM04, 17LM05, 17LM06, and 17LM07) used in this pseudosection model; Table S1). Lighter-color fields represent peak metamorphic conditions: the peak field in A (light green) is the same peak field determined in Figure 13E; peak fields in B, C, and D are calculated using the same method as for A, only the solution model set and/or water content is changed. Darker-color fields represent retrograde assemblages corresponding to the current solid assemblages observed in thin sections of these samples. Dashed blue arrows are the estimated *P-T* paths. (E) Peak and retrograde fields from A–D are superimposed to show the range of possible *P-T* conditions for peak and retrograde metamorphism. Bt—biotite, Fa—fayalite, Fsp—feldspar, Grs—grossular, Grt—garnet, Hc—hercynite, Ilm—ilmenite, Jd—jadeite, Ksp—K-feldspar, Ky—kyanite, L—liquid, Ms—muscovite, Pl—plagioclase, Qz—quartz, Rt—rutile, Sil—sillimanite, Spl—spinel, Spr—sapphirine, Zo—zoisite.**

not normally >0.70 (Sawyer, 2008). The topologies in the lower-temperature part of our pseudosections are consistent with melt loss and thus fail to explain the prograde evolution of the rocks. These models are intended to represent the peak metamorphic temperature history of Ledge Mountain migmatites. If leucosome is in situ and no melt has been lost, then the bulk composition of homogenized migmatite samples represents the original protolith composition. In Ledge Mountain samples, the observed and modeled large fraction of melt indicates that at least some melt has segregated away from its source or melt may have been lost from the system entirely, and the protolith composition must be reconstructed. Melt reintegration approximates the prograde metamorphic history by revealing the estimated protolith composition and likely melt-loss volume on the *P-T-t* path (Bartoli, 2017). We used the single-step melt reintegration approach described by Bartoli (2017) and developed by Indares et al. (2008) and Lasalle and Indares (2014).

Melt is reintegrated by adding fractions of the molar composition of the estimated leucosome melt back into the measured whole-rock composition using progressively higher melt fractions. Melt compositions can be estimated for nanogranite inclusions in large peritectic garnet grains using electron microprobe mineral composition data. In our case, we used the composition of the melt being generated in our model at the estimated peak *P-T* conditions for Ledge Mountain migmatites. Pseudosections of the melt-reintegrated compositions are generated until the solidus becomes saturated with $H_2O$, the hypothetical conditions at which the protolith began to lose melt (Bartoli, 2017). We reintegrated from 5% to 60% melt—i.e., corresponding to 4.8–37.5 vol% melt loss—for sample 5-6 to test whether melt has been lost from the system.

Reintegrating 40% of the calculated melt composition into the modeled whole-rock composition represents a protolith composition from which ~29 vol% [40% melt / (40% melt + 100% original whole rock)] was lost from the modeled rock. The minimum metamorphic temperature for the peak assemblage decreased 25 °C to ~925 °C, and the maximum temperature decreased 20 °C to ~1100 °C after reintegrating 40% melt. The maximum pressure decreased by ~500 bar. While melt reintegration results in minor shifts in the pseudosection fields, the field representing the peak mineral assemblage is largely unchanged. We therefore infer that the modeled compositions do not differ significantly from the protolith composition and that the whole-rock compositions we used are a good proxy for protolith compositions, even if significant melt (~29%) was lost from the system. Future work will involve melt reintegration to study the prograde path.

### Estimated Peak *P-T* Conditions

The inferred peak assemblage of plagioclase ± K-feldspar + quartz + garnet ± sillimanite + liquid + ilmenite ± rutile is stable from the solidus at amphibolite-facies conditions through UHT granulite-facies conditions, and so the peak *P-T* conditions cannot be inferred from the stable mineral assemblage alone. Overlaying isopleths for the grossular component of garnet from several samples should show peak *P-T* conditions where grossular isopleths intersect the peak mineral assemblage (Li et al., 2019; Indares, 2020). Calcium diffusion in garnet is much slower than that of Fe and Mg, resulting in little change from peak conditions, whereas the higher Fe and Mg diffusion rates probably capture retrograde conditions at the solidus (Chakraborty and Ganguly, 1992; Hollis et al., 2006; Li et al., 2019). We replicated this method of using grossular isopleths for our five modeled samples (5-6, 11, 17LM04, AD-01, 001HG) to find the *P-T* region of their intersection (e.g., Figs. 13B, 13D). Figure 13E shows grossular isopleths that trace 95% confidence intervals for mineral composition data from those five modeled samples (Table S2 [footnote 1]); these isopleths intersect in the region of ~1025–1190 °C and 12.5–18.5 kbar, indicating that peak metamorphism took place at UHT granulite-facies conditions.

The igneous set of solution models and 0.12 wt% $H_2O$ were used to generate pseudosections and isopleths (e.g., Fig. 13). The "peak" *P-T* field is determined at the approximate intersection of the peak mineral assemblage with the 95% confidence intervals for the grossular isopleths and is limited in pressure to the sillimanite stability field. This process was repeated with 1.23 wt% $H_2O$ and also using the metapelite set of solution models with both 0.12 and 1.23 wt% $H_2O$. Our estimated peak metamorphic conditions fall within the UHT granulite facies in all cases (e.g., Figs. 13B, 13D).

A second set of pseudosections was generated using an average migmatite composition to better capture the protolith composition. The average migmatite composition is based on 11 granitic migmatite samples—001HG, 003HG, 5-6, AD-01a, AD-01b, 17LM02, 17LM03, 17LM04, 17LM05, 17LM06, and 17LM07 (Fig. 15; Table S1 [footnote 1])—that are all similar in mineralogy and texture. The "peak" fields in Figure 15E represent the combined results of all model sets (igneous and metapelite) and water contents (0.12 and 1.23 wt%). Models based on this average composition are similar to those calculated for individual migmatite samples (e.g., Fig. 13).

Our best estimate for peak metamorphism of Ledge Mountain migmatites is 1025–1190 °C and 12.5–18 kbar, which was established using the igneous solution models and 0.12 wt% $H_2O$ (Fig. 15A). Models using the metapelite set of solution models and 0.12 wt% $H_2O$ result in increased peak temperatures to >1140 °C and represent maximum *P-T* conditions of metamorphism for Ledge Mountain migmatites (Fig. 15B). Increasing water content to 1.23 wt% in the igneous models resulted in a 60 °C decrease in peak temperatures to a minimum of 960 °C (Fig. 15C). Combining the metapelite model set with 1.23 wt% $H_2O$ lowered the peak metamorphic pressure to a minimum of 11 kbar (Fig. 15D). For all models, the minimum conditions for peak metamorphism are 960 °C and 11 kbar based on 1.23 wt% water (Figs. 15C, 15D). Results are summarized in Figure 15E.

## DISCUSSION

### Timing of Metamorphism at Ledge Mountain

Our multimethod study of felsic migmatites exposed at Ledge Mountain provides insights into the late Ottawan evolution of the central Adirondack Highlands, part of the hinterland of the Mesoproterozoic

Grenville province. New U-Pb zircon data indicate that Ledge Mountain experienced Ottawan to post-Ottawan metamorphism and anatexis (1085 ± 13 to 959 ± 14 Ma; Table 7; Fig. 12); analyses of metamorphic zircon rims from migmatites (i.e., lacking pegmatitic leucosome; samples 001HG and 004HG) give a mean age of 1047.0 ± 4.6 Ma, which probably records recrystallization of zircon at granulite-facies conditions on the retrograde cooling path following passage through peak UHT granulite-facies conditions. The mean age of zircon crystallization from melanosome of 1035.2 ± 2.4 Ma may also record dissolution and/or (re)crystallization following extraction of leucocratic melts and may indicate a prolonged period of metamorphism and alteration and melting during the Ottawan at 1047.0 ± 4.6 to 1035.2 ± 2.4 Ma.

Ages for zircon rims extend nearly continuously from the early Ottawan (1085 ± 13 Ma) through to the three youngest zircon rim ages for a pegmatitic leucosome (mean of 968 ± 5 Ma). These late (post-Ottawan) dates could record an influx of fluids (e.g., hydrothermal alteration) that is reported elsewhere in the Highlands (e.g., McLelland et al., 2002); however, zircon does not display textures typical of crystallization from hydrothermal fluids (see above and Text S1 [footnote 1]) nor is there evidence of extensive retrogression or alteration of Ledge Mountain migmatites. Alternatively, the late zircon dates could record final crystallization of anatectic melts or crystallization of melts produced during decompression on the retrograde cooling path.

## Conditions of Metamorphism

Estimated peak *P-T* conditions for the sillimanite-bearing migmatites ranged from 960 to >1140 °C and 11–18 kbar, based on pseudosection models using both igneous and sedimentary solution models, Ca-in-garnet isopleths, and variable $H_2O$ contents (Figs. 15, 16). Across all models and water contents, models yield peak conditions of at least 960 °C and 11 kbar (Fig. 15E). Temperatures representing the upper end of these ranges are among the highest reported for UHT terranes worldwide (e.g., Harley, 2004; Brown; 2014; Kelsey and Hand, 2015) and seem unlikely for the Adirondack Highlands. However minimum peak conditions of 960–1025 °C and 11–12.5 kbar—determined using the igneous solution models—seem reasonable for lower-crustal granulites that were exhumed in a migmatitic gneiss dome (Figs. 15, 16). These *P-T* conditions are consistent with recently reported *P-T* estimates of 950 ± 40 °C and 8.5–10 kbar for Gore Mountain amphibolite based on conventional thermobarometry and thermodynamic modeling (Shinevar et al., 2021).

Observed mineral assemblages and pseudosection models suggest that our peak conditions start in the sillimanite stability field at UHT granulite facies near the dry granite solidus (Fig. 16A). Peak metamorphism and anatexis is followed by near-isothermal decompression then isobaric cooling to amphibolite-facies retrograde conditions (Fig. 16A). Isothermal decompression is indicated by decompression textures including biotite symplectite (Fig. 7D) and ilmenite-after-rutile relationships (Fig. 6D), for example. The inferred overall *P-T-t* paths are similar for the five modeled Ledge Mountain granulites, in spite of petrographic variability, and involved isothermal decompression during buoyancy- and fault-driven exhumation followed by isobaric cooling (Fig. 16A). Our estimates of peak conditions are compatible with extensive petrographic evidence for melting and represent significantly higher metamorphic temperatures and pressures than previously reported for the Adirondack Highlands (600–850 °C and 6–8 kbar; Fig. 16A; e.g., Bohlen and Essene, 1977; Bohlen et al., 1980, 1985; Spear and Markussen, 1997; Storm and Spear, 2005); the latter are used to constrain the retrograde path for Ledge Mountain granulites.

Ledge Mountain migmatites contain spinel + quartz, an assemblage which in itself is not diagnostic of UHT metamorphism because the incorporation of minor elements such as $Fe^{3+}$, Zn, and Cr in spinel is known to extend the stability of this assemblage to lower temperatures (e.g., Pownall, 2015, and references therein). Although this study does not include a thorough investigation of the composition and complex microtextures of the Fe-Ti-Al oxides in Ledge Mountain rocks, the presence of spinel + quartz assemblages, which include hercynitic spinel with low $Fe^{3+}$ and Cr contents and, in sample 001HG, low to moderate ZnO (2.51–2.73 wt%), is consistent with UHT metamorphism.

## Partial Melting of Older Plutonic Rocks

Crustal reworking and emplacement of leucogranites is widespread in the waning stages of collisional orogenesis (e.g., Selleck at al., 2005), and the ca. 1050 Ma Lyon Mountain Granite is considered a hallmark of late- to post-Ottawan orogenic collapse and extension (McLelland et al., 2002; Valley et al., 2011; Chiarenzelli et al., 2017). Based on major and trace element whole-rock geochemistry, Ledge Mountain migmatites closely resemble the Lyon Mountain Granite, and the presence of xenocrystic zircon cores as old as 1195 Ma from Ledge Mountain migmatites suggests that, like the Lyon Mountain Granite, Ledge Mountain rocks were derived by partial melting of older plutonic rocks (Chiarenzelli et al., 2017). Whole-rock major element composition is consistent with an igneous protolith for the Ledge Mountain granulites (Fig. 9E).

Unlike the Lyon Mountain Granite, the Ledge Mountain rocks are not associated with iron oxide–apatite deposits, lack evidence for extensive metasomatism, and contain minerals indicative of granulite-facies metamorphism (e.g., garnet, rutile, and prismatic sillimanite not associated with sillimanite-quartz segregations). A hydrothermal origin has been suggested for sillimanite-quartz nodules in the Lyon Mountain Granite (McLelland et al., 2002), but the absence of petrographic evidence for widespread alteration suggests that the local sillimanite-quartz layers observed at Ledge Mountain may have had a different origin.

We infer that the Ledge Mountain migmatites primarily represent melting of older plutonic rocks and that some melt was retained in a deep-crustal environment. According to Frost and Frost (2011), granitoids formed by partial melting of tonalites to granodiorites are metaluminous at low pressures; high pressures favor production of peraluminous melts. Partial melting at higher temperature and pressure than was the case for the Lyon Mountain Granite could explain the peraluminous nature of the Ledge Mountain granulites (Frost and Frost,

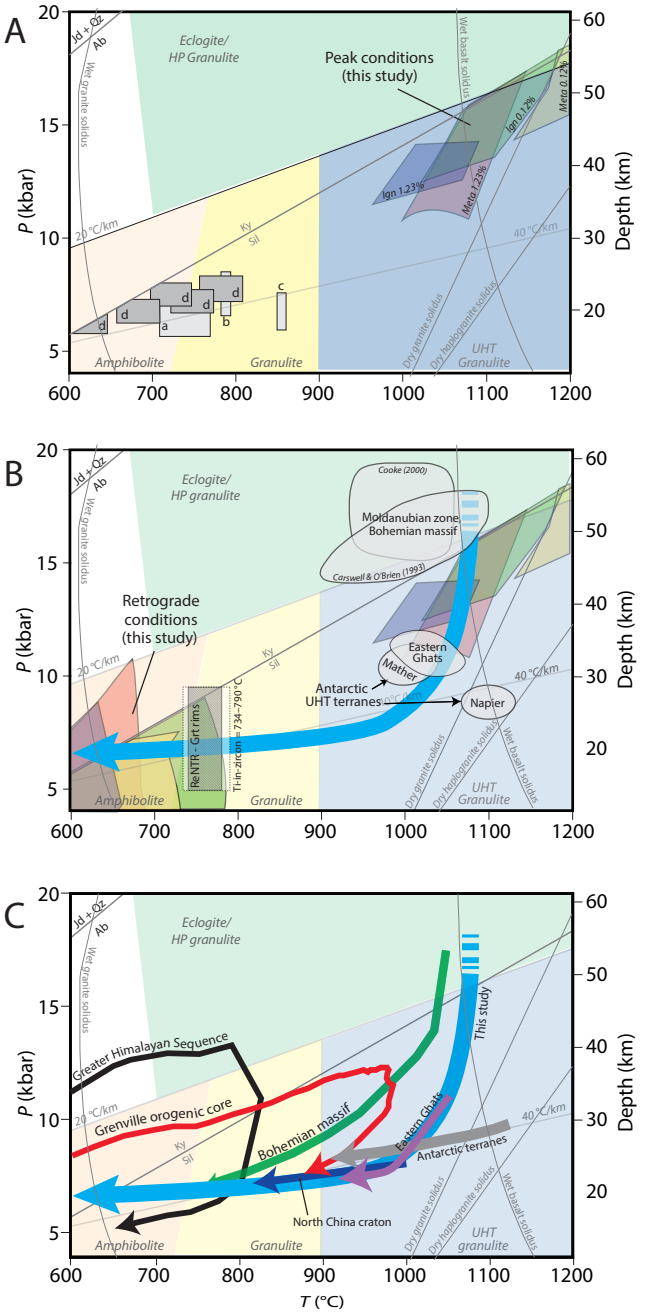


**Figure 16. Metamorphic phase diagrams. (A) Peak metamorphic conditions for Ledge Mountain rocks (colored fields from Figs. 15A–15D) are >100–200 °C higher than previous estimates from conventional thermobarometry (gray boxes a–d), and all fall within the ultrahigh-temperature (UHT) granulite-facies stability field. Retrograde, biotite-bearing assemblages correspond to earlier work from: a—Florence and Spear (1995); b—Storm and Spear (2005); c—Spear and Markussen (1997); d—Bohlen et al. (1985). Fields labelled Ign 0.12% (green), Ign 1.23% (purple), Meta 0.12% (yellow), and Meta 1.23% (red) are the peak metamorphic pressure-temperature fields using the igneous (ign) and metapelite (meta) model sets using 0.12% and 1.23% $H_2O$ shown in Figure 15. Amphibolite-, granulite-, UHT granulite-, and eclogite- or high-pressure (HP) granulite-facies metamorphism fields are shown for reference. Wet granite solidus from Huang and Wyllie (1975); wet tholeiitic basalt solidus from Nicholls and Ringwood (1973); dry haplogranite solidus is from Holtz et al. (2001); dry granite solidus is from Johannes and Holtz (1996). Ab—albite, Jd—jadeite, Ky—kyanite, Qz—quartz, Sil—sillimanite. (B) Data from A and retrograde conditions from this study shown in comparison to Antarctic UHT granulite terranes (the Napier Complex and Mather localities; Tsunogae et al., 2002; Harley, 2004, 2008), the Eastern Ghats region of India (Harley, 2004; 2008; Korhonen et al., 2011; Kelsey et al., 2017), and granulites from the Moldanubian Zone, Bohemian massif (the St. Leonhard and Dunkelsteiner Wald, Austria; Carswell and O'Brien, 1993; Cooke, 2000; Janoušek et al., 2004). Our models yield similar temperatures to these other UHT terranes. Ti-in-zircon thermometry yields temperatures between ~734 and 790 °C corresponding to fields for retrograde metamorphism (Fig. 11F) and retrograde net-transfer reaction (ReNTR) temperature estimates for garnet (Grt) rims based on Storm and Spear (2005). Peak pressure-temperature (*P-T*) stability fields for our models are followed by near-isothermal decompression then retrograde metamorphism along a near-isobaric cooling trend (blue arrow). (C) *P-T* path for Ledge Mountain rocks (blue arrow) developed from pseudosection modeling, mineral compositions, and petrography, and accounting for previous conventional thermobarometry results (see B). The thermo-mechanical model of Jamieson and Beaumont (2010) for Grenville-style lower crustal "orogenic core exhumed mainly by ductile thinning" (red line; from Jamieson and Beaumont, 2010, their model GO-3/GO-ST87) is shown for comparison. Large hot orogen middle crust represented by modeled Greater Himalayan Sequence rocks (black line; from Jamieson et al., 2004, their model HT1/G1) does not achieve UHT conditions. Our *P-T* path (blue) is similar to the exhumation path for the Bohemian massif (green line; after O'Brien, 2008, their fig. 17b), but Bohemian massif rocks have lower average temperatures. The definitive Antarctic UHT granulite-facies terranes (gray arrow), Eastern Ghats granulites (India; purple arrow), and Khondalite belt, North China craton (dark blue arrow) achieve comparable *P-T* conditions and follow exhumation paths that could fit our Ledge Mountain model, particularly from a depth of ~30 km and through our modeled retrograde conditions in B (Harley, 2004, 2008; Korhonen et al., 2011; Li et al., 2019; Kelsey et al., 2017).**

2011). However, in the absence of whole-rock Sr and Nd isotope data, mixing of melt with Al-rich metasedimentary material to produce a peraluminous composition cannot be ruled out.

## A Migmatitic Gneiss Dome in the Central Adirondacks

In orogenic belts around the world, gravitational collapse and extension have led to formation of metamorphic core complexes or granite-cored gneiss domes and the exhumation of deep, partially molten lower-crustal rocks (e.g., Whitney et al., 2004; Rey et al., 2009). In the Grenville province, late orogenic extensional deformation is being increasingly recognized as a mechanism for magma emplacement, exhumation, and the juxtaposition of different crustal levels to produce large metamorphic discontinuities (e.g., Rivers, 2008, 2012; Regan et al., 2019; Baird, 2020).

Within the central Adirondack Highlands, evidence provided by Regan et al. (2019) indicates that the Marcy anorthosite massif (Fig. 1) is structurally overlain by a domal, southeast-directed detachment zone that formed during the Ottawan orogeny at 1070–1060 Ma, just before and during emplacement of the ca. 1050 Ma Lyon Mountain Granite, and facilitated exhumation of lower-crustal rocks. Bohlen et al. (1980, 1985) noted a concentric pattern of metamorphic temperatures in the Adirondacks, with the highest temperature (>775 °C) centered on the Marcy massif and consistent with the anorthosite representing the structurally lowest rocks exposed in the Adirondacks (Regan et al., 2019).

The preservation of the inferred peak metamorphic assemblage at Ledge Mountain and the presence of only rare muscovite suggests some melt was lost from the system; however, microtextural evidence for the presence of in situ melt suggests that significant melt was ultimately retained (Fig. 7). Our pseudosection models indicate ~15%–30%+ melt during and following peak metamorphism, which far exceeds the 5%–7% melt connectivity transition required for ductile flow of these rocks and initiation of their buoyant uplift (Table 1; Rosenberg and Handy, 2005). The strength of Ledge Mountain migmatites at peak *P-T* conditions was close to the solid-to-liquid rheological transition that starts at 25%–40% melt (Rosenberg and Handy, 2005).

Anorthosite domes in the south-central Adirondack Highlands (Snowy Mountain and Oregon dome) and the Gore Mountain amphibolite experienced granulite-facies metamorphism during the Ottawan orogeny at ca. 1031 ± 30 Ma, 1048 ± 10 Ma, and 1041 ± 6 Ma, respectively, that is recorded in thin, unzoned rims on zircon (Hamilton et al., 2004). This timing is supported by a Lu-Hf isochron age for Gore Mountain garnets of 1047 ± 6 Ma (Connelly, 2006; McLelland and Selleck, 2011). Ledge Mountain migmatites (ca. 1047.0 ± 4.6 Ma), along with these other deep-crustal rocks, were undergoing concurrent high-grade metamorphism and melting in the Ottawan (Chiarenzelli and McLelland, 1991; Hamilton et al., 2004; McLelland and Selleck, 2011). The lower crust in the central Highlands at this time must have been weakened by anatexis and decompression melting, which would have helped drive buoyant exhumation of these high-grade rocks and facilitated significant (near-) isothermal decompression (Figs. 13, 15, 16; e.g., Rey et al., 2009; Vanderhaeghe, 2009).

A weak northeast-dipping foliation in the Ledge Mountain granulites (~10 km northeast of Snowy Mountain) shows they sit on the northern flank of the domal structure formed by Snowy Mountain (Fig. 1; Geraghty, 1978). The granulite-facies, sinistral Moose River Plain shear zone wraps around the Snowy Mountain dome then extends east toward Gore Mountain (but exposure is lost). Chiarenzelli et al. (2000), Gates et al. (2004), and Valentino et al. (2008) suggest that sinistral transpression along the Moose River Plain shear zone was in part responsible for exhumation of the anorthosite-cored Snowy Mountain dome. A similar concept is used to explain the evolution of migmatitic gneiss domes in the southern Karakoram (northwestern Himalaya, Pakistan), where molten middle crust was exhumed diapirically along vertical structures parallel to the crustal-scale Karakoram fault in the compressional regime of the Himalayan orogen (Mahéo et al., 2004).

Several large anorthosite bodies (Snowy Mountain, Oregon dome, and Humphrey Mountain) and the Gore Mountain amphibolite, along with subordinate Lyon Mountain Granite and the Ledge Mountain migmatites, lie broadly between the Moose River Plain shear zone to the north and the Piseco Lake shear zone (a crustal-scale sinistral shear zone) to the south. These high-grade rocks represent exhumed lower crust that also follows the structural grain of large-scale folds in the surrounding metasedimentary rocks (Fig. 2); together, they may form a second large gneiss dome (like the Marcy massif) that exhumed during the extensional phase of the Ottawan orogeny. The relationship of this proposed second dome to the Marcy massif is uncertain. These could be separate domes or, alternately, could represent a double dome structure like Montagne Noire in the French Massif Central or the Naxos dome (Cyclades Islands, Greece) where two sub-domes are separated by a near-vertical high-strain zone (Fig. 2; Rey et al., 2011; Whitney et al., 2020). If the latter, it will be important to locate and document a high-strain zone between Ledge Mountain and the Marcy massif as well as the domal foliation that would necessarily surround this south-central region of the Highlands (Figs. 1, 2).

## Comparison with Thermomechanical Models and Other Collisional Orogens

The inferred peak mineral assemblage for Ledge Mountain migmatites (plagioclase + K-feldspar + quartz + garnet + sillimanite + rutile + melt) is found in other collisional orogens including the Bohemian massif of the Variscan orogen (e.g., O'Brien, 2008; Kotková and Harley, 2010) and, if kyanite is present, is widely considered to reflect minimum *P-T* conditions of 14 kbar at 920 °C (e.g., O'Brien, 2008). This is consistent with our modeling results (assuming kyanite is present) and suggests there may be other petrotectonic similarities between the Grenville and Variscan orogens (Fig. 16B).

The definitive Antarctic UHT granulite-facies terranes follow isothermal decompression paths that could fit our exhumation model for Ledge Mountain (Figs. 16B, 16C; Harley, 2004, 2008). The Eastern Ghats region of India contains petrologically similar rocks to Ledge Mountain (i.e., felsic) and yields *P-T*

estimates that are similar to those of the Antarctic terranes (Korhonen et al., 2011; Kelsey et al., 2017).

Several authors have noted the temporal association of UHT metamorphism with supercontinent assembly (e.g., Santosh et al., 2011; Touret et al., 2016), and according to Harley (2016), the large hot orogen model, which is widely applied to the Grenville orogeny (e.g., Rivers, 2008, 2009, 2015), provides the best explanation for prolonged UHT metamorphism and associated clockwise *P-T* paths similar to those reported here for the Ledge Mountain granulites. The thermo-mechanical model of Jamieson and Beaumont (2010) for Grenville-style lower crustal flow is similar to our estimated *P-T* path, but the mid-crust represented by modeled Greater Himalayan Sequence rocks (Jamieson et al., 2004; O'Brien, 2008) does not achieve UHT conditions (Fig. 16C). Ledge Mountain granulites must represent deeper, hotter lower crust compared to Greater Himalayan Sequence rocks, consistent with our modeled peak metamorphic *P-T* conditions.

## CONCLUSIONS

Isochemical phase equilibrium modeling combined with microtextural analysis and mineral composition data have revealed more extreme metamorphic *P-T* conditions than previously recognized in the central Adirondack Highlands based on conventional thermobarometry. We estimate minimum metamorphic *P-T* conditions of 960–1025 °C and 11–12.5 kbar, which is comparable to conditions of other UHT granulite terranes like those from Antarctica, Eastern Ghats (India), and the Khondalite belt (North China craton) (Figs. 16B, 16C). Our results demonstrate that pseudosection modeling, combined with Ca-in-garnet isopleth models, can be used to recognize UHT metamorphism in felsic granulites that lack diagnostic UHT mineral assemblages such as sapphirine + quartz or orthopyroxene + sillimanite ± quartz (Kelsey and Hand, 2015; Li et al., 2019).

Ledge Mountain migmatites are dry; we estimate 0.12 wt% $H_2O$ based on their biotite content. We tested increasing water contents and found that modeled metamorphic temperatures decreased by ~50–100 °C per weight percent $H_2O$. Models required >3 wt% $H_2O$—25 times our best estimate using the biotite content—to shift the peak field to <900 °C (i.e., sub-UHT conditions).

Ultrahigh-temperature metamorphism is now recognized for two localities in the central Adirondack Highlands—at Ledge Mountain and Gore Mountain—which has important implications for late- to post-orogenic crustal dynamics in the Grenville province. These results suggest a need for wider application of thermodynamic modeling in the Grenville province and in other orogens worldwide. UHT conditions may occur on a regional scale or may be quite localized, including adjacent to anorthosite or mafic intrusions (Kelsey and Hand, 2015, and references therein). Recognition of UHT metamorphic conditions at Ledge Mountain suggests additional effort should be made to identify UHT conditions elsewhere in the (central) Adirondack Highlands because if UHT conditions were more widespread, the significant amount of melt in the middle or lower crust would have important implications for Grenville tectonics.

New U-Pb zircon data establish an Ottawan age for the metamorphism and anatexis recorded in felsic granulites, which are thought to represent partial melting of older plutonic rocks based on whole-rock chemistry and zircon trace element data. UHT metamorphism and the presence of at least ~15%–30% melt based on thermodynamic modeling are compatible with melt-assisted exhumation of deep-crustal migmatites in a late-orogenic extensional dome.

### ACKNOWLEDGMENTS

The authors want to thank Gary M. Boone (Emeritus Professor, Syracuse University) for his inspiration, guidance, and long-lasting drive for answers in the Adirondack Highlands. We are grateful to Marion E. (Pat) Bickford (Syracuse University) for facilitating collection and processing of samples for age dating. Former San Jose State University graduate student Susan Gervais Scudder assisted with electron microprobe analysis and petrographic descriptions. Extensive comments from Michael Williams and two anonymous reviewers greatly improved this manuscript, and we also thank Mark Quigley, Toby Rivers, and two anonymous reviewers for their feedback on an earlier version of this paper. We owe Matt Coble many thanks for his guidance in the USGS-Stanford SHRIMP-RG Lab and for the teaching and mentoring of our students who have passed through that lab. We would also like to acknowledge Dale Burns in the Stanford Microchemical Analysis Facility for his expert assistance.

### REFERENCES CITED

Aleinikoff, J.N., Walsh, G.J., 2017. New evidence for late to post-Shawinigan intrusion of the Hawkeye Granite Gneiss and Lyon Mountain Granite Gneiss, Adirondack Highlands. NY: Geological Society of America, Abstracts with Programs, v. 49, https://doi.org/10.1130/abs/2017NE-290044.

Baird, G.B., 2020, Late Ottawan orogenic collapse of the Adirondacks in the Grenville province of New York State (USA): Integrated petrologic, geochronologic, and structural analysis of the Diana Complex in the southern Carthage-Colton mylonite zone: Geosphere, v. 16, p. 844–874, https://doi.org/10.1130/GES02155.1.

Baldwin, J.A., Brown, M., and Schmitz, M.D., 2007, First application of titanium-in-zircon thermometry to ultrahigh-temperature metamorphism: Geology, v. 35, p. 295–298, https://doi.org/10.1130/G23285A.1.

Barker, F., 1979, Trondhjemites: Definition, environment and hypotheses of origin, *in* Barker, F., ed., Trondhjemites, Dacites and Related Rocks: Amsterdam, Elsevier, p. 1–12, https://doi.org/10.1016/B978-0-444-41765-7.50006-X.

Bartoli, O., 2017, Phase equilibria modelling of residual migmatites and granulites: An evaluation of the melt-reintegration approach: Journal of Metamorphic Geology, v. 35, p. 919–942, https://doi.org/10.1111/jmg.12261.

Bartoli, O., Acosta-Vigil, A., and Cesare, B., 2015, High-temperature metamorphism and crustal melting: Working with melt inclusions: Periodico di Mineralogia, v. 84, p. 591–614, https://doi.org/10.2451/2015PM0434.

Bartoli, O., Acosta-Vigil, A., Ferrero, S., and Cesare, B., 2016, Granitoid magmas preserved as melt inclusions in high-grade metamorphic rock: American Mineralogist, v. 101, p. 1543–1559, https://doi.org/10.2138/am-2016-5541CCBYNCND.

Bickford, M.E., McLelland, J.M., Selleck, B.W., Hill, B.M., and Heumann, M.J., 2008, Timing of anatexis in the eastern Adirondack Highlands: Implications for tectonic evolution during ca. 1050 Ma Ottawan orogenesis: Geological Society of America Bulletin, v. 120, p. 950–961, https://doi.org/10.1130/B26309.1.

Bingen, B., Austrheim, H., and Whitehouse, M., 2001, Ilmenite as a source for zirconium during high-grade metamorphism? Textural evidence from the Caledonides of western Norway and implications for zircon: Journal of Petrology, v. 42, p. 355–375, https://doi.org/10.1093/petrology/42.2.355.

Bohlen, S.R., 1987, Pressure-temperature-time paths and a tectonic model for the evolution of granulites: The Journal of Geology, v. 95, p. 617–632, https://doi.org/10.1086/629159.

Bohlen, S.R., and Essene, E.J., 1977, Feldspar and oxide thermometry of granulites in the Adirondack Highlands: Contributions to Mineralogy and Petrology, v. 62, p. 153–169, https://doi.org/10.1007/BF00372874.

Bohlen, S.R., Essene, E.J., and Hoffman, K.S., 1980, Update on feldspar and oxide thermometry in the Adirondack Mountains, New York: Geological Society of America Bulletin, v. 91, p. 110–113, https://doi.org/10.1130/0016-7606(1980)91<110:UOFAOT>2.0.CO;2.

Bohlen, S.R., Valley, J.W., and Essene, E.J., 1985, Metamorphism in the Adirondacks: I. Petrology, pressure and temperature: Journal of Petrology, v. 26, p. 971–992, https://doi.org/10.1093/petrology/26.4.971.

Boone, G.M., 1978, Kyanite in Adirondack Highlands sillimanite-rich gneiss, and *P-T* estimates of metamorphism: Geological

Society of America Abstracts with Programs, v. 10, no. 2, p. 34.
Bose, S., Das, K., Ohnishi, I., Torimoto, J., Karmakar, S., Shinoda, K., and Dasgupta, S., 2009, Characterization of oxide assemblages of a suite of granulites from Eastern Ghats Belt, India: Implication to the evolution of C-O-H-F fluids during retrogression: Lithos, v. 113, p. 483–497, https://doi.org/10.1016/j.lithos.2009.05.029.
Brown, M., 2014, The contribution of metamorphic petrology to understanding lithosphere evolution and geodynamics: Geoscience Frontiers, v. 5, no. 4, p. 553–569, https://doi.org/10.1016/j.gsf.2014.02.005.
Carswell, D.A., and O'Brien, P.J., 1993, Thermobarometry and geotectonic significance of high-pressure granulites: Examples from the Moldanubian Zone of the Bohemian Massif in Lower Austria: Journal of Petrology, v. 34, p. 427–459, https://doi.org/10.1093/petrology/34.3.427.
Cesare, B., Acosta-Vigil, A., Bartoli, O., and Ferrero, S., 2015, What can we learn from melt inclusions in migmatites and granulites?: Lithos, v. 239, p. 186–216, https://doi.org/10.1016/j.lithos.2015.09.028.
Chakraborty, S., and Ganguly, J., 1992, Cation diffusion in aluminosilicate garnets: Experimental determination in spessartine-almandine diffusion couples, evaluation of effective binary diffusion coefficients, and applications: Contributions to Mineralogy and Petrology, v. 111, p. 74–86, https://doi.org/10.1007/BF00296579.
Cherniak, D.J., and Watson, E.B., 2003, Diffusion in zircon: Reviews in Mineralogy and Geochemistry, v. 53, p. 113–143, https://doi.org/10.2113/0530113.
Chiarenzelli, J.R., and McLelland, J.M., 1991, Age and regional relationships of granitoid rocks of the Adirondack Highlands: The Journal of Geology, v. 99, p. 571–590, https://doi.org/10.1086/629518.
Chiarenzelli, J., Valentino, D., and Gates, A., 2000, Sinistral transpression in the Adirondack Highlands during the Ottawan Orogeny: Strike-slip faulting in the deep Grenvillian crust: Abstract, Calgary, Alberta, Millenium Geoscience Summit GeoCanada 2000.
Chiarenzelli, J., Regan, S., Peck, W.H., Selleck, B.W., Cousens, B, Baird, G.B., and Shrady, C.H., 2010, Shawinigan arc magmatism in the Adirondack Lowlands as a consequence of closure of the Trans-Adirondack backarc basin: Geosphere, v. 6, p. 900–916, https://doi.org/10.1130/GES00576.1.
Chiarenzelli, J., Selleck, B., Lupulescu, M., Regan, S., Bickford, M.E., Valley, P., and McLelland, J., 2017, Lyon Mountain ferroan leucogranite suite: Magmatic response to extensional thinning of overthickened crust in the core of the Grenville orogen: Geological Society of America Bulletin, v. 129, p. 1472–1488, https://doi.org/10.1130/B31697.1.
Clark, C., Taylor, R.J.M., Johnson, T.E., Harley, S.L., Fitzsimmons, I.C.W., and Oliver, L., 2019, Testing the fidelity of thermometers at ultrahigh temperatures: Journal of Metamorphic Geology, v. 37, p. 917–934, https://doi.org/10.1111/jmg.12486.
Connelly, J.N., 2006, Improved dissolution and chemical separation methods for Lu-Hf garnet chronometry: Geochemistry Geophysics Geosystems, v. 7, Q04005, https://doi.org/10.1029/2005GC001082.
Connolly, J.A.D., 2005, Computation of phase equilibria by linear programming: A tool for geodynamic modeling and its application to subduction zone decarbonation: Earth and Planetary Science Letters, v. 236, p. 524–541, https://doi.org/10.1016/j.epsl.2005.04.033.
Connolly, J.A.D., 2009, The geodynamic equation of state: What and how: Geochemistry Geophysics Geosystems, v. 10, Q10014, https://doi.org/10.1029/2009GC002540.
Cooke, R.A., 2000, High-pressure/temperature metamorphism in the St. Leonhard Granulite Massif, Austria: Evidence from intermediate pyroxene-bearing granulites: International Journal of Earth Sciences, v. 89, p. 631–651, https://doi.org/10.1007/s005310000123.
Corfu, F., Hanchar, J.M., Hoskin, P.W.O., and Kinny, P., 2003, Atlas of zircon textures: Reviews in Mineralogy and Geochemistry, v. 53, p. 469–500, https://doi.org/10.2113/0530469.
Darling, R.S., 2013, Zircon-bearing, crystallized melt inclusions in peritectic garnet from the western Adirondack Mountains, New York State, USA: Geofluids, v. 13, p. 453–459, https://doi.org/10.1111/gfl.12047.
Darling, R.S., and Peck, W.H., 2016, Metamorphic conditions of Adirondack rocks: Adirondack Journal of Environmental Studies, v. 21, p. 61–79.
Das, E., Karmakar, S., Dey, A., Karmakar, S., and Sengupta, P., 2017, Reaction textures, pressure-temperature paths and chemical dates of monazite from a new suite of sapphirine-spinel granulites from parts of the Eastern Ghats Province, India: Insights into the final amalgamation of India and East Antarctica during the formation of Rodinia, *in* Pant, N.C., and Dasgupta, S., eds., Crustal Evolution of India and Antarctica: The Supercontinent Connection: Geological Society of London Special Publication 457, p. 141–170, https://doi.org/10.1144/SP457.12.
Dasgupta, S., Sengupta, P., Ehl, J., Raith, M., and Bardhan, S., 1995, Reaction textures in a suite of spinel granulites from the Eastern Ghats Belt, India: Evidence for polymetamorphism, a partial petrogenetic grid in the system KFMASH and the roles of ZnO and $Fe_2O_3$: Journal of Petrology, v. 36, p. 435–461, https://doi.org/10.1093/petrology/36.2.435.
Ewing, T.A., Hermann, J., and Rubatto, D., 2013, The robustness of the Zr-in-rutile and Ti-in-zircon thermometers during high-temperature metamorphism (Ivrea-Verbano Zone, northern Italy): Contributions to Mineralogy and Petrology, v. 165, p. 757–779, https://doi.org/10.1007/s00410-012-0834-5.
Ferry, J.M., and Watson, E.B., 2007, New thermodynamic models and revised calibrations for the Ti-in-zircon and Zr-in-rutile thermometers: Contributions to Mineralogy and Petrology, v. 154, p. 429–437, https://doi.org/10.1007/s00410-007-0201-0.
Florence, F.P., and Spear, F.S., 1995, Intergranular diffusion kinetics of Fe and Mg during retrograde metamorphism of a pelitic gneiss from the Adirondack Mountains: Earth and Planetary Science Letters, v. 134, p. 329–340, https://doi.org/10.1016/0012-821X(95)00129-Z.
Frost, B.R., and Chacko, T., 1989, The granulite uncertainty principle: Limitations on thermobarometry in granulites: The Journal of Geology, v. 97, p. 435–450, https://doi.org/10.1086/629321.
Frost, B.R., and Frost, C.D., 2008, A geochemical classification for feldspathic igneous rocks: Journal of Petrology, v. 49, p. 1955–1969, https://doi.org/10.1093/petrology/egn054.
Frost, C.D., and Frost, B.R., 2011, On ferroan (A-type) granitoids: Their compositional variability and modes of origin: Journal of Petrology, v. 52, p. 39–53, https://doi.org/10.1093/petrology/egq070.
Frost, B.R., Barnes, C.G., Collins, W.J., Arculus, R.J., Ellis, D.J., and Frost, C.D., 2001, A geochemical classification for granitic rocks: Journal of Petrology, v. 42, p. 2033–2048, https://doi.org/10.1093/petrology/42.11.2033.
Fuhrman, M.L., and Lindsley, D.H., 1988, Ternary-feldspar modeling and thermometry: American Mineralogist, v. 73, p. 201–215.
Gates, A.E., Valentino, D.W., Chiarenzelli, J.R., Solar, G.S., and HamiltonI, M.A., 2004, Exhumed Himalayan-type syntaxis in the Grenville orogen, northeastern Laurentia: Journal of Geodynamics, v. 37, p. 337–359.
Geraghty, E.P., 1978, Structure, stratigraphy, and petrology of part of the Blue Mountain 15′ quadrangle, central Adirondack Mountains, New York [Ph.D. thesis]: Syracuse, New York, Syracuse University, 281 p.
Green, E.C.R., White, R.W., Diener, J.F.A., Powell, R., Holland, T.J.B., and Palin, R.M., 2016, Activity-composition relations for the calculation of partial melting equilibria in metabasic rocks: Journal of Metamorphic Geology, v. 39, p. 845–869, https://doi.org.jpllnet.sfsu.edu/10.1111/jmg.12211.
Groppo, C., Rolfo, F., and Indares, A., 2012, Partial melting in the Higher Himalayan Crystallines of eastern Nepal: The effect of decompression and implications for the 'channel flow' model: Journal of Petrology, v. 53, p. 1057–1088, https://doi.org/10.1093/petrology/egs009.
Guilmette, C., Indares, A., and Hébert, R., 2011, High-pressure anatectic paragneisses from the Namche Barwa, Eastern Himalayan Syntaxes: Textural evidence for partial melting, phase equilibria modeling and tectonic implications: Lithos, v. 124, p. 66–81, https://doi.org/10.1016/j.lithos.2010.09.003.
Hamilton, M.A., McLelland, J., and Selleck, B., 2004, SHRIMP U-Pb zircon geochronology of the anorthosite-mangerite-charnockite-granite suite, Adirondack Mountains, New York: Ages of emplacement and metamorphism, *in* Tollo, R.P., Corriveau, L., McLelland, J.M., and Bartholomew, M.J., eds., Proterozoic Tectonic Evolution of the Grenville Orogen in North America: Geological Society of America Memoir 197, p. 337–355, https://doi.org/10.1130/0-8137-1197-5.337.
Harley, S.L., 2004, Extending our understanding of ultrahigh temperature crustal metamorphism: Journal of Mineralogical and Petrological Sciences, v. 99, p. 140–158, https://doi.org/10.2465/jmps.99.140.
Harley, S.L., 2008, Refining the *P-T* records of UHT crustal metamorphism: Journal of Metamorphic Geology, v. 26, p. 125–154, https://doi.org/10.1111/j.1525-1314.2008.00765.x.
Harley, S.L., 2016, A matter of time: The importance of the duration of UHT metamorphism: Journal of Mineralogical and Petrological Sciences, v. 111, p. 50–72, https://doi.org/10.2465/jmps.160128.
Hasalová, P., Štípská, P., Powell, R., Schulmann, K., Janoušek, V., and Lexa, O., 2007, Transforming mylonitic metagranite by open-system interactions during melt flow: Journal of Metamorphic Geology, v. 26, p. 55–80, https://doi.org/10.1111/j.1525-1314.2007.00744.x.
Hasterok, D., Gard, M., Bishop, C.M.B., and Kelsey, D., 2019, Chemical identification of metamorphic protoliths using machine learning methods: Computers & Geosciences, v. 132, p. 56–68, https://doi.org/10.1016/j.cageo.2019.07.004.
Heumann, M.J., Bickford, M.E., Hill, B.M., McLelland, J.M., Selleck, B.W., and Jercinovic, M.J., 2006, Timing of anatexis in metapelites from the Adirondack lowlands and southern highlands: A manifestation of the Shawinigan orogeny and subsequent anorthosite-mangerite-charnockite-granite

magmatism: Geological Society of America Bulletin, v. 118, p. 1283–1298, https://doi.org/10.1130/B25927.1.

Holland, T., and Powell, R., 1991, A compensated-Redlich-Kwong (CORK) equation for volumes and fugacities of $CO_2$ and $H_2O$ in the range 1 bar to 50 kbar and 100–1600°C: Contributions to Mineralogy and Petrology, v. 109, p. 265–273, https://doi.org/10.1007/BF00306484.

Holland, T., and Powell, R., 2001, Calculation of phase relations involving haplogranitic melts using an internally consistent thermodynamic dataset: Journal of Petrology, v. 42, p. 673–683, https://doi.org/10.1093/petrology/42.4.673.

Holland, T.J.B., and Powell, R., 2011, An improved and extended internally consistent thermodynamic dataset for phases of petrological interest, involving a new equation of state for solids: Journal of Metamorphic Geology, v. 29, p. 333–383, https://doi.org/10.1111/j.1525-1314.2010.00923.x.

Holland, T.J.B., Green, E.C.R., and Powell, R., 2018, Melting of peridotite through to granites: A simple thermodynamic model in the system KNCFMASHTOCr: Journal of Petrology, v. 59, p. 881–900, https://doi.org/10.1093/petrology/egy048.

Hollis, J.A., Harley, S.L., White, R.W., and Clarke, G.L., 2006, Preservation of evidence for prograde metamorphism in ultra-high-temperature, high-pressure kyanite-bearing granulites, South Harris, Scotland: Journal of Metamorphic Geology, v. 24, p. 263–279, https://doi.org/10.1111/j.1525-1314.2006.00636.x.

Holness, M.B., and Sawyer, E.W., 2008, On the pseudomorphing of melt-filled pores during the crystallization of migmatites: Journal of Petrology, v. 49, p. 1343–1363, https://doi.org/10.1093/petrology/egn028.

Holness, M.B., Cesare, B., and Sawyer, E.W., 2011, Melted rocks under the microscope: Microstructures and their interpretation: Elements, v. 7, p. 247–252, https://doi.org/10.2113/gselements.7.4.247.

Holtz, F., Jannes, W., Tamic, N., and Behrens, H., 2001, Maximum and minimum water contents of granitic melts generated in the crust: A reevaluation and implications: Lithos, v. 56, p. 1–14, https://doi.org/10.1016/S0024-4937(00)00056-6.

Hoskin, P.W.O., and Schaltegger, U., 2003, The composition of zircon and igneous and metamorphic petrogenesis: Reviews in Mineralogy and Geochemistry, v. 53, p. 27–62, https://doi.org/10.2113/0530027.

Huang, W.-L., and Wyllie, P.J., 1975, Melting reactions in the system $NaAlSi_3O_8$—$KAlSi_3O_8$—$SiO_2$ to 35 kilobars, dry and with excess water: The Journal of Geology, v. 83, p. 737–748, https://doi.org/10.1086/628165.

Indares, A., 2020, Deciphering the metamorphic architecture and magmatic patterns of large hot orogens: Insights from the central Grenville Province: Gondwana Research, v. 80, p. 385–409, https://doi.org/10.1016/j.gr.2019.10.013.

Indares, A., White, R.W., and Powell, R., 2008, Phase equilibria modelling of kyanite-bearing anatectic paragneisses from the central Grenville Province: Journal of Metamorphic Geology, v. 26, p. 815–836, https://doi.org/10.1111/j.1525-1314.2008.00788.x.

Jamieson, R.A., and Beaumont, C., 2010, Coeval thrusting and extension during lower crustal ductile flow—Implications for exhumation of high-grade metamorphic rocks: Journal of Metamorphic Geology, v. 29, p. 33–51, https://doi.org/10.1111/j.1525-1314.2010.00908.x.

Jamieson, R.A., Beaumont, C., Medvedev, S., and Nguyen, M.H., 2004, Crustal channel flows: 2. Numerical models with implications for metamorphism in the Himalayan-Tibetan orogen: Journal of Geophysical Research, v. 109, B06407, https://doi.org/10.1029/2003JB002811.

Jamieson, R.A., Beaumont, C., Nguyen, M.H., and Culshaw, 2007, Synconvergent ductile flow in variable-strength continental crust: Numerical models with application to the western Grenville orogen: Tectonics, v. 26, TC5005, https://doi.org/10.1029/2006TC002036.

Janoušek, V., Finger, F., Roberts, M., Frýda, J., Pin, C., and Dolejš, D., 2004, Deciphering the petrogenesis of deeply buried granites: Whole-rock geochemical constraints on the origin of largely undepleted felsic granulites from the Moldanubian Zone of the Bohemian Massif: Transactions of the Royal Society of Edinburgh: Earth Sciences, v. 95, p. 141–159, https://doi.org/10.1017/S0263593300000985.

Johannes, W., and Holtz, F., 1996, Petrogenesis and Experimental Petrology of Granitic Rocks: Berlin, Springer-Verlag, Minerals and Rocks Series, v. 22, 335 p., https://doi.org/10.1007/978-3-642-61049-3.

Johnson, D.M., Hooper, P.R., and Conrey, R.M., 1999, XRF analysis of rocks and minerals for major and trace elements on a single low dilution Li-tetraborate bead: Advances in X-ray Analysis, v. 41, p. 843–867.

Kelsey, D.E., and Hand, M., 2015, On ultrahigh temperature crustal metamorphism: Phase equilibria, trace element thermometry, bulk composition, heat sources, timescales and tectonic settings: Geoscience Frontiers, v. 6, p. 311–356, https://doi.org/10.1016/j.gsf.2014.09.006.

Kelsey, D.E., and Powell, R., 2011, Progress in linking accessory mineral growth and breakdown to major mineral evolution in metamorphic rocks: A thermodynamic approach in the $Na_2O$-CaO-$K_2O$-FeO-MgO-$Al_2O_3$-$SiO_2$-$H_2O$-$TiO_2$-$ZrO_2$ system: Journal of Metamorphic Geology, v. 29, p. 151–166, https://doi.org/10.1111/j.1525-1314.2010.00910.x.

Kelsey, D.E., Clark, C., and Hand, M., 2008, Thermobarometric modelling of zircon and monazite growth in melt-bearing systems: Examples using model metapelitic and metapsammitic granulites: Journal of Metamorphic Geology, v. 26, p. 199–212, https://doi.org/10.1111/j.1525-1314.2007.00757.x.

Kelsey, D.E., Morrissey, L.J., Hand, M., Clark, C., Tamblyn, R., Gaehl, A.A., and Marshall, S., 2017, Significance of post-peak metamorphic reaction microstructures in the ultrahigh temperature Eastern Ghats Province, India: Journal of Metamorphic Geology, v. 35, p. 1081–1109, https://doi.org/10.1111/jmg.12277.

Kendrick, J., and Indares, A., 2018, The reaction history of kyanite in high-*P* aluminous granulites: Journal of Metamorphic Geology, v. 36, p. 125–146, https://doi.org/10.1111/jmg.12286.

Kohn, M.J., Corrie, S.L., and Markley, C., 2015, The fall and rise of metamorphic zircon: American Mineralogist, v. 100, p. 897–908, https://doi.org/10.2138/am-2015-5064.

Korhonen, F.J., Saw, A.K., Clark, C., Brown, M., and Bhattacharya, S., 2011, New constraints on UHT metamorphism in the Eastern Ghats Province through the application of phase equilibria modeling and in situ geochronology: Gondwana Research, v. 20, p. 764–781, https://doi.org/10.1016/j.gr.2011.05.006.

Kotková, J., and Harley, S.L, 2010, Anatexis during high-pressure crustal metamorphism: Evidence from garnet–whole-rock REE relationships and zircon-rutile Ti-Zr thermometry in leucogranulites from the Bohemian Massif: Journal of Petrology, v. 51, p. 1967–2001, https://doi.org/10.1093/petrology/egq045.

Lasalle, S., and Indares, A., 2014, Anatectic record and contrasting *P-T* paths of aluminous gneisses from the central Grenville Province: Journal of Metamorphic Geology, v. 32, p. 627–646, https://doi.org/10.1111/jmg.12083.

Lechler, P.J., and Desilets, M.O., 1987, A review of the use of loss on ignition as a measurement of total volatiles in whole-rock analysis: Chemical Geology, v. 63, p. 341–344, https://doi.org/10.1016/0009-2541(87)90171-9.

Li, X., White, R.W., and Wei, C., 2019, Can we extract ultra-high-temperature conditions from Fe-rich metapelites? An example from the Khondalite Belt, North China Craton: Lithos, v. 328, p. 228–243, https://doi.org/10.1016/j.lithos.2019.01.032.

Mahéo, G., Pêcher, A., Guillot, S., Rolland, Y., and Delacourt, C., 2004, Exhumation of Neogene gneiss domes between oblique crustal boundaries in south Karakorum (northwest Himalaya, Pakistan), *in* Whitney, D.L., Teyssier, C., and Siddoway, C.S., eds., Gneiss Domes in Orogeny: Geological Society of America Special Paper 380, p. 141–154, https://doi.org/10.1130/0-8137-2380-9.141.

Maniar, P.O., and Piccoli, P.M., 1989, Tectonic discrimination of granitoids: Geological Society of America Bulletin, v. 101, p. 635–643, https://doi.org/10.1130/0016-7606(1989)101<0635:TDOG>2.3.CO.

McDonough, W.F. and Sun, S.S., 1995, The composition of the Earth: Chemical Geology, v. 120, p. 223–253.

McLelland, J., 1991, Geology and geochronology of the southern Adirondacks, *in* Ebert, J.R., ed., Field Trip Guidebook: New York State Geological Association 63rd Annual Meeting, Guidebook, p. 71–101.

McLelland, J., and Isachsen, Y., 1980, Structural synthesis of the southern and central Adirondacks: A model for the Adirondacks as a whole and plate-tectonics interpretation: Geological Society of America Bulletin, v. 91, p. 208–292, https://doi.org/10.1130/GSAB-P2-91-208.

McLelland, J., Morrison, J., Selleck, B., Cunningham, B., Olson, C., and Schmidt, K., 2002, Hydrothermal alteration of late- to post-tectonic Lyon Mountain granitic gneiss, Adirondack Mountains, New York: Origin of quartz-sillimanite segregations, quartz-albite lithologies, and associated Kiruna-type low-Ti Fe-oxide deposits: Journal of Metamorphic Geology, v. 20, p. 175–190, https://doi.org/10.1046/j.0263-4929.2001.00345.x.

McLelland, J.M., and Selleck, B.W., 2011, Megacrystic Gore Mountain–type garnets in the Adirondack Highlands: Age, origin, and tectonic implications: Geosphere, v. 7, p. 1194–1208, https://doi.org/10.1130/GES00683.1.

McLelland, J.M., Geraghty, E., and Boone, G.M., 1978, The structural framework and petrology of the southern Adirondacks, *in* Merriam, D.F., ed., New York State Geological Association 50th Annual Meeting Guidebook: Syracuse, NewYork, Syracuse University Department of Geology, p. 58–103.

McLelland, J.M., Bickford, M.E., Hill, B.M., Clechenko, C.C., Valley, J.W., and Hamilton, M.A., 2004, Direct dating of Adirondack massif anorthosite by U-Pb SHRIMP analysis of igneous zircon: Implications for AMCG complexes: Geological Society of America Bulletin, v. 116, p. 1299-1317, https://doi.org/10.1130/B25482.1.

McLelland, J.M., Selleck, B.W., and Bickford, M.E., 2010, Review of the Proterozoic evolution of the Grenville Province, its Adirondack outlier, and the Mesoproterozoic inliers of the

Appalachians, *in* Tollo, R.P., Bartholomew, M.J., Hibbard, J.P., and Karabinos, P.M., eds., From Rodinia to Pangea: The Lithotectonic Record of the Appalachian Region: Geological Society of America Memoir 206, p. 21–49, https://doi.org/10.1130/2010.1206(02).

McLelland, J.M., Selleck, B.W., and Bickford, M.E., 2013, Tectonic evolution of the Adirondack Mountains and Grenville Orogen inliers within the USA: Geoscience Canada, v. 40, p. 318–352, https://doi.org/10.12789/geocanj.2013.40.022.

Metzger, E.P., 1980, Investigation of partial melting at Ledge Mountain, central Adirondacks, New York [M.S. thesis]: Syracuse, New York, Syracuse University, 105 p.

Nicholls, I.A., and Ringwood, A.E., 1973, Effect of water on olivine stability in tholeiites and the production of silica-saturated magmas in the island-arc environment: The Journal of Geology, v. 81, p. 285–300, https://doi.org/10.1086/627871.

O'Brien, P.J., 2008, Challenges in high-pressure granulite metamorphism in the era of pseudosections: Reaction textures, compositional zoning and tectonic interpretation with examples from the Bohemian Massif: Journal of Metamorphic Geology, v. 26, p. 235–251, https://doi.org/10.1111/j.1525-1314.2007.00758.x.

Ownby, S.E., Miller, C.F., Berquist, P.J., Carrigan, C.W., Wooden, J.L., and Fullagar, P.D., 2004, U-Pb geochronology and geochemistry of a portion of the Mars Hill terrane, North Carolina–Tennessee: Constraints on origin, history, and tectonic assembly, *in* Tollo, R.P., Corriveau, L., McLelland, J., and Bartholemew, M.J., eds., Proterozoic Tectonic Evolution of the Grenville Orogen in North America: Geological Society of America Memoir 197, p. 609–632, https://doi.org/10.1130/0-8137-1197-5.609.

Pearce, J.A., Harris, N.B., and Tindle, A.G., 1984, Trace element discrimination diagrams for the tectonic interpretation of granitic rocks: Journal of Petrology, v. 25, p. 956–983, https://doi.org/10.1093/petrology/25.4.956.

Peck, W.H., Selleck, B.W., Wong, M.S., Chiarenzelli, J.R., Harpp, K.S., Hollocher, K., Lackey, J.S., Catalano, J., Regan, S.P., and Stocker, A., 2013, Orogenic to postorogenic (1.20–1.15 Ga) magmatism in the Adirondack Lowlands and Frontenac terrane, southern Grenville Province, USA and Canada: Geosphere, v. 9, p. 1637–1663, https://doi.org/10.1130/GES00879.1.

Peck, W.H., Selleck, B.W., Regan, S.P., Howard, G.E., and Kozel, O.O., 2018, In-situ dating of metamorphism in Adirondack anorthosite: American Mineralogist, v. 103, p. 1523–1529. https://doi.org/10.2138/am-2018-6481.

Pownall, J.M., 2015, UHT metamorphism on Seram, eastern Indonesia: Reaction microstructures and *P-T* evolution of spinel-bearing garnet-sillimanite granulites from the Kobipoto Complex: Journal of Metamorphic Geology, v. 33, p. 909–935, https://doi.org/10.1111/jmg.12153.

Reeder, J.V., 2017, Formation of kyanite-bearing migmatites in the central Adirondacks [M.S. thesis]: San Francisco, California, San Francisco State University, 96 p.

Regan, S.P., Geer, P.S., Walsh, G.J., Aleinikoff, J.N., Baird, G.B., Valley, P.M., Williams, M.L., Jercinovic, M.J., and Grover, T.W., 2015, Precambrian geology of the Eagle Lake quadrangle, Essex County, New York, *in* Valentino, D., Roden-Tice, M.K., and Franzi, D., eds., Geology of the Northeastern Adirondack Mountains and Champlain-St. Lawrence Lowlands of New York, Vermont and Quebec: New York State Geological Association Field Conference field trip, 87th Annual Meeting, Plattsburgh, New York, 12–13 September, p. 30–59.

Regan, S.P., Walsh, G.J., Williams, M.L., Chiarenzelli, J.R., Toft, M., and McAleer, R., 2019, Syn-collisional exhumation of hot middle crust in the Adirondack Mountains (New York, USA): Implications for extensional orogenesis in the southern Grenville province: Geosphere, v. 15, p. 1240–1261, https://doi.org/10.1130/GES02029.1.

Rey, P.F., Teyssier, C., and Whitney, D.L., 2009, The role of partial melting and extensional strain rates in the development of metamorphic core complexes: Tectonophysics, v. 477, p. 135–144, https://doi.org/10.1016/j.tecto.2009.03.010.

Rey, P.F., Teyssier, C., Kruckenberg, S.C., and Whitney, D.L., 2011, Viscous collision in channel explains double domes in metamorphic core complexes: Geology, v. 39, p. 387–390, https://doi.org/10.1130/G31587.1.

Rivers, T., 1997, Lithotectonic elements of the Grenville Province: Review and tectonic implications: Precambrian Research, v. 86, p. 117–154, https://doi.org/10.1016/S0301-9268(97)00038-7.

Rivers, T., 2008, Assembly and preservation of lower, mid, and upper orogenic crust in the Grenville Province—Implications for the evolution of large hot long-duration orogens: Precambrian Research, v. 167, p. 237–259, https://doi.org/10.1016/j.precamres.2008.08.005.

Rivers, T., 2009, The Grenville Province as a large hot long-duration collisional orogen—Insights from the spatial and thermal evolution of its orogenic fronts, *in* Murphy, J.B., Keppie, J.D., and Hynes, A.J., eds., Ancient Orogens and Modern Analogues: Geological Society of London Special Publication 327, p. 405–444, https://doi.org/10.1144/SP327.17.

Rivers, T., 2012, Upper-crustal orogenic lid and mid-crustal core complexes: Signature of a collapsed orogenic plateau in the hinterland of the Grenville Province: Canadian Journal of Earth Sciences, v. 49, p. 1–42, https://doi.org/10.1139/e11-014.

Rivers, T., 2015, Tectonic setting and evolution of the Grenville Orogen: An assessment of progress over the last 40 years: Geoscience Canada, v. 42, p. 77–124, https://doi.org/10.12789/geocanj.2014.41.057.

Roberts, M.P., and Finger, F., 1997, Do U-Pb zircon ages from granulites reflect peak metamorphic conditions?: Geology, v. 25, p. 319–322, https://doi.org/10.1130/0091-7613(1997)025<0319:DUPZAF>2.3.CO;2.

Rosenberg, C.L., and Handy, M.R., 2005, Experimental deformation of partially melted granite revisited: Implications for the continental crust: Journal of Metamorphic Geology, v. 23, p. 19–28, https://doi.org/10.1111/j.1525-1314.2005.00555.x.

Rubatto, D., 2002, Zircon trace element geochemistry: Partitioning with garnet and the link between U-Pb ages and metamorphism: Chemical Geology, v. 184, p. 123–138, https://doi.org/10.1016/S0009-2541(01)00355-2.

Rubatto, D., 2017, Zircon: The metamorphic mineral: Reviews in Mineralogy and Geochemistry, v. 83, p. 261–295, https://doi.org/10.2138/rmg.2017.83.9.

Rubatto, D., and Gebauer, D., 2000, Use of cathodoluminescence for U-Pb zircon dating by ion microprobe: Some examples from the western Alps, *in* Pagel, M., Barbin, V., Blanc, P., and Ohnenstetter, D., eds., Cathodoluminescence in Geosciences: Berlin, Heidelberg, Springer, p. 373–400, https://doi.org/10.1007/978-3-662-04086-7_15.

Santosh, M., Kusky, T., and Wang, L., 2011, Supercontinent cycles, extreme metamorphic processes, and changing fluid regimes: International Geology Review, v. 53, p. 1403–1423, https://doi.org/10.1080/00206814.2010.527682.

Sarkar, T., and Schenk, V., 2014, Two-stage granulite formation in a Proterozoic magmatic arc (Ongole domain of the Eastern Ghats Belt, India): Part 1. Petrology and pressure-temperature evolution: Precambrian Research, v. 255, p. 485–509, https://doi.org/10.1016/j.precamres.2014.07.026.

Sawyer, E.W., 2008, Atlas of Migmatites: The Canadian Mineralogist Special Publication 9, 371 p.

Sawyer, E.W., Cesare, B., and Brown, M., 2011, When the continental crust melts: Elements, v. 7, p. 229–234, https://doi.org/10.2113/gselements.7.4.229.

Schaltegger, U., Fanning, C.M., Günther, D., Maurin, J.C., Schulmann, K., and Gebauer, D., 1999, Growth, annealing and recrystallization of zircon and preservation of monazite in high-grade metamorphism: Conventional and in-situ U-Pb isotope, cathodoluminescence and microchemical evidence: Contributions to Mineralogy and Petrology, v. 134, p. 186–201, https://doi.org/10.1007/s004100050478.

Schiller, D., and Finger, F., 2019, Application of Ti-in-zircon thermometry to granite studies: problems and possible solutions: Contributions to Mineralogy and Petrology, v. 174, https://doi.org/10.1007/s00410-019-1585-3.

Selleck, B.W., McLelland, J.M., and Bickford, M.E., 2005, Granite emplacement during tectonic exhumation: The Adirondack example: Geology, v. 33, p. 781–784, https://doi.org/10.1130/G21631.1.

Sengupta, P., Sen, J., Dasgupta, S., Raith, M., Bhui, U.K., and Ehl, J., 1999, Ultra-high temperature metamorphism of metapelitic granulites from Kondapalle, Eastern Ghats Belt: Implications for the Indo-Antarctic correlation: Journal of Petrology, v. 40, p. 1065–1087, https://doi.org/10.1093/petroj/40.7.1065.

Shinevar, W.J., Jagoutz, O., and VanTongeren, J.A., 2021, Gore Mountain garnet amphibolite records UHT conditions: Implications for the rheology of the lower continental crust during orogenesis: Journal of Petrology, egab007, https://doi.org/10.1093/petrology/egab007.

Spear, F.S., and Florence, F.P., 1992, Thermobarometry in granulites: Pitfalls and new approaches: Precambrian Research, v. 55, p. 209–241, https://doi.org/10.1016/0301-9268(92)90025-J.

Spear, F.S., and Markussen, J.C., 1997, Mineral zoning, *P-T-X-M* phase relations, and metamorphic evolution of some Adirondack granulites, New York: Journal of Petrology, v. 38, p. 757–783, https://doi.org/10.1093/petroj/38.6.757.

Storm, L.C., and Spear, F.S., 2005, Pressure, temperature and cooling rates of granulite facies migmatitic pelites from the southern Adirondack Highlands, New York: Journal of Metamorphic Geology, v. 23, p. 107–130, https://doi.org/10.1111/j.1525-1314.2005.00565.x.

Sun, S.-s., and McDonough, W.F., 1989, Chemical and isotopic systematics of oceanic basalts: Implications for mantle composition and processes, *in* Saunders, A.D., and Norry, M.J., eds., Magmatism in the Ocean Basins: Geological Society of London Special Publication 42, p. 313–345, https://doi.org/10.1144/GSL.SP.1989.042.01.19.

Swanson, B.A., 2019, Pressure-temperature conditions of kyanite-bearing migmatites at Ledge Mountain, central Adirondack Highlands [M.S. thesis]: San Francisco, California, San Francisco State University, 89 p.

Touret, J.L.R., Santosh, M., and Huizenga, J.M., 2016, High-temperature granulites and supercontinents: Geoscience Frontiers, v. 7, p. 101–113, https://doi.org/10.1016/j.gsf.2015.09.001.

Tsunogae, T., Santosh, M., Osanai, Y., Owada, M., Toyoshima, T., and Hokada, T., 2002, Very high-density carbonic fluid inclusions in sapphirine-bearing granulites from Tonagh Island in the Archean Napier Complex, East Antarctica: Implications for $CO_2$ infiltration during ultrahigh-temperature (T>1,100 °C) metamorphism: Contributions to Mineralogy and Petrology, v. 143, p. 279–299, https://doi.org/10.1007/s00410-001-0343-4.

Turpin, L., Cuney, M., Friedrich, M., Bouchez, J.-L., and Aubertin, M., 1990, Meta-igneous origin of Hercynian peraluminous granites in N.W. French Massif Central: implications for crustal history reconstructions: Contributions to Mineralogy and Petrology, v. 104, p. 163–172, https://doi-org.jpllnet.sfsu.edu/10.1007/BF00306440.

Valentino, D.W., Chiarenzelli, J., Piaschyk, D., Williams, L., and Peterson, R., 2008, The southern Adirondack sinistral transgressive shear system: Friends of the Grenville Field Trip 2008, Indian Lake, New York, 56 p.

Valentino, D.W., Chiarenzelli, J.R., and Regan, S.P., 2018, Spatial and temporal links between Shawinigan accretionary orogenesis and massif anorthosite intrusion, southern Grenville Province, New York, U.S.A.: Journal of Geodynamics, v. 129, p. 80–97, https://doi.org/10.1016/j.jog.2018.04.001.

Valley, P.M., Hanchar, J.M., and Whitehouse, M.J., 2011, New insights on the evolution of the Lyon Mountain Granite and associated Kiruna-type magnetite-apatite deposits, Adirondack Mountains, New York State: Geosphere, v. 7, p. 357–389, https://doi.org/10.1130/GES00624.1.

Vanderhaeghe, O., 2009, Migmatites, granites and orogeny: Flow modes of partially-molten rocks and magmas associated with melt/solid segregation in orogenic belts: Tectonophysics, v. 477, p. 119–134, https://doi.org/10.1016/j.tecto.2009.06.021.

Walsh, A.K., Kelsey, D.E., Kirkland, C.L., Hand, M., Smithies, R.H., Clark, C., and Howard, H.M., 2015, *P-T-t* evolution of a large, long-lived, ultrahigh-temperature Grenvillian belt in central Australia: Gondwana Research, v. 28, p. 531–564, https://doi.org/10.1016/j.gr.2014.05.012.

Waters, D.J., 2001, The significance of prograde and retrograde quartz-bearing intergrowth microstructures in partially melted granulite-facies rocks: Lithos, v. 56, p. 97–110, https://doi.org/10.1016/S0024-4937(00)00061-X.

Werner, C.D., 1987, Saxonian granulites—A contribution to the geochemical diagnosis of the original rocks in high-metamorphic complexes: Gerlands Beiträge zur Geophysik, v. 96, p. 271–290.

Whalen, J.B., Currie, K.L., and Chappell, B.W., 1987, A-type granites: Geochemical characteristics, discrimination and petrogenesis: Contributions to Mineralogy and Petrology, v. 95, p. 407–419, https://doi.org/10.1007/BF00402202.

White, R.W., Powell, R., Holland, T.J.B., and Worley, B.A., 2000, The effect of $TiO_2$ and $Fe_2O_3$ on metapelitic assemblages at greenschist and amphibolite facies conditions: Mineral equilibria calculations in the system $K_2O$-FeO-MgO-$Al_2O_3$-$SiO_2$-$H_2O$-$TiO_2$-$Fe_2O_3$: Journal of Metamorphic Geology, v. 18, p. 497–511, https://doi.org/10.1046/j.1525-1314.2000.00269.x.

White, R.W., Powell, R., and Clarke, G.L., 2002, The interpretation of reaction textures in Fe-rich metapelitic granulites of the Musgrave Block, central Australia: Constraints from mineral equilibria calculations in the system $K_2O$-FeO-MgO-$Al_2O_3$-$SiO_2$-$H_2O$-$TiO_2$-$Fe_2O_3$: Journal of Metamorphic Geology, v. 20, p. 41–55, https://doi.org/10.1046/j.0263-4929.2001.00349.x.

White, R.W., Powell, R., and Halpin, J.A., 2005, Spatially-focussed melt formation in aluminous metapelites from Broken Hill, Australia: Journal of Metamorphic Geology, v. 22, p. 825–845, https://doi.org/10.1111/j.1525-1314.2004.00553.x.

White, R.W., Powell, R., and Holland, T.J.B., 2007, Progress relating to calculation of partial melting equilibria for metapelites: Journal of Metamorphic Geology, v. 25, p. 511–527, https://doi.org/10.1111/j.1525-1314.2007.00711.x.

White, R.W., Powell, R., Holland, T.J.B., Johnson, T.E., and Green, E.C.R., 2014a, New mineral activity-composition relations for thermodynamic calculations in metapelitic systems: Journal of Metamorphic Geology, v. 32, p. 261–286, https://doi.org/10.1111/jmg.12071.

White, R.W., Powell, R., and Johnson, T.E., 2014b, The effect of Mn on mineral stability in metapelites revisited: New *a-x* relations for manganese-bearing minerals: Journal of Metamorphic Geology, v. 32, p. 809–828, https://doi.org/10.1111/jmg.12095.

Whitney, D.L., and Evans, B.W., 2010, Abbreviations for names of rock-forming minerals: American Mineralogist, v. 95, p. 185–187, https://doi.org/10.2138/am.2010.3371.

Whitney, D.L., Teyssier, C., and Fayon, A.K., 2004, Isothermal decompression, partial melting and exhumation of deep continental crust, *in* Grocott, J., McCaffrey, K.J.W., Taylor, G., and Tikoff, B., eds., Vertical coupling and decoupling in the lithosphere: Geological Society, London, Special Publication 227, p. 313–326, https://doi.org/10.1144/GSL.SP.2004.227.01.16.

Whitney, D.L., Hamelin, C., Teyssier, C., Raia, N.H., Korchinski, M.G., Seaton, N.C.A., Bagley, B.C., von der Handt, A., Roger, F., and Rey, P.F., 2020, Deep crustal source of gneiss dome revealed by eclogite in migmatite (Montagne Noire, French Massif Central): Journal of Metamorphic Geology, v. 38, p. 297–327, https://doi.org/10.1111/jmg.12523.

Whitney, P.R., and Olmsted, J.F., 1988, Geochemistry and origin of albite gneisses, northeastern Adirondack Mountains, New York: Contributions to Mineralogy and Petrology, v. 99, p. 476–484, https://doi.org/10.1007/BF00371938.

Williams, M.L., Grover, T., Jercinovic, M.J., Regan, S.P., Pless, C.R., and Suarez, K.A., 2019, Constraining the timing and character of crustal melting in the Adirondack Mountains using multi-scale compositional mapping and in-situ monazite geochronology: American Mineralogist, v. 104, p. 1585–1602, https://doi.org/10.2138/am-2019-6906.

Wong, M.S., Williams, M.L., McLelland, J.M., Jercinovik, M.J., and Kowalkoski, J., 2012, Late Ottawan extension in the eastern Adirondack Highlands: Evidence from structural studies and zircon and monazite geochronology: Geological Society of America Bulletin, v. 124, p. 857–869, https://doi.org/10.1130/B30481.1.